

UC San Diego

UC San Diego Electronic Theses and Dissertations

Title

Investigation of the reaction of OH and CO to form H and CO₂ by photoelectron-photofragment coincidence spectroscopy in a cryogenic ion beam trap

Permalink

<https://escholarship.org/uc/item/00d9d8k3>

Author

Johnson, Christopher Joseph

Publication Date

2011

Peer reviewed|Thesis/dissertation

UNIVERSITY OF CALIFORNIA, SAN DIEGO

Investigation of the reaction of OH and CO to form H and CO₂ by Photoelectron-
Photofragment Coincidence spectroscopy in a cryogenic ion beam trap

A dissertation submitted in partial satisfaction of the requirements
for the degree Doctor of Philosophy

in

Physics

by

Christopher Joseph Johnson

Committee in Charge:

Professor Robert Continetti, Chair
Professor Clifford Surko, Co-Chair
Professor Daniel Dubin
Professor Amitabha Sinha
Professor Congjun Wu

2011

Copyright

Christopher Joseph Johnson, 2011

All rights reserved.

The Dissertation of Christopher Joseph Johnson is approved, and it is acceptable in quality and form for publication on microfilm and electronically:

Co-Chair

Chair

University of California, San Diego

2011

To Diana, my parents, and friends, for putting up with me this long. . .

TABLE OF CONTENTS

Signature Page	iii
Dedication	iv
Table of Contents	v
List of Figures	ix
List of Tables	xii
Acknowledgements	xiii
Vita	xvi
Abstract.....	xvii
Chapter 1. Introduction	1
1.1. Chemical Reactions	1
1.2. Experimental Techniques for the Study of Reaction Intermediates	9
1.3. Photoelectron Spectroscopy	12
1.4. Photofragment Translational Spectroscopy	16
1.5. Photoelectron-Photofragment Coincidence Spectroscopy	18
1.6. Ion Storage Techniques	22
1.7. Structure of the Thesis	25
Chapter 2. Experimental Methods and Data Analysis	29
2.1. Experimental Apparatus	30
2.1.1. Ion Source	32
2.1.2. Acceleration	34
2.1.3. Time of Flight and Mass Gate	34
2.1.4. Ion Beam Trap	36
2.1.5. Detector Chamber	38
2.1.6. Vacuum System	38
2.2. Laser System	43

2.3. Detectors	45
2.3.1. Electron Detector	46
2.3.2. Multiparticle Neutral Detector	50
2.3.3. Data Acquisition System	53
2.4. Data Analysis	54
2.4.1. Discrimination	54
2.4.2. Calibration	55
2.4.3. Neutral Fragment Kinematics	57
2.4.4. Electron Kinematics	58
2.4.5. Gating	59
2.4.6. Coincidence Calculations	63
2.4.7. Photoelectron Angular Distributions	64
Chapter 3. Photoelectron-Photofragment Coincidence Spectroscopy in a Cryogenically Cooled Linear Electrostatic Ion Beam Trap	70
3.1. Introduction	70
3.2. Experimental	74
3.2.1. Trap Design	76
3.2.2. Vacuum System	78
3.2.3. Synchronization with Pulsed Laser	80
3.2.4. Intracavity Electron Detector	85
3.2.5. Experimental Details	86
3.3. Results	88
3.3.1. Trapping Lifetimes	88
3.3.2. Recoil Trajectories	90
3.3.3. Bunching Properties	92
3.3.4. Cooling	95
3.3.5. Multimass Experiments	97

3.4. Conclusions	96
Chapter 4. Dissociative Photodetachment Studies of Cooled HOCO^- Anions Revealing Dissociation Below the Barrier to $\text{H} + \text{CO}_2$	103
4.1. Introduction	103
4.2. Experimental	104
4.3. Results and Discussion	105
Chapter 5. New Insight into the Barrier Governing CO_2 Formation from $\text{OH} + \text{CO}$...	119
5.1. Introduction	119
5.2. Experimental	120
5.3. Computational	121
5.4. Results	122
5.5. Tunneling Analysis	124
5.6. Discussion	128
Chapter 6. Electron Affinities, Well Depths, and Vibrational spectroscopy of <i>cis</i> - and <i>trans</i> - HOCO	139
6.1. Introduction	139
6.2. Results	141
6.3. Discussion	143
6.4. Experimental Methods	150
6.5. Computational Methods	151
Chapter 7. Global Dissociative Photodetachment Dynamics of the HOCO Anion	155
7.1. Introduction	155
7.2. The $\text{OH} + \text{CO}$ Channel	155
7.3. <i>Cis-trans</i> Isomerization	160
7.4. The $\text{H} + \text{CO}_2$ Channel	164
7.5. Product Branching	166
7.6. The Impact of Cooled Anions	168

7.7. Conclusions	169
7.8. Future Directions	170
Chapter 8. Photoelectron Angular Distributions in Two-photon Photodetachment of NO ₂ ⁻	174
8.1. Introduction	174
8.2. Experimental	176
8.3. Results and Discussion	177
8.4. Conclusions	186
Appendix A. Design of a New Multiparticle Time- and Position-Sensitive Detector ..	190
A.1. Operating Principles	190
A.2. System Design	192
A.3. Mechanical Design	195
Appendix B. Electrical Circuits Developed in the Construction of the Instrument	199
B.1. Instrument Interlock Logic	199
B.2. Mirror Switching Circuit	201
B.3. RF Synchronization System	203
B.4. Image Charge Pickup Amplifier	205
B.5. Bunching Amplitude Modulation Circuit	210
B.6. Electron Detector Bias and Readout Circuit	212
B.7. Trap Cycle Divider	215

LIST OF FIGURES

Figure 1.1: Energetic schemes for elementary reactions	2
Figure 1.2: Examples of potential energy surfaces	7
Figure 1.3: Potential energy diagram for photodissociation	10
Figure 1.4: Photoelectron spectroscopy diagram.....	14
Figure 1.5: A schematic of direct dissociative photodetachment	17
Figure 1.6: A schematic of indirect dissociative photodetachment	19
Figure 1.7: Effect of repulsive curve shape on dissociative photodetachment.....	21
Figure 2.1: A schematic of the instrument	31
Figure 2.2: The source vacuum system	40
Figure 2.3: The UHV vacuum system	42
Figure 2.4: An ion optics simulation of the velocity map imager	47
Figure 2.5: Diagram of the wedge-and-strip anode	49
Figure 2.6: Diagram of the crossed-delay-line anode	51
Figure 2.7: Example of electron slicing	62
Figure 2.8: Example of O_2^- photodetachment anisotropy	65
Figure 3.1: Diagram of the instrument	75
Figure 3.2: Diagram of the trap assembly	77
Figure 3.3: Detail of the interaction region and electron detector	79
Figure 3.4: Timing diagram of the experiment	81
Figure 3.5: Example of unbunched and bunched photoelectron images	82
Figure 3.6: Diagram of the phase locking system	84
Figure 3.7: Decay times for various species at operational pressures	89
Figure 3.8: Fragment recoil parameters as a function of lens voltage.....	91
Figure 3.9: Bunch velocity distribution vs. RF amplitude	93
Figure 3.10: Bunch velocity distribution vs. RF phase.....	94

Figure 3.11: An example of cooling in HOCO^- anions	96
Figure 3.12: An example of multimass operation	98
Figure 4.1: Channel-resolved photoelectron spectra	104
Figure 4.2: Coincidence spectrum for $\text{HOCO}^- \rightarrow \text{OH} + \text{CO} + \text{e}^-$	106
Figure 4.3: Coincidence spectrum for $\text{HOCO}^- \rightarrow \text{H} + \text{CO}_2 + \text{e}^-$	108
Figure 4.4: Branching fractions and fitted photoelectron spectrum	112
Figure 5.1: PPC spectra for HOCO^- (DOCO^-) $\rightarrow \text{H(D)} + \text{CO}_2 + \text{e}^-$	122
Figure 5.2: Energy-resolved stable fractions	124
Figure 5.3: Model PES for <i>cis</i> - $\text{HOCO} \rightarrow \text{H(D)} + \text{CO}_2$	128
Figure 5.4: An example 2D slice of the HOCO potential energy surface	131
Figure 5.5: Prediction of tunneling lifetimes as a function of OH bond energy	133
Figure 6.1: Normal modes for <i>cis</i> - and <i>trans</i> - HOCO	140
Figure 6.2: Photoelectron spectra and anisotropy parameters for HOCO at 660 nm	144
Figure 6.3: Photoelectron spectra and anisotropy parameters for HOCO at 775 nm	146
Figure 7.1: Computed PES for HOCO and DOCO	152
Figure 7.2: Comparison of hot and cold $\text{HOCO}^- \rightarrow \text{OH} + \text{CO} + \text{e}^-$	154
Figure 7.3: Comparison of total energy release for HOCO and DOCO	155
Figure 7.4: Comparison of energy-resolved branching for HOCO and DOCO	157
Figure 7.5: Comparison of hot and cold $\text{HOCO}^- \rightarrow \text{OH} + \text{CO} + \text{e}^-$	161
Figure 8.1: Potential energy diagram for anionic and neutral NO_2	175
Figure 8.2: Sliced photoelectron images for one- and two-photon detachment	178
Figure 8.3: Photoelectron spectra and anisotropy parameters for NO_2 at 775 nm	180
Figure 8.4: NO_2^- HOMO and LCAO decomposition	183
Figure 8.5: PADs and model fits at five different electron energies	185
Figure A.1: A diagram of the detector setup	193
Figure A.2: Mechanical design of the detector	197

Figure B.1: Instrument interlock logic.....	100
Figure B.2: Mirror voltage divider schematic	202
Figure B.3: Synchronization FPGA design	204
Figure B.4: Image charge amplifier.....	207
Figure B.5: Top layer, image charge amplifier PCB	208
Figure B.6: Bottom layer, image charge amplifier PCB	209
Figure B.7: RF amplitude modulation circuit.....	211
Figure B.8: Electron detector bias circuit	214
Figure B.9: Trap cycle divider.....	216

LIST OF TABLES

Table 3.1: Selection of ion oscillation frequencies	87
Table 6.1: Overview of HOCO and DOCO vibrational frequencies	142
Table 6.2: Comparison of electron affinities and well depths for HOCO and DOCO ..	149
Table 7.1: Comparison of HOCO branching ratios	167

ACKNOWLEDGEMENTS

First and foremost I must thank my fiancée, Diana. Almost anything I now know about chemistry is directly due to her help, and nothing I don't know is her fault. My family has been curious and supportive throughout my entire career. My advisor, Bob Continetti, has been as close as I can think of to perfect of a boss for me, skillfully modulating the length of my leash to prevent me from wandering down too many alleys but allowing me to explore a wide range of possibilities in his lab. Of course, past and present members of the Continetti lab have had a profound impact on my development from someone who had barely set foot in the lab to being able to construct an entire experimental apparatus that actually works, and have all been good friends along the way. In particular I must thank John Savee and Jenny Mann for teaching me the ins and outs of the instruments and data analysis, and Qichi Hu for patiently bringing me up to speed on lasers. Additional thanks go to Jon Oakman and Zhou Lu for help in getting my head around the operation of a photoelectron-photofragment coincidence spectrometer, Anthony Fu and Andrew Moir for their assistance on the project, and Silvia de Dea for encouraging conversation and the chance to learn a little chemical engineering. Progress on performing these experiments would have been significantly slower without the help of Berwyck Poad and Ben Shen, and more recently Amelia Ray. Further helpful conversations with Mort Fineman and Joseph Taulane are greatly appreciated.

Beyond the Continetti lab, I must first thank my co-advisor Prof. Cliff Surko for helping to bridge the gap between how things are done in Physics and in Chemistry. The Physics Electronics Shop, particularly George and Allen, were crucial to the success of

the instrument, as were Don, Randall, Steve, and many other machinists in the Campus Research Machine Shop. I spent many quality hours in the office and on the couch of Andy Ault, discussing what is and isn't possible to measure for systems large and small and watching many a college basketball game. The professors in the physical chemistry division have been particularly generous in offering advice and expertise, particularly Amit Sinha, Mike Tauber, John Weare, Misha Galperin, Francesco Paesani, Kim Prather, and Judy Kim. Throughout my career Carmen Alfaro has been extremely helpful in all practical matters involving the lab, and has made my life significantly easier than it could have been.

The text of Chapters 4 and 5 are adapted from the following publications, of which the dissertation author is the primary author and the dissertation advisor is the corresponding author:

Johnson, Christopher J. and Continetti, Robert E. *J. Phys. Chem. Lett.*, **1**, 1895 (2010).

Johnson, Christopher J., Poad, Berwyck L. J., Shen, Ben B., and Continetti, Robert E. *J. Chem. Phys.*, **134**, 117106 (2011).

Additionally, the text of Chapters 3 and 6 are adapted from the following submitted articles, of which the dissertation author is the primary author and the dissertation advisor is the corresponding author:

Johnson, Christopher J., Shen, Ben B., Poad, Berwyck L. J., and Continetti, R. E. *Rev. Sci. Instrum.*, in press (2011).

Johnson, Christopher J., Harding, Michael E., Poad, Berwyck L. J., Stanton, John F., and Continetti, R. E. *JACS*, submitted (2011).

VITA

- 2005 Bachelor of Science, Butler University
- 2005-2006 Teaching Assistant, Department of Physics, University of California San Diego
- 2006 Laboratory Instructor, Department of Physics, University of California San Diego
- 2006-2011 Research Assistant, University of California San Diego
- 2008 Master of Science, University of California San Diego
- 2011 Doctor of Philosophy, University of California San Diego

PUBLICATIONS

- “Dissociative Photodetachment Studies of Cooled HOCO^- Anions Revealing Dissociation Below the Barrier to $\text{H} + \text{CO}_2$ ” Johnson, Christopher J. and Continetti, Robert E. *Journal of Physical Chemistry Letters*, **1**, 1895 (2010).
- “Communication: New Insight into the Barrier Governing CO_2 Formation from $\text{OH} + \text{CO}$ ” Johnson, Christopher J., Poad, Berwyck L. J., Shen, Ben B., and Continetti, Robert E. *Journal of Chemical Physics*, **134**, 117106 (2011).
- “Photoelectron-Photofragment Coincidence Studies of $\text{NO}^- \cdot \text{X}$ Clusters ($\text{X} = \text{H}_2\text{O}, \text{CD}_4$)” Poad, Berwyck L. J., Johnson, Christopher J., and Continetti, Robert E. *Faraday Discussions*, **150**, 481 (2011).
- “Photoelectron-Photofragment Coincidence Spectroscopy in a Cryogenically Cooled Linear Electrostatic Ion Beam Trap” Johnson, Christopher J., Shen, Ben B., Poad, Berwyck L. J., and Continetti, R. E. *Review of Scientific Instruments*, in press (2011).
- “The Electron Affinities, Well Depths, and Vibrational Spectroscopy of cis- and trans- HOCO by Photoelectron Imaging” Johnson, Christopher J., Harding, Michael E., Poad, Berwyck L. J., Stanton, John F., and Continetti, R. E. submitted (2011).
- “Spectroscopy and Dynamics of the HOCO Radical” Johnson, Christopher J. and Continetti, R. E., invited perspective in *Physical Chemistry Chemical Physics*, (2011).
- “Nonresonant Energy-resolved Two-photon Photoelectron Angular Distributions from NO_2^- Photodetachment” Johnson, Christopher J., Poad, Berwyck L. J., and Continetti, Robert E. in preparation (2011).

ABSTRACT OF THE DISSERTATION

Investigation of the reaction of OH and CO to form H and CO₂ by Photoelectron-Photofragment Coincidence spectroscopy in a cryogenic ion beam trap

by

Christopher Joseph Johnson

Doctor of Philosophy in Physics

Professor Robert Continetti, Chair

Professor Clifford Surko, Co-Chair

The HOCO radical plays a crucial role in a wide variety of chemical processes, including atmospheric CO₂ regulation and combustion chemistry, as an intermediate in the elementary reaction $\text{OH} + \text{CO} \rightarrow \text{H} + \text{CO}_2$. However, scant information exists on this species due to the difficulties in studying it. Previous photoelectron-photofragment coincidence (PPC) studies performed in this laboratory have identified key processes occurring on the HOCO potential energy surface, but are complicated by the presence of

internal excitation in the precursor anions, leading to uncertainties in product energies and dynamics.

To address this, a new instrument has been constructed which incorporates a cryogenically cooled linear electrostatic storage device, providing a cold source of anions for dissociative photodetachment studies by PPC spectroscopy. The enhanced resolution and well-characterized energetics provided by this instrument have allowed the fundamental energetics and processes occurring on the HOCO potential energy surface to be studied in unprecedented detail. New data shows unambiguous confirmation of the presence of tunneling in the reaction $\text{HOCO} \rightarrow \text{H} + \text{CO}_2$. Careful study of this product channel has led to the generation a model one-dimensional potential barrier describing this process directly from experimental tunneling data, and tunneling lifetimes over a range of relevant internal energies to be predicted. High resolution photodetachment experiments provide a reassignment of the electron affinities of both cis- and trans-HOCO and the determination of several normal mode frequencies not previously measured in the gas phase, each with the support of high-level *ab initio* quantum chemical calculations. Further details on the previously-unknown isomer well depths and the process of isomerization have been extracted using this information.

Finally, nonresonant two-photon photodetachment studies of NO_2^- , a species with striking electronic structure similarities to HOCO^- , reveal a highly asymmetric angular distribution of photoelectrons. A model for reconstructing these photoelectron angular distributions is proposed, showing that interference between atomic emissions in the

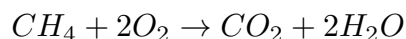
linear combination of atomic orbitals – molecular orbital picture is sufficient to explain the asymmetry.

Chapter 1. Introduction

1.1. Chemical Reactions

At the most basic level, chemical reactions are the process by which matter of some composition is transformed into matter of a different composition. For centuries the various types of chemical reactions known to occur have been classified and harnessed to create an ever-broadening array of substances. As scientific interest moved beyond the taxonomy of known reactions to analysis of these reactions, it was realized that the speed at which reactions occurred was related mathematically to the concentrations of the reactant molecules, temperature, and many other factors.^{1,2} This led to the development of chemical kinetics, which not only allowed for predictive power of reaction rates but also a hint into the microscopic processes occurring during the reaction. Complex processes could be broken down into a hierarchy of sub-reactions, culminating in a set of elementary reactions which can not be broken down further. A detailed and accurate understanding of the rates and mechanisms underlying each of these elementary reactions provides the means predict the behavior of complex reactions, even ones for which no experimental information exists, or for which experimental information is not detailed enough to directly understand the underlying mechanism.

As an example, consider the combustion of methane in oxygen,



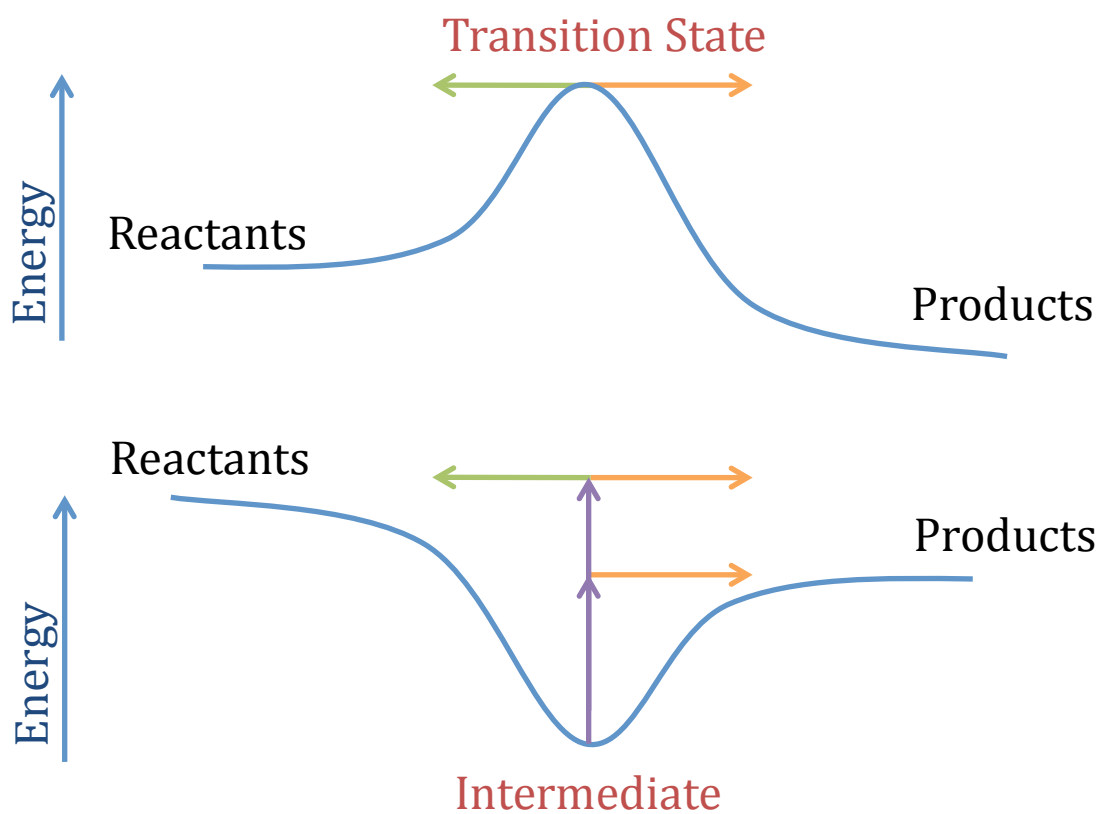
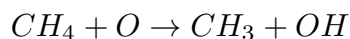


Figure 1.1: Energetic schemes for elementary reactions. Reactions with unstable transition states (a) exhibit an energy barrier to product formation. Reactions with stable intermediates (b) may freely proceed from reactants to products, or may be stabilized by collisions or radiative decay as the intermediate.

which is composed of hundreds of separated sub-reactions, themselves composed of elementary reactions such as



which cannot be simplified further. Typically elementary reactions are classified as unimolecular, consisting of transformation of a single species into one or more species, or bimolecular, in which two species interact to yield one or more new species. Additional three-body reactions occur, in which the third body acts to stabilize the products and carry away excess energy. Reactions involving a larger number of species are typically not elementary. For any elementary reaction there exists a reaction intermediate, which is the molecular configuration where the critical interactions of the reaction occur. Intermediates are generally classified in two main categories. Figure 1.1(a) depicts an unstable intermediate, also known as a transition state, which only exists for an instant as reactants transform into products. Here the x-axis is the reaction coordinate, a representation of the progress of the reaction. Reactions involving this type of intermediate are characterized by an energy barrier that must be overcome in order for the products to be created. For cases where a stable intermediate is formed, shown in Figure 1.1(b), there is an energy well in which the reactants may be trapped prior to forming the products, if energy is removed from the reactants as they near the critical configuration. The type of intermediate present in an elementary reaction strongly influences the types of experiments appropriate for its study.

These intermediates exist as points in a more general framework called the potential energy surface (PES), a representation of the change in electronic energy of the system as a function of relative atomic positions. This construct is a result of the Born-Oppenheimer approximation (BOA), in which electron motion and nuclear motion are treated as completely separable due to their large disparity in masses.³ Essentially, it states that electrons move instantaneously on the timescale of nuclear motion, and thus the electronic wavefunction is always in equilibrium for any given nuclear configuration and electronic state. In the BOA, electronic and nuclear wavefunctions are treated as completely separable,

$$|\Psi(\mathbf{r}_e, \mathbf{R}_N)\rangle = |\phi(\mathbf{r}_e, \mathbf{R}_N)\rangle |\chi(\mathbf{R}_N)\rangle \quad (1.1)$$

with the electronic wavefunction ϕ depending explicitly on electron coordinates (r_e) but only parametrically on the nuclear coordinates (R_N) and the nuclear wavefunction χ only on nuclear coordinates. The total Hamiltonian,

$$H = \sum_i -\frac{1}{2} \nabla_{r_i}^2 + \sum_i -\frac{1}{M_i/m_e} \nabla_{R_i}^2 + \sum_i \sum_{j>i} \frac{1}{r_{ij}} + \sum_i \sum_{j>i} \frac{Z_i Z_j}{R_{ij}} - \sum_i \sum_j \frac{Z_j}{|\mathbf{r}_i - \mathbf{R}_j|} \quad (1.2)$$

can then be separated into the electronic and nuclear Hamiltonians H_e and T_N , since

$$\nabla_{r_e}^2 |\chi(\mathbf{R}_N)\rangle \equiv 0 \quad (1.3)$$

and

$$\nabla_{\mathbf{R}_N}^2 |\phi(\mathbf{r}_e, \mathbf{R}_N)\rangle \approx 0, \quad (1.4)$$

where the nuclear Hamiltonian contains only the nuclear kinetic energy operator (term 2 in Equation 1.2), and the electronic Hamiltonian contains everything else. The PES can then be calculated by solving

$$E_e = \langle \phi_e(\mathbf{r}_e, \mathbf{R}_N) | H_e | \phi_e(\mathbf{r}_e, \mathbf{R}_N) \rangle \quad (1.5)$$

for all values of \mathbf{R}_N , and the total energy of the system is

$$E = E_e + T_N. \quad (1.6)$$

This approximation is generally justified when electronic motion is significantly faster than nuclear motion, i.e. for relatively heavy atoms (C, N, O and larger). However, it can induce errors in small systems such as H_2 , where nuclear motion is relatively fast, or transition metals, where electron motion can become relativistic. The BOA also breaks down when the electronic energies of two states approach degeneracy for a single geometric configuration, and non-negligible coupling terms between the two states in the electronic Hamiltonian mix the states allowing for transitions between the two.

Since the PES depicts only electronic energy as a function of nuclear configuration, nuclear motion can be solved for by using this surface as the potential function in the nuclear Schrodinger equation

$$\left[\sum_i -\frac{1}{2} \nabla_{R_i}^2 + E_e(\mathbf{R}_N) \right] |\chi(\mathbf{R}_N)\rangle = E |\chi(\mathbf{R}_N)\rangle \quad (1.7)$$

and represented by horizontal lines of constant energy (or planes, or higher dimensional surfaces) within the PES, as depicted by the example diatomic PES in Figure 1.2a. This example diatomic PES can be used to demonstrate the important points of this discussion. At infinite separation, the total energy of the system is simply the sum of the energies of each individual atom. However, as the atoms approach each other they begin to interact, and if this interaction serves to lower the energy in the system they will experience an increasingly attractive force. Eventually, at very short interatomic distances, the electrons in the atoms will begin to repel and centrifugal forces will become large, leading to a repulsive force that exactly cancels the attractive force at some distance, the equilibrium bond length for the molecule.

While quite simple in the diatomic case, the dimensionality of the PES is equal to the number of internal degrees of freedom and thus grows quickly with the number of atoms. A two-dimensional surface for a linear 3-atom system, ignoring bending motion, is shown in Figure 1.2b. For any higher dimensionality, the PES becomes extremely difficult to visualize. In these cases, reduced-dimensional PESs (such as Figure 1.2b), in which all but two or three coordinates are fixed at some value, can be of great intuitive help. Additional help comes from a potential energy diagram, which maps the energies and connectivity of “stationary” points in the molecular coordinate space,⁴ for example Figure 7.1. These stationary points, typically either bound minima, asymptotic minima, or first-order saddle points, describe certain molecular geometries at which critical interactions occur, such as equilibrium structures or the above-mentioned transition states separating these equilibrium structures.

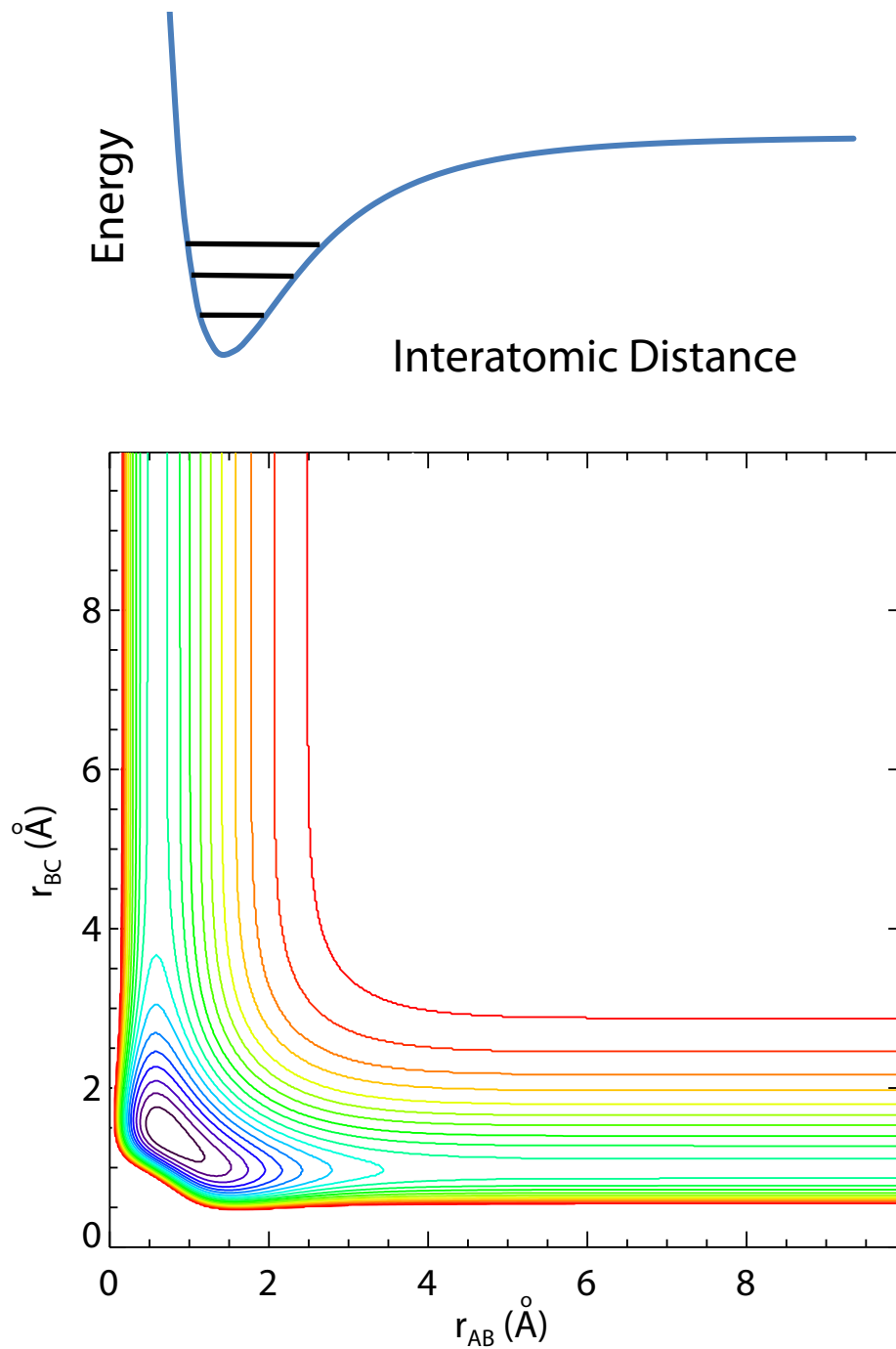


Figure 1.2: Examples of 1D (top) and 2D (bottom) potential energy surfaces for bound molecules. In the top surface, energy levels corresponding to different quanta of vibration are shown.

In principle, a complete knowledge of the PES of a system allows for all interactions and processes occurring in the system to be described and accurately calculated, at least within the limitations set by the BOA. In practice, for nearly all but the smallest systems, full quantum mechanical calculations of the dynamics on these PESs are impossible and thus many approximate methods have been developed to explore processes occurring on surfaces of a broad range of complexity.⁵ From a dynamical perspective, in addition to full quantum treatments, full- and reduced-dimensionality quantum wavepacket propagation methods have been developed to track the evolution of the system on the PES by iteratively solving the time-dependent Schrodinger equation. When these calculations prove too computationally demanding, quasiclassical trajectory calculations can be employed to essentially integrate Newton's equations in a discretized fashion for motion on the PES for a large number of different initial trajectories in the molecular coordinate space.⁶ In contrast, statistical methods can also be applied using the stationary points on the PES to determine rates of processes occurring around these points. Approaches such as transition-state theory⁷ and Rice-Ramsperger-Kassel-Marcus (RRKM) theory⁸ have shown significant predictive power for bulk thermal processes. However, a general, extensible, and universal predictive theory remains elusive, and continued development and refinement of these techniques can only occur with increasingly sophisticated and information-rich experimental studies of benchmark systems.

1.2. Experimental Techniques for the Study of Reaction Intermediates

The majority of these elementary reactions are radical reactions, meaning at least one of the reactants has an unpaired electron causing it to interact more aggressively than closed-shell molecules. The high reactivity of radicals makes them difficult to study in isolation, but convenient for studies of their interactions with other species since they can react completely on experimental time scales. Most of the information known about these reactions has been obtained by measuring their kinetics and energetics through observations in bulk. The shapes and amplitudes of the barrier or well in the reaction can be determined from kinetic data by variation of temperature and concentration of the reactants, among other things. These are commonly related by the Arrhenius equation,

$$k = A \exp \{-E_a/RT\} \quad (1.8)$$

which relates the reaction rate k to the temperature T and barrier to reaction E_a . In many cases it is necessary to add power law dependences on T , or to use stretched exponential forms of the Arrhenius equation, to describe more complex processes.¹ However, in some cases complexity of the reaction coordinate or the barrier can lead to difficulty in interpreting kinetic experiments, showing strongly non-Arrhenius behavior. In these situations, experiments on isolated intermediates themselves can offer valuable insight.

Generation and isolation of the intermediate can, however, present some difficulty. Unstable intermediates with lifetimes shorter than a few nanoseconds can be extremely difficult to observe. Even stable intermediates must be produced in enough

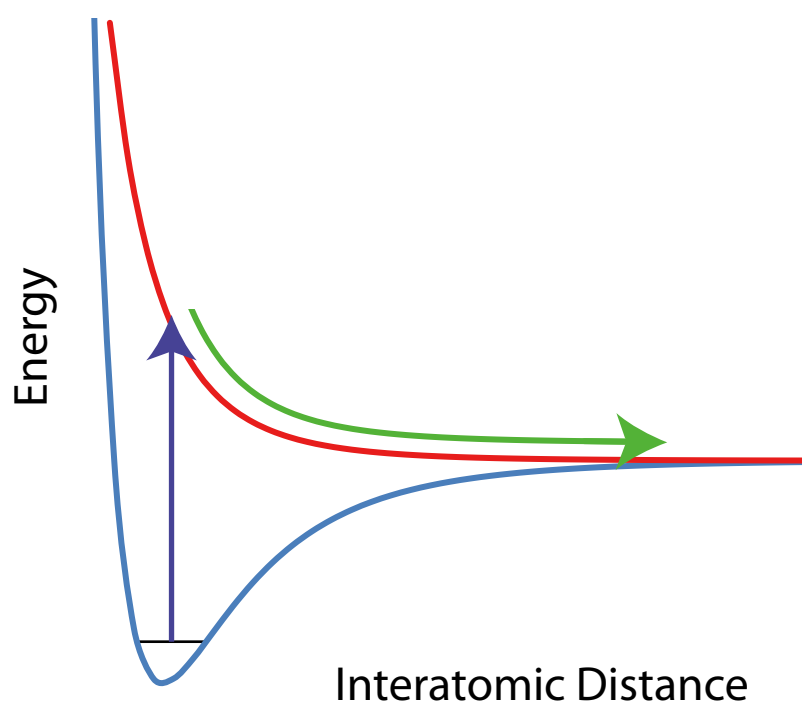


Figure 1.3: Potential energy diagram of a photodissociation/translational spectroscopy experiment. Absorption of a photon causes a transition to a repulsive excited state, and the resulting unbound molecule dissociates with a given KER.

quantity to generate a signal and must have little to no internal excitation. One effective method to accomplish this is through the use of supersonic expansions, in which gas at a high pressure is introduced through a small orifice, whose diameter is greater than the mean free path of the gas, into a vacuum chamber. As the gas expands, collisions between molecules in the expansion convert internal energy to kinetic energy and the internal temperature of the ensemble cools, often below 100 K.⁹ Since the number density in the expansion is relatively high, reactions initiated by electron-beam irradiation, electric discharges, or laser photolysis can occur. The energy resulting from the reaction is extracted by the expansion leaving internally cold products for study. Photodissociation experiments, shown diagrammatically in Figure 1.1(b) and schematically in Figure 1.3, can probe the energetics of stable intermediates by observing the onset of products or depletion of reactants as a function of absorbed photon energy, for example. However, this experiment requires efficient production of internally cold, stable intermediates, and thus is of limited use on species which are difficult to form and cool.

An alternate and complementary method for production of intermediates is the neutralization of stable precursor ions. The use of ions is convenient due to their relative ease in manipulation and identification by well-established charged-particle beam and mass spectrometric techniques. Cationic precursors can be created and neutralized through a variety of means, including dissociative recombination with low-energy electrons¹⁰ or charge exchange with a partner electron donor,¹¹ typically creating highly excited dissociative species from which valuable information about the intermediate may

be obtained. Alternately, detachment of electrons from anionic precursors can yield significant insight into the structure and dynamics of intermediates. A particularly well-developed method of this type is anion photodetachment, in which a stable or unstable neutral intermediate is produced by photodetachment by a photon of known energy of an electron from stable anionic precursor.¹² Many experimental variants employing this process exist. Threshold photodetachment, pioneered by Lineberger and co-workers,¹³ allows for electron affinities and energy resolved detachment cross-sections to be measured by tuning laser energy and monitoring electron yield as a function of wavelength. These experiments yield insights into the adiabatic and vertical detachment energies of the neutrals, and resonances in the cross-sections can be analyzed to obtain further information about the internal degrees of freedom of the system under study.¹⁴ Even more valuable information can be obtained by detachment with photons well above the adiabatic electron affinity (AEA), in an experiment known as photoelectron spectroscopy.¹⁵ This process, outlined in Figure 1.4, leads to the production of free electrons whose energy can be analyzed to reveal detailed energetic information about the neutral PES, and is the first component of the coincidence method used in this thesis.^{16,17}

1.3. Photoelectron Spectroscopy

Absorption of a photon of a given energy $E_{las} > AEA$ yields an electron with kinetic energy defined by $eKE = E_{las} - AEA - E_{int}$, where E_{int} is the internal energy of the resultant quantum state of the neutral molecule. If the photon field is sufficiently weak then this process can be well described by second-order time-dependent perturbation theory. In the dipole approximation the transition intensity can be written as

$$I \propto |\langle \psi_f | \boldsymbol{\mu}_{if} | \psi_i \rangle|^2 \quad (1.9)$$

Working within the BOA, any electronic transition such as photodetachment may be decomposed into the product of a transition dipole matrix element term accounting for the electronic component of the transition,

$$|\boldsymbol{\mu}_{if}|^2 = |\langle \phi_f | e\mathbf{r} | \phi_i \rangle|^2 = |\langle \mathbf{k} | \langle \phi_f^N | e\mathbf{r} | \phi_i^A \rangle|^2, \quad (1.10)$$

determined by the overlap of the anion (A) wavefunction with the direct product of the electron plane-wave (\mathbf{k}) and neutral (N) electronic wavefunctions, and a Franck-Condon term,¹⁸

$$FCF = |\langle \chi_f | \chi_i \rangle|^2 \quad (1.11)$$

which depends on the overlap of the initial and final nuclear wavefunctions. The FCF is a measure of the geometric similarity between the anion geometry and the neutral geometry, for detachment to the neutral absolute ground state, or neutral vibrational turning points for detachment to vibrationally excited states. A further approximation to Equation 1.9 can be made for photodetachment, in which the core electrons are not considered, giving

$$|\boldsymbol{\mu}_{if}|^2 = |\langle \mathbf{k} | \langle \phi_N | e\mathbf{r} | \phi_N \rangle | \phi_- \rangle|^2 \approx \boldsymbol{\mu}_N |\langle \mathbf{k} | e\mathbf{r} | \phi_- \rangle|^2 \quad (1.12)$$

which relates the outgoing electron wavefunction to that of only the outermost electron of the anion. This formulation can be used much more straightforwardly in calculations of

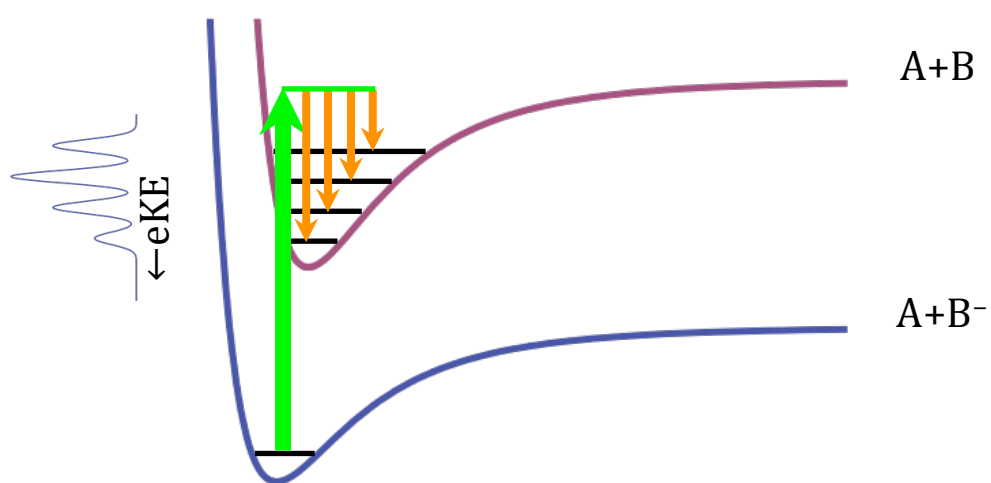


Figure 1.4: Diagram of a photoelectron spectroscopy experiment. Absorption of a photon (green) leaves the system in a given neutral state, and excess energy is carried away by the outgoing electron (orange). A corresponding photoelectron spectrum is shown.

photoelectron spectra, and more importantly, photoelectron angular distributions which will be discussed below.

As an electronic dipole transition, electron spectroscopy is still governed by the selection rule $\Delta l = \pm 1$, however the fact that the final wavefunction is represented by a direct product of the final neutral state and a free continuum electron of essentially arbitrary angular momentum allows, for example, a $\Sigma \leftarrow \Sigma$ transition from the anion to the neutral. This aspect has allowed the study of excited neutral states by photoelectron spectroscopy that are inaccessible from the ground neutral state by optical spectroscopy.¹⁹ States which are spin-forbidden from the neutral ground state can often be observed, due to the fact that the electron can carry away $\pm 1/2$ spin so that single and triplet states can be accessed from a doublet anion for instance. Additionally, since the geometries of anions typically differ from those of the corresponding neutral, some electronic states can be more easily reached in this experiment than in traditional electronic spectroscopy due to more favorable Franck-Condon factors.

Recently photoelectron spectroscopy has begun to shift to an imaging approach rather than pure electron energy spectroscopy. In the imaging technique, the distribution of outgoing electrons is projected onto a planar detector, allowing not only the electron energies ($eKE \propto r^2$) to be determined, but also the photoelectron angular distributions (PADs) with respect to the laser polarization vector. The PADs contain rich information about the molecular orbitals of the anion and neutral, and several models exist to extract this information from experimental data.^{17,20-23} Quantitative reproduction of the PADs

from first principles remains elusive, but has the potential to provide extremely useful information on the electronic structure of the species under study.

1.4. Photofragment Translational Spectroscopy

While photoelectron spectroscopy is capable of resolving neutral state energies, it is unable to explicitly provide information on the dynamics of resulting neutral dissociation such as dissociation pathways and energetics, all of which occur after the (assumed instantaneous) detachment of the electron. The most direct way to obtain this information is by detecting the neutral particle recoil velocity vectors directly.²⁴ From these velocity vectors, the masses of the fragments can be determined by enforcing conservation of momentum, and thus the recoil energy released in the dissociation process can be calculated.¹¹ If multiple fragment mass channels exist, these can be separated by momentum conservation provided the experimental resolution is sufficient. Given a known starting energy initiating the dissociation, the amount of energy partitioned into the fragments can be determined by $E_{int,prod} = KER_{max} - KER$ where KER is the total kinetic energy released in the dissociation event. If structure can be resolved and assigned in the KER spectrum, the state-resolved dynamics of dissociation can be used to investigate the flow of energy in the molecule. Like photoelectron spectroscopy, any energy that does not appear in particle kinetic energies must be held as internal energy in the fragments, providing significant insight into the photodissociation dynamics involved in the process.

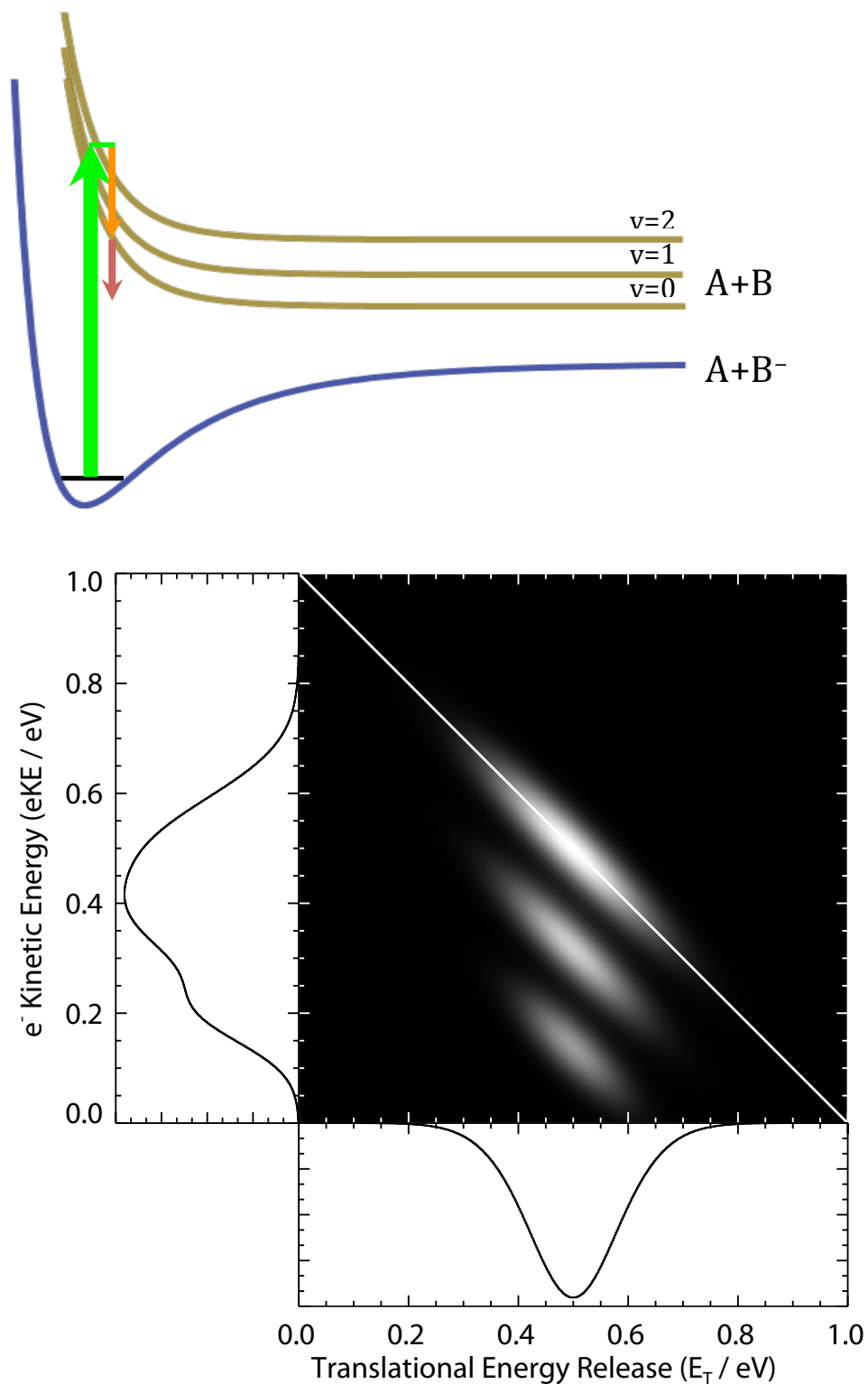


Figure 1.5: A schematic of direct DPD (top), and an example coincidence spectrum most closely matching it (bottom). The diagonal line represents the maximum total energy release possible.

While technically challenging, this experiment has been applied to a number of small molecular systems, revealing transient processes occurring on their PESs.^{25,26}

Experimentally, photofragment spectroscopy (like photodissociation) requires the capability to isolate and excite the system of interest, and detect the recoiling fragments with high efficiency and resolution. The second requirement can be met through the use of fast beams and well-developed particle imaging techniques or laser-based detection approaches, however the first requirement constrains the technique to only stable molecular systems which can be easily prepared in large quantities and concentrations.

1.5. Photoelectron-Photofragment Coincidence Spectroscopy

The experimental technique used in this thesis, photoelectron-photofragment coincidence (PPC) spectroscopy, combines the most powerful elements of both of the above techniques to yield significant insight into the dissociation dynamics of transient neutrals, which can not be isolated and separated conveniently.²⁷ In these experiments, an unstable transient neutral is prepared by first generating its stable anionic form, then photodetaching the excess electron to produce the neutral which can freely dissociate. Detection of the photoelectron kinetic energy (eKE) provides a direct measure of the initial internal energy of the neutral species, as described above. Detection of the neutral fragment recoil vectors then allows for the transient dynamics to be observed. By obtaining this information in coincidence, one ion at a time, these dynamics can be directly investigated as a function of neutral excitation, with essentially complete kinematic information on both processes. PPC spectroscopy provides a level of

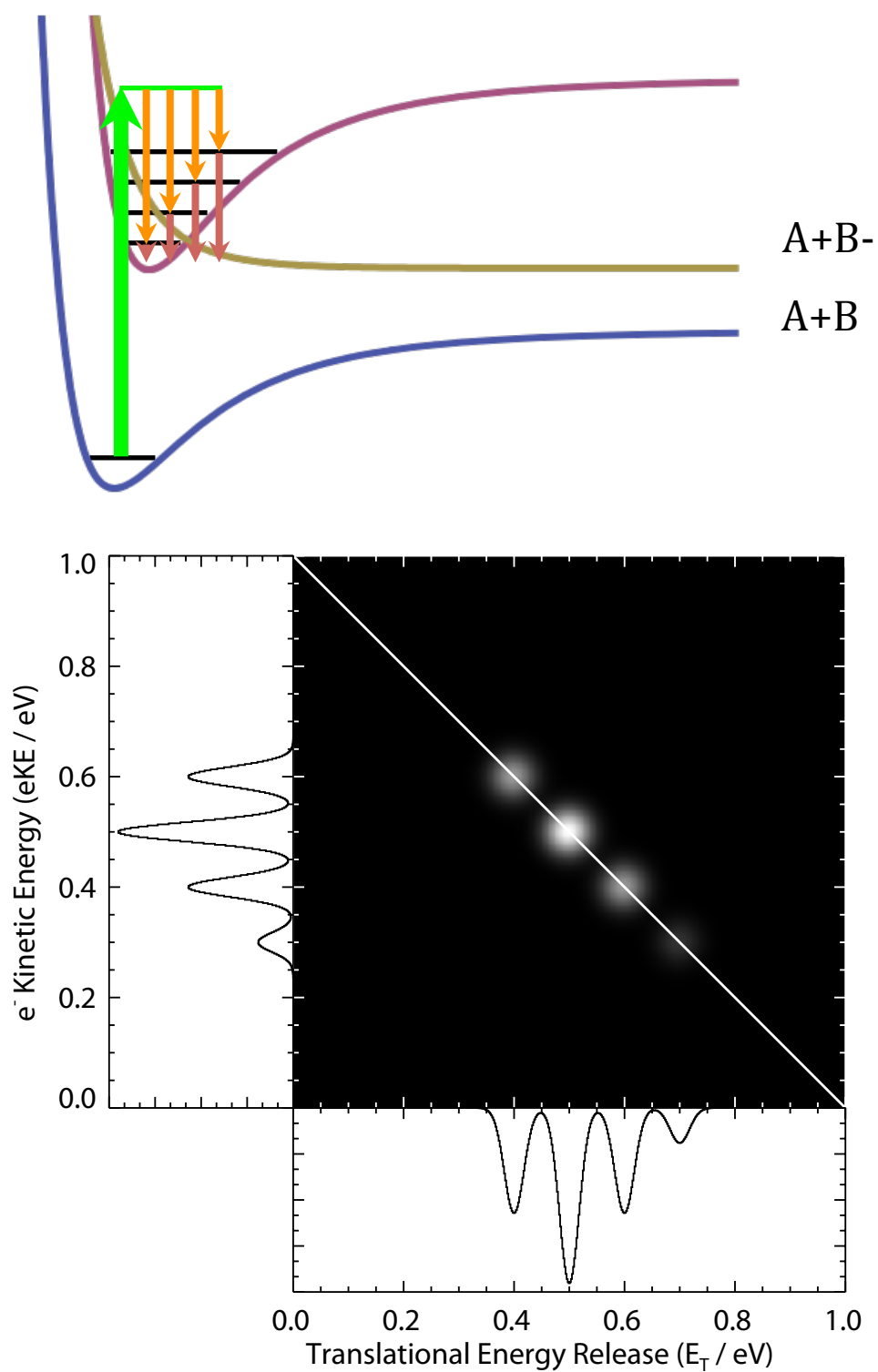


Figure 1.6: A schematic of indirect DPD, and the associated coincidence spectrum.

specificity that is unachievable in any other technique, directly revealing process that would otherwise be hidden, or would need to be inferred from less direct experiments. It also enables the dynamics of inherently unstable neutral systems to be studied straightforwardly, something not possible in most other reaction dynamics techniques.

Interpretation of PPC spectra is somewhat different than with 1D spectra; total translational energy of electrons and fragments must be conserved. For systems with bound states lying lower than product states, the maximum total energy released is given by $E_{tot} = E_{las} - AEA_n - D_{0n}$, where D_{0n} is the neutral molecule's dissociation energy, as outlined in Figure 1.5. If the neutral has no bound states, then $E_{tot} = E_{las} - D_{0a} - AEA_p$, where D_{0a} is now the anion's dissociation energy, and AEA_p is the adiabatic electron affinity of the anionic product fragment as in Figure 1.4. In either case, conservation of energy requires that any internal energy in the products leads to a commensurate reduction in total energy release. This manifests itself as a diagonal displacement away from $E_{tot,max}$ on the coincidence spectrum, typically through reduction of the observed eKE due to the stacking of dissociative curves for increasing internal excitation in products as shown in Figure 1.5. This measure of the product internal energy distribution can only be inferred or modeled in most other experiments, and the direct knowledge of it is one of the main advantages of PPC spectroscopy.

Both of the scenarios described above involve photodetachment directly to a repulsive neutral state. If, however, photodetachment occurs to a bound state which is metastable due to the crossing of a dissociative state, shown in Figure 1.7, more structure can be obtained in the coincidence spectrum. In this case, the diagonal band found in

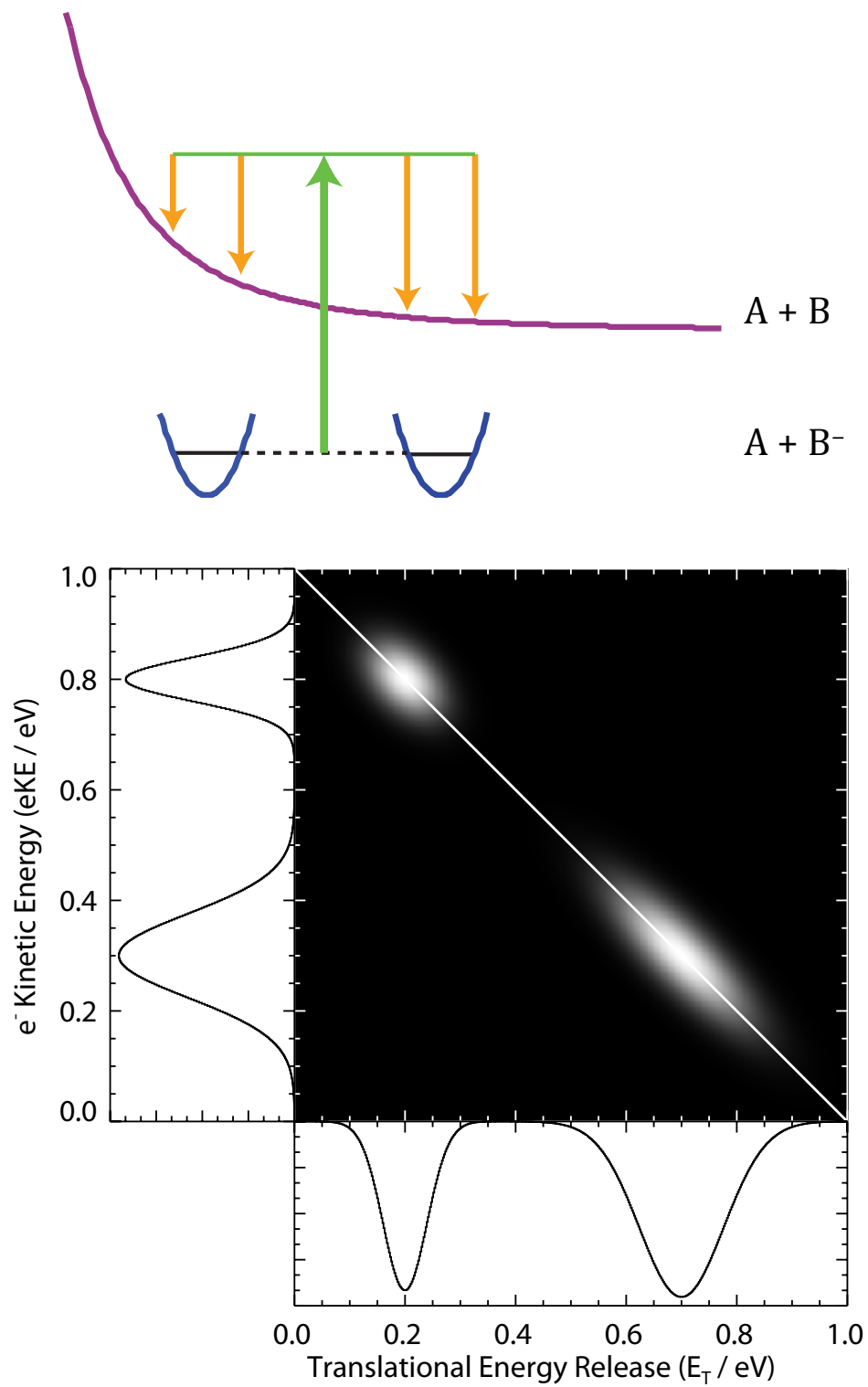


Figure 1.7: Different characteristic diagonal features for DPD to two different parts of the same repulsive curve.

direct DPD is discretized according to the internal structure of the bound state, giving a photoelectron spectrum of the bound state and a KER spectrum resulting from the hop from the bound state to the dissociative state. This process, known as indirect DPD and shown in Figure 1.6, can yield highly structured and information-rich coincidence spectra reflecting not only the internal structure of the bound state and the internal energy distribution of the products, but also the mechanisms of the coupling of the two PESs. Furthermore, the position of the spectral feature along the diagonal, and its corresponding diagonal width, provide important information on the shape of the repulsive surface in the Franck-Condon region of the anion, an example of which is presented in Figure 1.8. A broader diagonal distribution is typically indicative of a steeper slope through the Franck-Condon region, and features closer to the eKE axis clearly occur lower on the repulsive surface than features closer to the KER axis.

Though these are the most prevalent processes observed in typical experiments, unique signatures of other processes can also be found in PPC spectra. In particular, anionic photodissociation can be observed through either autodetachment or photodetachment of a product anion by a second photon. These processes, both of which have been observed in experiments on O_3^- and O_4^- , are characterized by horizontal and vertical features, respectively, in their coincidence spectra.

1.6. Ion Storage Techniques

The ability to store and manipulate charged particles has been a driving force in numerous areas of physics and chemistry over the last 100 years. From lithographically

created radiofrequency traps of millimeter dimensions²⁸ to storage rings many kilometers in diameter such as the Large Hadron Collider, these devices span an enormous range of size and storage energies. In general, ion storage devices can be divided into two categories: devices in which the time-averaged velocities of stored particles are generally zero or near-zero, which will be referred to as localizing traps for the purposes of this discussion, or devices which depend on well-defined particle velocities for storage, which will be called beam traps here.

In any device, three-dimensional confinement must occur through dynamic interactions between the charged particle and the confining electromagnetic fields. It is not possible to generate a local minimum in space using purely static electric and magnetic fields, due to the restriction that the divergence of electric and magnetic fields must be zero in free space. However, for moving charges or time-dependent fields, a stable dynamical equilibrium can be generated. For localizing traps, this equilibrium is a region of space; these traps are ideal for storing low-kinetic-energy particles. The two most common types are the Penning trap, which uses magnetic and electric fields to confine charged particles in cyclotron orbits around a cylindrical axis, and the Paul trap, which rapidly oscillates the signs of two axes of a saddle point potential, with a frequency sufficient to prevent particles from escaping.²⁹ On the other hand, beam traps can generally be considered in the family of ion storage rings, in which particles with specific velocities or energies are maintained in a stable and defined orbit by magnetic or electric fields. In other words, these traps could be thought to generate an equilibrium region in

phase space. These are most commonly realized as high-energy magnetic storage rings, though new electrostatic devices are becoming increasingly popular.

One of the original electrostatic ion traps developed was the Kingdon trap,³⁰ which consisted of a cylindrically symmetric potential created by a biased central wire, allowing particles of appropriate charge and velocity to form stable orbits. Recently, this idea has been extended to create the orbitrap,³¹ which has a shaped central electrode to generate an axially harmonic and radially logarithmic potential and is commonly used for extremely high resolution mass spectra of singly charged molecules.³² In addition, the magnetic storage ring community has recently shown increasing interest in exploiting the nearly unlimited mass range offered by electrostatic devices, and several medium-³³⁻³⁵ to large-scale^{36,37} electrostatic rings have been created or are being constructed.

It is this type of device that the electrostatic ion beam trap (EIBT) is based upon,³⁸ essentially the one-dimensional equivalent of a storage ring. In the EIBT, particles with beam-like trajectories and a given energy are reflected in stable oscillating orbits between two electrostatic mirrors. This device will be described in significantly more detail in Chapters 2 and 3, but has already been used in a number of fields as an ion source,³⁹ analyzer,⁴⁰ or a high-resolution mass spectrometer,^{41,42} and has successfully been cooled to ~ 2 K.⁴³

One of the main utilities of these storage devices is the ability to cool ions, both translationally⁴⁴ and, in the case of molecules and clusters, internally,^{45,46} over relatively long (>millisecond) time scales. In Paul and higher order RF traps, cooling of internal degrees of freedom is often accomplished with the use of a cold buffer gas,⁴⁷⁻⁴⁹ acting as

a thermal bath for the ions. In storage rings and the EIBT, with their relatively large particle velocities, internal cooling must take place radiatively or, at very high energy, by employing a diffuse beam of cold electrons (electron cooler) as the buffer gas for the ions.

It is this radiative cooling, combined with the ability to produce colder ions in a low-duty-cycle ion source, that will be harnessed to allow PPC experiments to be performed on ions with low internal excitation. Though several approaches could be envisioned to use any of these devices for PPC spectroscopy, the EIBT was chosen for its simplicity and ease of integration into the current experimental setup. The rationale for this choice will be made clear in this thesis.

1.7. Structure of the Thesis

This introduction has provided the background necessary to understand the data presented throughout the rest of this thesis. In the next two chapters the experimental apparatus and data analysis are explained, including the major advance of the inclusion of a cryogenic ion beam trap, and its performance is characterized. With this established, attention will turn to the HOCO radical and its role in the reaction $\text{OH} + \text{CO} \rightarrow \text{H} + \text{CO}_2$, the primary motivation behind this work. An interesting anisotropy discovered in two-photon photodetachment of NO_2 will then be presented, which has significant implications for earlier two-photon experiments on HOCO. Finally, a new multiparticle detector currently under development will be described, and technical documentation of important instrumental components will be given, in the appendices.

References

- (1) Steinfeld, J. I.; Francisco, J. S.; Hase, W. L. *Chemical Kinetics and Dynamics*; 2nd ed. Prentice Hall: Upper Saddle River, New Jersey, 1998.
- (2) Henriksen, N. E.; Hansen, F. Y. *Theories of Molecular Reaction Dynamics*; Oxford University Press: Oxford, UK, 2008.
- (3) Born, M.; Oppenheimer, R. *Annalen der Physik* **1927**, *84*, 30.
- (4) Xie, Z.; Bowman, J. M. *J. Chem. Theory. Comput.* **2010**, *6*, 26.
- (5) Bowman, J.; Schatz, G. *Annu. Rev. Phys. Chem.* **1995**, *46*, 169.
- (6) Schatz, G.; Elgersma, H. *Chem. Phys. Lett.* **1980**, *73*, 21.
- (7) Truhlar, D.; Garrett, B.; Klippenstein, S. *J. Phys. Chem.* **1996**, *100*, 12771.
- (8) Forst, W. *Unimolecular Reactions*; Cambridge University Press: Cambridge, UK, 2003.
- (9) Smalley, R.; Wharton, L.; Levy, D. *Accounts Chem. Res.* **1977**, *10*, 139.
- (10) Thomas, R. D. *Mass Spectrom. Rev.* **2008**, *27*, 485.
- (11) Savee, J.; Mann, J.; Laperle, C.; Continetti, R. *Int. Rev. Phys. Chem.* **2011**, *30*, 79.
- (12) Neumark, D. M. *Phys. Chem. Chem. Phys.* **2005**, *7*, 433.
- (13) Schulz, P.; Mead, R.; Jones, P.; Lineberger, W. *J. Chem. Phys.* **1982**, *77*, 1153.
- (14) Woo, S.; Helmy, E.; Mauk, P.; Paszek, A. *Phys. Rev. A* **1981**, *24*, 1380].
- (15) Brehm, B.; Gusinow, M.; Hall, J. *Phys. Rev. Lett.* **1967**, *19*, 737.
- (16) Neumark, D. M. *J. Phys. Chem. A* **2008**, *112*, 13287.
- (17) Sanov, A.; Mabbs, R. *Int. Rev. Phys. Chem.* **2008**, *27*, 53.
- (18) Condon, E. *Phys. Rev.* **1928**, *32*, 0858.
- (19) Weaver, A.; Metz, R.; Bradforth, S.; Neumark, D. *J. Chem. Phys.* **1989**, *90*, 2070.
- (20) Lin, P.; Lucchese, R. *J. Chem. Phys.* **2001**, *114*, 9350.

- (21) Oana, C. M.; Krylov, A. I. *J. Chem. Phys.* **2009**, *131*, 124114.
- (22) Cooper, J.; Zare, R. *J. Chem. Phys.* **1968**, *48*, 942.
- (23) Mabbs, R.; Grumbling, E. R.; Pichugin, K.; Sanov, A. *Chem. Soc. Rev.* **2009**, *38*, 2169.
- (24) Schinke, R. *Photodissociation Dynamics*; Dalgarno, A.; Knight, P. L.; Read, F. H.; Zare, R. N., Eds. Cambridge Monographs on Atomic, Molecular and Chemical Physics; Cambridge University Press: Cambridge, UK, 1995.
- (25) Butler, L.; Neumark, D. *J. Phys. Chem.* **1996**, *100*, 12801.
- (26) Sato, H. *Chem. Rev.* **2001**, *101*, 2687.
- (27) Continetti, R. *Int. Rev. Phys. Chem.* **1998**, *17*, 227.
- (28) Jiang, L.; Whitten, W. B.; Pau, S. *Opt. Express* **2011**, *19*, 3037.
- (29) Major, F. G.; Gheoghe, V. N.; Werth, G. *Charged Particle Traps*; Physics and Techniques of Charged Particle Field Confinement; Springer: Berlin, 2005.
- (30) Kingdon, K. *Phys. Rev.* **1923**, *21*, 408.
- (31) Hu, Q.; Noll, R.; Li, H.; Makarov, A.; Hardman, M.; Cooks, R. *J. Mass Spectrom.* **2005**, *40*, 430.
- (32) Perry, R. H.; Cooks, R. G.; Noll, R. *J. Mass Spectrom. Rev.* **2008**, *27*, 661.
- (33) Moller, S. *Nucl. Instrum. Meth. A* **1997**, *394*, 281.
- (34) Tanabe, T.; Noda, K.; Saito, M.; Lee, S.; Ito, Y.; Takagi, H. *Phys. Rev. Lett.* **2003**, *90*.
- (35) Jinno, S.; Takao, T.; Hanada, K.; Goto, M.; Okuno, K.; Tanuma, H.; Azuma, T.; Shiromaru, H. *Nucl. Instrum. Meth. A* **2007**, *572*, 568.
- (36) Zajfman, D.; Wolf, A.; Schwalm, D.; Orlov, D. A.; Grieser, M.; Hahn, R. V.; Welsch, C. P.; Lopez-Urrutia, J. R. C.; Schröter, C. D.; Urbain, X.; Ullrich, J. *J. Phys.: Conf. Ser.* **2005**, *4*, 296.
- (37) Thomas, R. D.; Schmidt, H. T.; Andler, G.; Björkhage, M.; Blom, M.; Brännholm, L.; Bäckström, E.; Danared, H.; Das, S.; Haag, N.; Halldén, P.; Hellberg, F.; Holm, A. I. S.; Johansson, H. A. B.; Källberg, A.; Källersjö, G.; Larsson, M.; Leontein, S.; Liljeby, L.; Löfgren, P.; Malm, B.; Mannervik, S.; Masuda, M.; Misra, D.; Orbán, A.; Paál, A.; Reinherd, P.; Rensfelt, K. G.; Rosén, S.; Schmidt, K.; Seitz, F.; Simonsson, A.; Weimer, J.; Zettergren, H.; Cederquist,

- H. *Rev. Sci. Instrum.* **2011**, *82*, 065112.
- (38) Dahan, M.; Fishman, R.; Heber, O.; Rappaport, M.; Altstein, N.; Zajfman, D.; van der Zande, W. *Rev. Sci. Instrum.* **1998**, *69*, 76.
- (39) Pedersen, H.; Altevogt, S.; Jordon-Thaden, B.; Heber, O.; Lammich, L.; Rappaport, M.; Schwalm, D.; Ullrich, J.; Zajfman, D.; Treusch, R.; Guerassimova, N.; Martins, M.; Wolf, A. *Phys. Rev. A* **2009**, *80*.
- (40) Aviv, O.; Toker, Y.; Errit, M.; Bhushan, K. G.; Pedersen, H. B.; Rappaport, M. L.; Heber, O.; Schwalm, D.; Zajfman, D. *Rev. Sci. Instrum.* **2008**, *79*, 083110.
- (41) Bhushan, K. G.; Gadkari, S. C.; Yakhmi, J. V.; Sahni, V. C. *Rev. Sci. Instrum.* **2007**, *78*, 083302.
- (42) Greenwood, J. B.; Kelly, O.; Calvert, C. R.; Duffy, M. J.; King, R. B.; Belshaw, L.; Graham, L.; Alexander, J. D.; Williams, I. D.; Bryan, W. A.; Turcu, I. C. E.; Cacho, C. M.; Springate, E. *Rev. Sci. Instrum.* **2011**, *82*, 043103.
- (43) Lange, M.; Froese, M.; Menk, S.; Varju, J.; Bastert, R.; Blaum, K.; Lopez-Urrutia, J. R. C.; Fellenberger, F.; Grieser, M.; Hahn, von, R.; Heber, O.; Kuehnel, K.-U.; Laux, F.; Orlov, D. A.; Rappaport, M. L.; Repnow, R.; Schroeter, C. D.; Schwalm, D.; Shornikov, A.; Sieber, T.; Toker, Y.; Ullrich, J.; Wolf, A.; Zajfman, D. *Rev. Sci. Instrum.* **2010**, *81*, 055105.
- (44) Danared, H. In *Nuclear Instruments & Methods in Physics Research Section a-Accelerators Spectrometers Detectors and Associated Equipment*; 1997; Vol. 391, pp. 24–31.
- (45) Kreckel, H.; Krohn, S.; Lammich, L.; Lange, M.; Levin, J.; Scheffel, M.; Schwalm, D.; Tennyson, J.; Vager, Z.; Wester, R.; Wolf, A.; Zajfman, D. *Phys. Rev. A* **2002**, *66*, 052509.
- (46) Toker, Y.; Aviv, O.; Errit, M.; Rappaport, M. L.; Heber, O.; Schwalm, D.; Zajfman, D. *Phys. Rev. A* **2007**, *76*, 053201.
- (47) Wang, Y. S.; Tsai, C. H.; Lee, Y. T.; Chang, H. C.; Jiang, J. C.; Asvany, O.; Schlemmer, S.; Gerlich, D. *J. Phys. Chem. A* **2003**, *107*, 4217.
- (48) Wang, X.-B.; Wang, L.-S. *Rev. Sci. Instrum.* **2008**, *79*, 073108.
- (49) Kamrath, M. Z.; Relph, R. A.; Guasco, T. L.; Leavitt, C. M.; Johnson, M. A. *Int. J. Mass Spectrom.* **2010**, *300*, 91.

Chapter 2. Experimental Methods and Data Analysis

In principle, efficient detection of recoiling electrons and neutrals in coincidence from DPD processes requires detectors capable of collecting products ejected over the full 4π steradian distribution surrounding the interaction point. This requirement can be avoided by projection of the centers of the outgoing electron and neutral distributions onto a finite planar time- and position sensitive detector. For neutral particles which are not easily manipulated, this is accomplished by the use of a fast precursor ion beam, allowing neutral particles to be detected at high lab energies with relatively small detectors while still enabling straightforward reconstruction of the center-of-mass frame kinematics. Electrons can simply be extracted out of the ion beam and detected in a similar manner. The utility of the ion beam is threefold: 1) by accelerating ions to a known lab frame kinetic energy, ions of differing masses can be separated and isolated by time-of-flight, 2) the center-of-mass frame trajectory is well known, and 3) detection efficiencies for individual particles at keV energies are significantly higher than for low-energy particles. Thus these experiments are performed in what is essentially a low-energy particle accelerator for molecular ions. This instrument, shown diagrammatically in Figure 2.1, consists of an ion source, accelerating and guiding ion optics, a laser interaction point, and a multiparticle neutral and single-particle electron detector, all of which will be discussed in the ensuing sections.

2.1. Experimental Apparatus

The major advance described here and used for the experiments in this thesis is the ability to store and cool ions in a trap while still maintaining the above merits of the ion beam approach. To that end, prior to embarking on a detailed description of the components comprising the instrument, a brief description of the experimental procedure will be given. The trap, known as the electrostatic ion beam trap (EIBT) and first introduced in the group of Daniel Zajfman at the Weizmann Institute, consists of a linear reflecting ion resonator which is capable of storing a beam of ions oscillating between two electrostatic focusing mirrors, similar to an optical resonator.¹ The choice of this type of device over traditional Paul or Penning traps is governed by two main considerations. First, the EIBT maintains ions in a nearly monoenergetic beam with a well-defined ensemble of trajectories, allowing the previous single-shot ion beam experiment to be directly adapted to use in the trap. Second, it contains a large field-free region between the two mirrors, allowing detectors to be placed in the trap cavity without destructively perturbing ion oscillation. Furthermore, the lack of oscillating electric fields and any magnetic fields yields photoelectron trajectories that can be easily manipulated and reconstructed in data analysis. These devices are finding increasing use in nuclear, atomic, and molecular physics,² as well as mass spectrometry.³⁻⁵

In this implementation, the EIBT and its surroundings are cooled to cryogenic temperatures and PPC experiments are performed in the cavity itself. Photodetached electrons are extracted out of the ion-laser plane to an intracavity electron detector.

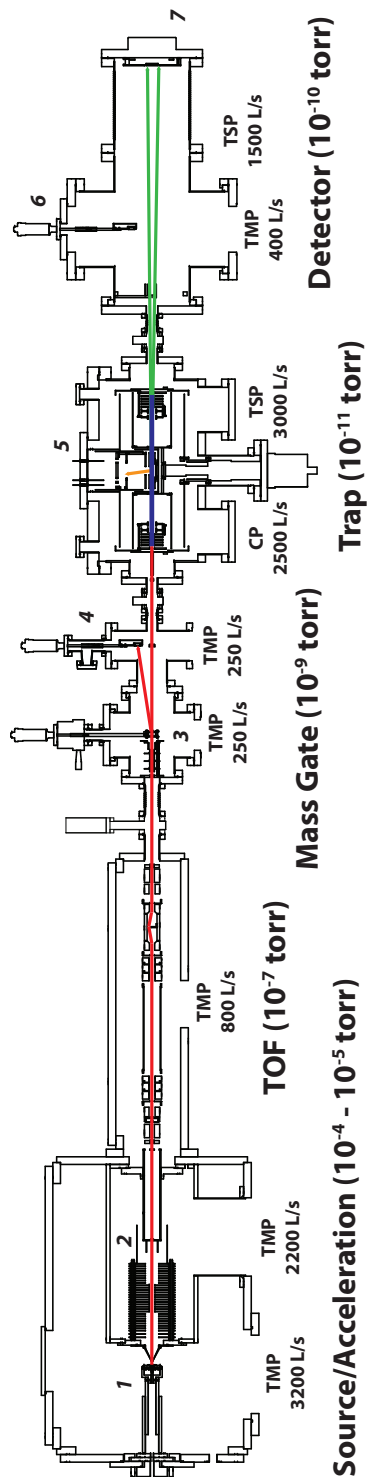


Figure 2.1: An overview of the instrument, including pumping and typical operational pressures.

Neutral products resulting from photodetachment of an electron from a trapped anion continue along the beam center-of-mass trajectory and impact a second detector, maintaining the detection scheme required for the photoelectron-photofragment coincidence experiments described in this thesis. In the ensuing sections, each set of components of the instrument will be described in detail, the experimental process and data analysis explained. In Chapter 3, the trap itself will be described in detail, and measures of its performance that are relevant to these experiments will be presented. The fundamental characteristics of the EIBT have been explored at the Weizmann Institute,⁶⁻⁹ and will not be presented here.

2.1.1. Ion Source

The heart of the instrument is the ion source – the rest of the instrument is just biased metal if there are no ions on which to perform the experiment. The role of the ion source is to generate a molecular plasma containing a mixture of ionic species, one of which is the target for study, in sufficient numbers to allow the experiment to be performed. Ion source chemistry, while still poorly understood, is a feature of nearly all molecular ion beam techniques, and thus many approaches for the generation of molecular ions exist. The ion beam source used in this experiment is a pre-existing PPC spectrometer, and as such the Source, Accelerator, and TOF segments described below are essentially identical to those already reported.¹⁰

Of the available ionization techniques, the method of choice in this experiment is ionization in a pulsed supersonic expansion. A supersonic expansion occurs when gas

passes from a high-pressure (3-5 atm) volume to a low-pressure (<1 mtorr) volume through an orifice much larger than the mean free path of molecules in the orifice.¹¹ At the end of the expansion, molecules attain a velocity significantly higher than the speed of sound at the orifice, giving rise to the term supersonic. An important property of this type of expansion is the significant cooling of internal degrees of freedom due to inelastic collisional transfer of internal energy to kinetic energy during the expansion. This cooling, while non-thermal and generally system-specific, is found to produce ensembles of molecules with vibrational temperatures typically <100 K and rotational temperatures <20 K.¹² Ionization in the supersonic expansion is attractive not only due to the high directionality and density of the resulting molecular beam, but also this cooling effect. Molecular anion generation, typically occurring through collisions with energetic molecules or attachment of free low-energy electrons, inherently induces internal excitation in the resulting ion. By ionizing early in the expansion, this internal excitation can often be efficiently removed. However, for ions requiring creation late in the expansion, cooling is less efficient and can lead to significant internal excitation.^{13,14}

The current implementation is based upon a pulsed supersonic expansion at 10 Hz. The target gas mixture, typically at a stagnation pressure of 4-5 atm, expands through a 250 μm cylindrical nozzle actuated by a fast piezoelectric disc. Immediately after the inlet, a coaxial pulsed electric discharge (typically 300-500 V, 50 μs square pulse) is activated, fragmenting and ionizing molecules in the gas mixture and initiating neutral and ion chemistry. As this mixture continues to expand, it is intersected by a 1 keV beam of electrons from a filament-based electron gun. High-energy electron-

molecule collisions cause further fragmentation and generating low-energy secondary electrons that have a high probability of attaching to the species in the expansion to create anions. The “ion soup” created in this process is sampled by a conical skimmer with a 3 mm diameter opening in the tip, ensuring that only ions on the expansion centerline, the coldest and densest portion, continue to form the fast ion beam.

2.1.2. Acceleration

The portion of the beam passing through the skimmer is immediately accelerated by a stack of plates with annular holes, progressively biased at increasingly higher voltages by a resistor-chain voltage divider. Several of these plates are reserved to allow independent control of their voltage, allowing them to be used in an einzel lens configuration to help collimate ions as they are accelerated. Once at full beam energy, the ion beam passes into a metal cylinder that is capped at both ends with 3 mm holes along the centerline. While ions are inside of this cylinder, its potential is rapidly (~30 ns) switched to ground using a fast high-voltage switch,¹⁵ rereferencing the ions to ground and alleviating the need to float any part of the instrument at the beam voltage. This process results in a collimated, nearly monoenergetic beam of ions which can be conveniently guided through the rest of the instrument.

2.1.3. Time of Flight and Mass Gate

Since each species of differing mass/charge ratio (m/q) in a monoenergetic beam has a different lab velocity, ions can be separated and identified by their times-of-flight (TOFs) over a given distance. This allows for identification and isolation of the species

of interest from the rest of the ions created in the source. In principle, however, the spatial and temporal length of a packet of ions is governed by the length of the potential switch, and thus unit-mass separation is not typically achievable over the current TOF distance. In order to circumvent this issue, a narrow length of ions can be “chopped” from the packet to drastically increase the resolving power of the TOF mass spectrometer. The implementation used in the current instrument is the “Bakker-style” chopper,¹⁶ in which the ion beam passes between two parallel plates, one rapidly switched (~ 100 ns fall time) from a given voltage V to ground and another held at a static voltage $V/2$. Ions early in the packet are deflected towards one plate, ions late in the packet are deflected towards the other, and only ions between the two plates during the switch feel no overall tangential acceleration. Selection of only those ions continuing along the original beam trajectory yields ion packets of <100 ns FWHM, significantly shorter than a 1 amu difference in TOF over the mass range of interest, yielding a mass spectrum with resolution appropriate for the identification of ion masses in the 1-200 amu range.

As the ion beam undergoes this mass selection process, it is focused and guided using a set of ion optics. Ion deflection is achieved using two sets of horizontal and vertical deflectors in the near-field and far-field regions of the TOF chamber. These deflectors consist of parallel pairs of metal plates on opposing sides of the ion beam, which carry user-adjustable DC bias voltages to attract or repel ions as they pass. The ion optics stack also contains two electrostatic einzel lenses to telescope and collimate the ion beam. These lenses consist of three coaxial cylindrical electrodes, the outer two held

at ground and the inner biased to some DC voltage. This arrangement creates a radially inhomogeneous field which causes ions at larger radii to be radially deflected towards or away from the beam centerline, the direct analog of an optical lens. Finally, to reduce the considerable flux of fast neutrals created by collisional electron detachment with background gas, a beam block is placed on the beam centerline in an electrode configuration allowing ions to be deflected over the block and returned to their original trajectories.

In a single-shot experiment, this separation is sufficient to allow only the mass of interest to be intersected by an appropriately timed laser pulse. However, in the trapping experiment many masses can be simultaneously stored. In most situations, this situation is not optimal, and thus a “mass gate” is implemented to allow only the mass (or a small range of masses) of interest to pass to the trap. This mass gate consists of two parallel plates at equal but opposite voltages which are rapidly switched to ground to allow the mass of interest to pass, then rapidly returned to their respective voltages, with rise and fall times <20 ns. Ions outside of this pulse are deflected out of the beamline to a timing detector for observation of their TOFs.

2.1.4. Ion Beam Trap

The ion beam trap component to this experiment is described in detail in Chapter 3 of this thesis, and thus will only be outlined here for the sake of continuity. As stated in the beginning of this chapter, the EIBT is the ion optical analogue to an optical resonator, which allows it to store beams of ions at keV energies in stable reflecting orbits between

two focusing electrostatic mirrors. The ability to store beams with well-defined trajectories, rather than clouds of ions with nearly thermalized motions, makes this device ideal for the fast ion beam experiments in this thesis. Ions are injected into the EIBT through one mirror held at ground; if the mirror is switched to trapping voltage before the first round trip of the ions, they will remain trapped in the cavity, with the primary loss mechanism being charge exchange with the background gas.

In this implementation, the entire trap apparatus is cooled to cryogenic temperatures, and surrounded with cryogenic heat shields, to allow stored ions to radiatively cool over periods of several seconds. Since extracting the ions after this cooling period would have disastrous consequences on the duty cycle of the experiment, the electron detector assembly is placed at the center of the trap and ion-laser interactions are carried out repetitiously on the same bunch of ions at the normal 1 kHz laser repetition rate. Photodetached neutrals recoil out of the end of the trap towards a neutral particle detector, and electrons are extracted out of the trap into an electron detector. By performing the experiment this way, the standard PPC experimental technique is minimally perturbed, significantly simplifying the implementation of this complex experimental apparatus.

Since the natural kinetic energy spread and Coulomb interactions of the ions cause the injected ion packet to disperse over time, ultimately filling the entire cavity length, an active system must be employed to maintain a high target density at the laser crossing, and to ensure that ions are travelling towards the neutral particle detector for coincidence detection. The system implemented for this consists of a cylindrical

electrode along the beamline with a small sinusoidal RF voltage applied to it, causing the ion packet to bunch and phaselock to the RF if the natural oscillation frequency is close to the bunching frequency. This RF voltage is driven by and phaselocked to the master oscillator of the laser, ensuring automatic phaselocking of the ion packet to the laser pulses. This system is described in detail in Chapter 3 and Appendix B.

2.1.5. Detector Chamber

The detector chamber serves two purposes, to house the multiparticle neutral detector and a timing detector for measuring time-of-flight spectra of ions during the beam optimization phase of the experiment. The neutral particle detector, described in Section 2.3.2, is positioned along the trap axis on a vertically translatable mount to allow fine-tuning of the center of the distribution of particle impacts on the detector face. A parallel plate electrostatic deflector is placed in the beamline to deflect ions into a simple TOF ion detector, a simple stack of two 1" diameter microchannel plates (MCPs), whose emitted charge is collected by a stainless steel anode and amplified by a high-speed preamplifier. This system provides signals with rise and fall times of ~ 10 ns, more than fast enough for effective TOF mass determination.

2.1.6. Vacuum System

An inherent requirement for the successful execution of these experiments is a differentially-pumped high performance vacuum system providing the >14 orders of magnitude pressure drop from the inlet nozzle in the ion source to the laser-ion interaction region. The primary purpose of this pressure drop is a reduction in the

number of collision between ions in the beam and background gas. The occurrence of these collisions, which can lead to heating of ions or loss of beam intensity, is a function of the path length, itself a function of the number density of the background gas. Given that the instrument is several meters long, a background pressure corresponding to a mean free path of tens of meters or more fulfills this condition for efficient transport of ions to the trap. However, a single round trip of an ion bunch in the trap covers a distance of approximately one meter, so with oscillation rates on the order of hundreds of kHz, mean free paths of greater than 10^6 meters are required for several seconds of storage. Meeting these constraints requires careful vacuum system design and operation, as will be discussed in this section.

The instrument vacuum system can be roughly divided into two almost independent subsystems, a high vacuum system, with base pressures of $\sim 10^{-8}$ torr, and an ultrahigh vacuum system, with base pressures below or well below 10^{-9} torr. These two subsystems operate independently of one-another, partly due to the increased requirements for cleanliness below 10^{-8} torr, and also the higher frequency of maintenance performed in the high vacuum region. The source, acceleration, and time-of-flight optics are each housed in separate differentially pumped chambers, each separated by small orifices to allow the ion beam to pass freely from chamber to chamber while reducing the transfer of background gas to downstream chambers. These three chambers make up the high vacuum system and are isolated from the ultrahigh vacuum system by a beamline gate valve, allowing these regions to be vented and pumped down without disrupting the operation of the ultrahigh vacuum chambers. The individual

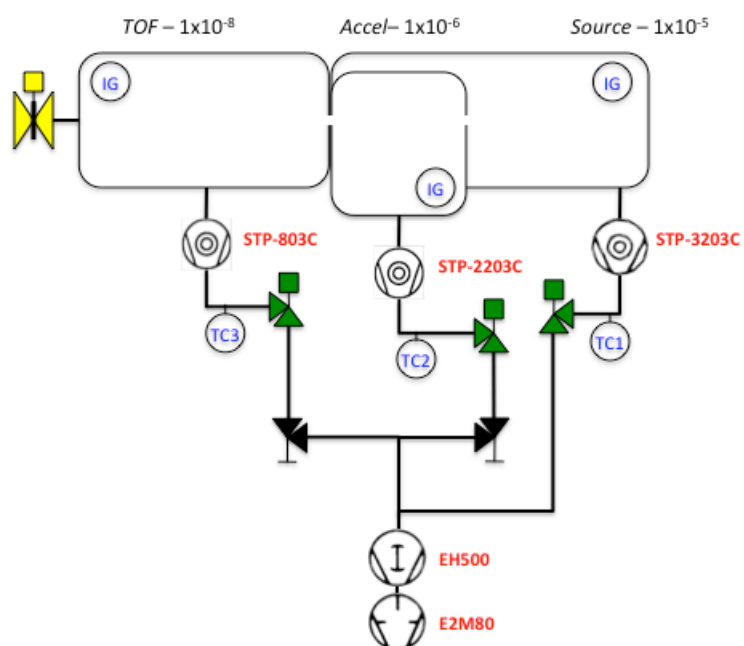


Figure 2.2: The source vacuum system. All three chambers are connected by 3 mm orifices. The gate valve isolates this system from the mass gate chamber.

chambers are each evacuated by magnetically-levitated turbomolecular pumps (TMPs), with pumping speeds of 3200 L/s on the source chamber, 2200 L/s on the acceleration chamber, and 800 L/s on the time-of-flight chamber. Since TMPs are unable to exhaust to atmospheric pressures, all three pumps exhaust to a common foreline which is evacuated by a large rotary vane pump whose pumping speed is boosted by a roots blower.

The ultrahigh vacuum system also consists of three vacuum chambers, though the requirements for each chamber in this system are more unique than for the source system. Each chamber is isolated by gate valves along the beamline, allowing one to be vented and pumped down while the other two are under vacuum. This capability requires a more complex foreline system, which will be described in detail. A variety of ultrahigh vacuum pumps are used in these chambers. The most upstream chamber, housing the mass gate, is pumped by two TMPs of ~250 L/s each, ensuring that essentially no gas load from the source chambers impacts the critical vacuum of the trap chamber. The trap chamber, a large 24" ID cylindrical chamber, is pumped by a 2500 L/s cryopump and a home-built, 3000 L/s titanium sublimation pump (TSP). The detector chamber is pumped by a magnetically levitated 400 L/s TMP which exhausts directly into another 250 L/s TMP to increase the overall compression ratio of the system and reduce the partial pressures of hydrogen and helium, for which TMPs have poor compression.

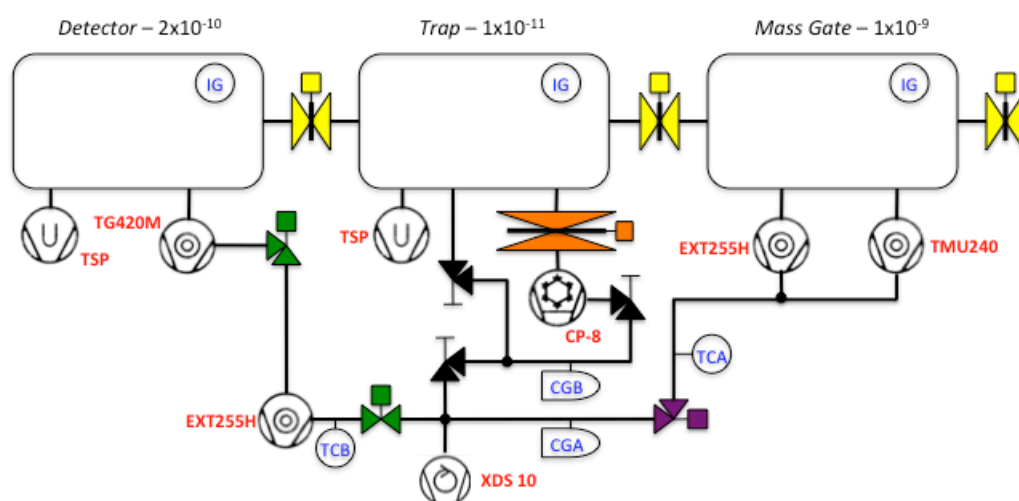


Figure 2.3: The UHV vacuum system. Gate valves separate all chambers.

Only the TMPs require backing by a mechanical pump, and the total throughput of the system is small due to the low gas load from the source, so the entire UHV section can be backed by an 8 cfm small scroll pump. The use of a single backing pump increases the complexity of pumping down one chamber while the others are under vacuum, as during pumpout the roughing pressures are too high for operation of TMPs at full speed. Additionally, the roughing valves for the trap chamber and cryopump are Viton-sealed, and thus permeation through the Viton o-rings can be a significant load on a vacuum chamber at 10^{-11} torr. This fact necessitates that the volume behind the roughing valves must also be at rough vacuum to eliminate permeation, and must not be allowed to rise to atmosphere during pumpout of the other chambers. To address this, each chambers' forlines are isolatable by valves which can be closed as needed during pumpdown. Foreline valves behind TMPs under no load can be closed for several minutes without concern, as pressure rises in the forelines typically remain lower than the critical backing pressures for TMP operation.

2.2. Laser System

The high temporal resolution required for accurate electron TOF detection (discussed in Section 2.3.1) mandates the use of short-pulse picosecond lasers in these experiments. Similarly, the high duty cycle required for the inherently low-signal coincidence technique requires high laser repetition rates. These specifications are both met by cavity-dumped, modelocked lasers, and the system used in the studies presented in this thesis will be described here.

The laser used for all studies in this thesis is a Ti:Sapphire-based regenerative amplifier, producing 1.8 picosecond, 400 μJ pulses at a repetition rate of 1.038 kHz at 775 nm. As with most lasers with similar pulse lengths and energies, the peak powers of pulses are too high for optical components in the laser cavity, thus a scheme known as chirped pulse amplification (CPA) is employed. In CPA systems, a short pulse is stretched temporally using dispersive elements, mapping longer wavelengths to later times in the pulse. Using this method, the short pulse can be stretched to tens of picoseconds, safe for amplification in the cavity. Since the chirp is well defined, the pulse can then be compressed post-amplification using a similar dispersive system, recovering the short pulse length.

The regenerative amplifier used in these experiments is composed of a series of lasers and optical systems. Low energy picosecond pulses are produced in a modelocked, diode pumped fiber laser at 43.58 MHz. These seed pulses, of nJ energies, are stretched using a grating based system and injected at 1.038 kHz (division factor of 42,000) into a Ti:Sapphire amplifier cavity which is pumped by a high-power q-switched Nd:YAG laser. The stretched seed pulse makes several passes through the excited Ti:Sapphire crystal until it reach its maximum energy, at which time it is ejected using a fast polarization rotator (Pockels cell) into a grating/prism compressor, giving the final output pulse.

These output pulses can be further manipulated by a variety of nonlinear techniques, providing a large range of photon energies for use in experiments. The 775 nm (1.60 eV) fundamental beam can be doubled (388 nm, 3.20 eV) or tripled (258 nm,

4.80 eV) using nonlinear crystals, with a commensurate reduction in pulse energy. For more fine-grained wavelength selection, the 388 nm pulses can be used to drive a travelling-wave optical parametric amplifier of superfluorescence (TOPAS), which produces tunable output over the range 460 nm – 720 nm and 830 nm – 2 μ m albeit at significantly lower pulse energies. The TOPAS works by generating a very broadband, coherent superfluorescent beam from which the target wavelength can be selected and amplified in a multi-stage optical parametric amplifier. The TOPAS output can undergo further nonlinear interactions to extend the tuning range, yielding low pulse energies which significantly reduce the rate of data acquisition but extend the wavelength range as low as 230 nm.

Regardless of the wavelength chosen, the final beam is steered towards the instrument and passed through a series of irises to ensure proper alignment. The beam is focused into the ion beam using a 500 mm focal length lens, yielding a typical spot size in the interaction region of < 1 mm. Residual beam exits the instrument and is used to trigger the timing systems of the detectors, described in the next section.

2.3. Detectors

As opposed to high-energy physics experiments, in which particles can be tracked by their deposition of energy in multiple detector channels, at keV energy ranges particles typically can undergo only one interaction with the detection system. Thus, for a single detector, full reconstruction of particle trajectories can only be accomplished if the trajectory can be completely characterized by just one impact. This requires a system

that is able to map particle $[v_x, v_y, v_z]$ vectors into some type of spatiotemporal coordinate system under some known transformation. The simplest solution is to project the center-of-mass recoil dynamics, occurring at eV kinetic energies, onto a detector with the center-of-mass frame moving at keV energies in the lab frame. This scheme effectively allows the full 4π distribution of products to be mapped to two spatial dimensions plus time, a coordinate system that allows straightforward conversion to particle velocities as is required.

This is the scheme chosen for electron and neutral particle detection. In principle, both detectors work very similarly. Single energetic particles impact an electron multiplier composed of a set of microchannel plates with an overall gain of more than 10^7 , generating a cloud of electrons that impinge on an anode capable of encoding both position and time of arrival of the electron cloud. The encoded positions and times of multiple neutral fragments and electrons are recorded on an event-by-event basis, allowing a full kinematic reconstruction of the event after the fact in data analysis. Despite this similarity, the encoding methods of the detectors differ significantly.

2.3.1. Electron Detector

Photoelectron imaging has made significant advances in resolution with the advent of Velocity Map Imaging (VMI).¹⁷ This system consists of focusing electrodes designed to counteract blurring effects due to the finite laser-ion interaction volume by mapping charged particle velocities to specific points on a planar detector, as shown in Figure 2.4. VMI has been used with great success in electron and ion detection, with

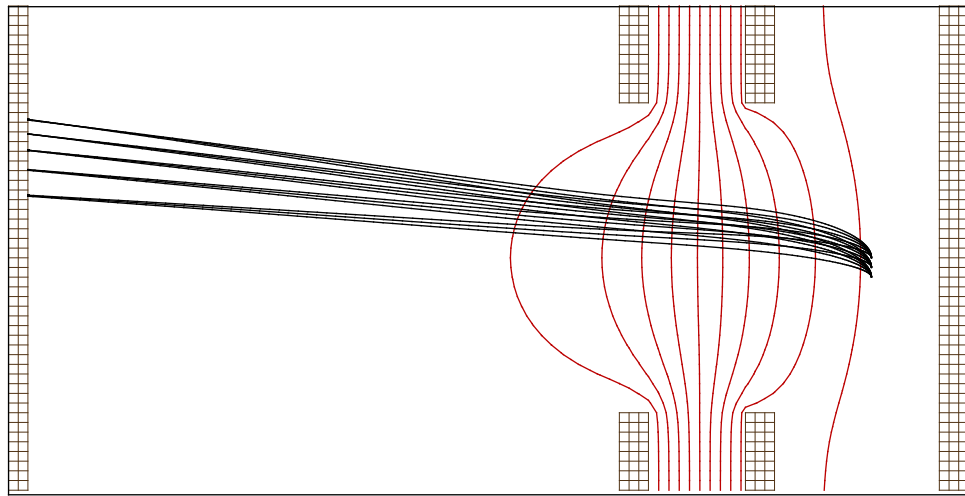


Figure 2.4: An ion optics simulation of the VMI electron detector, cylindrically symmetric about the horizontal centerline. Electrons are released from three different points (0, 1, and 2 mm from the cylindrical axis) at five energies (0.5, 1, 1.5, 2, and 2.5 eV). Electrons of a given energy but different origins are mapped to the same point on the detector face (far left).

resolutions often approaching $1\% \delta r^2/r^2$.¹⁸ A disadvantage of the VMI approach in the 3D imaging experiments done in this lab is that, along with focusing radially, the distribution of electron TOFs is compressed, with simulations showing differences in TOF of only 2 ns between 1 eV electrons ejected towards and away from the detector. With timing resolution of ~ 200 ps, this clearly becomes the resolution-limiting factor. Using ion-optics simulation software (Simion 8.0), a VMI design was optimized to produce the best balance of spatial resolution and timing dynamic range. This detector routinely delivers good performance for overall velocity resolution, which can be improved to $\sim 2\text{-}5\%$ by using the slicing method in data analysis, outlined in Section 2.4.5. The main limitations to this resolution are the effects of the movement of the electron-neutral center of mass over the TOF of an electron to the detector, and distortions of the image due to inhomogeneity in the detected positions.

Since at most one electron is expected per laser pulse, the electron detector requirements are relatively simple. The encoding method used in this detector is known as “wedge-and-strip,” shown in Figure 2.5, in which charge division between specifically shaped electrodes provides position information.^{19,20} This detector is divided into three electrodes: the wedge electrode, which consists of a comb of tapered fingers, the strip electrode, another comb of parallel fingers with increasing thicknesses which is interdigitated with the wedge electrode, and the zig-zag electrode, which fills the space between the wedge and strip. Assuming that the electron cloud incident on the wedge-and-strip anode is larger than one period of the pattern, the ratio of charge on the wedge

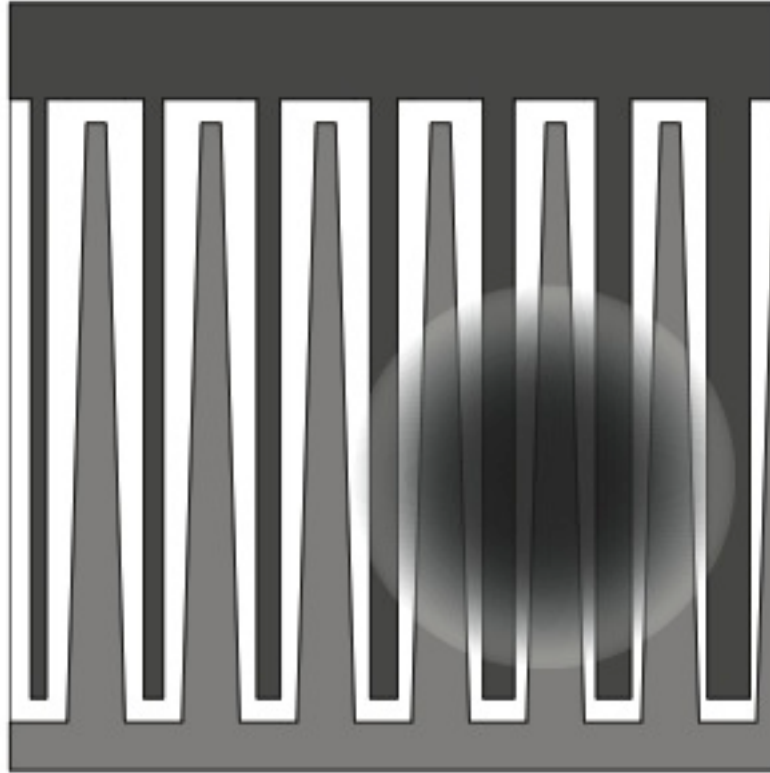


Figure 2.5: Wedge (light gray), strip (dark grey) and zig-zag anodes (not to scale). An example charge distribution is shown covering multiple periods.

to total charge encodes position along the finger direction, while the ratio of strip to total charge encodes position perpendicular to the fingers. The zig-zag electrode serves merely to capture the charge missing the wedge and strip electrodes, allowing proper normalization for the total charge incident on the anode.

The charges on each electrode are amplified and digitized in three channels of a charge-sensing analog-to-digital convertor (ADC). Timing information can be collected by capacitively coupling a high-speed preamplifier to one of these electrodes. The electron TOF is determined by the difference in time of the laser pulse, detected after passing through the interaction point, and the arrival time of the electron. Both laser and electron timing signals are first fed into a constant fraction discriminator (CFD), which triggers at 20% of the peak height of each signal rather than a set threshold, giving accurate timing information for signals of significantly varying intensity typical for these detectors. These triggers are routed to a time-to-amplitude convertor (TAC), which outputs a voltage proportional to the difference in time between a start and stop signal, in this case the laser and electron CFD outputs respectively. This voltage is then digitized in the fourth channel of the ADC.

2.3.2. Multiparticle Neutral Detector

The requirement of detecting several particles with time and position information precludes the use of the wedge-and-strip anode described above, as two impacts effectively scramble the charge division technique. The anode can be split into two

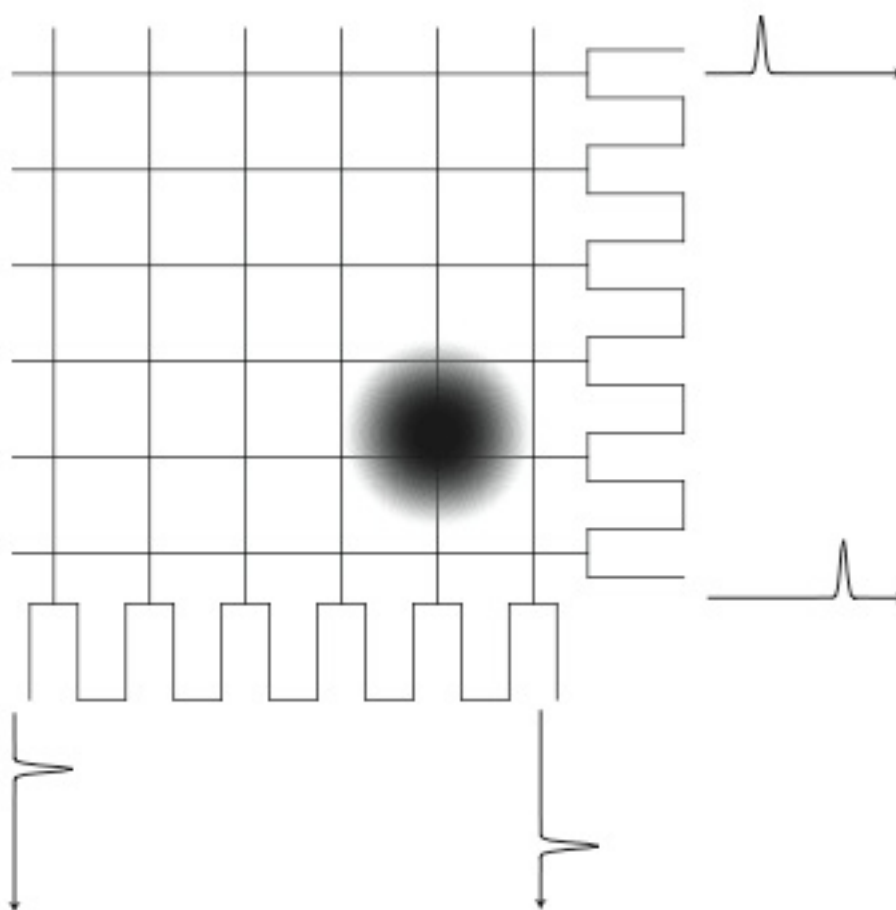


Figure 2.6: Delay line anode diagram. Incident charge (shown) is sampled by each delay line, producing pulses from either end of one line. The difference in time between these pulses encodes the position of the particle.

separate sets of electrodes, allowing for two-particle events,²¹ but the technique quickly becomes limiting. Thus, a different approach is taken for neutral particle detection, which allows detection of more than one particle in a single detector. This detector is known as the “crossed delay line” (XDL)^{22,23} and is composed of a grid of wires in the x- and y- directions, each set picking up a fraction of the charge from the MCPs and transmitting it to one of two serpentine delay lines as shown in Figure 2.6. Upon reaching the delay line, the charge splits and travels both directions to each end of the line, where the difference in time between the charge emerging from the ends is directly proportional to the location along the delay line that the initial charge cloud struck. By measuring the differences in time for these signals on the x- and y- delay lines, the particle impact location can be determined. Furthermore, if a second particle impacts the detector after the charge from the first has left the delay lines, its position can also be recorded, and so on. Absolute impact time of a particle can also be determined from these signals.

The implementation of this scheme in the current instrument further increases multiplicity and reduces dead time by employing four sets of delay lines in a quadrant configuration, called the quad crossed-delay-line (QXDL) detector.¹⁰ This strategy allows for up to 8 particles to be detected in coincidence, given appropriate kinematic constraints. Each quadrant is instrumented separately but identically for extraction of position and time for two particles. Signals from each end of each delay line are amplified in fast preamps, and fed into custom two-hit TACs. These TACs have start and stop inputs which are fed into two cascading sets of CFDs. The first start and stop CFDs output to the particle one TAC, while the second pair output to the particle two TAC.

Each of these TACs produce output voltages that are digitized by 12-bit ADCs. Timing information is taken from the first and second start CFDs of the y-coordinate TACs and fed to stops on a time-to-digital convertor (TDC) whose start is triggered by a pulse at some time delay after the laser shot. Additionally, the charge incident on each quadrant is amplified and digitized along with the total charge extracted from the MCPs in another ADC.

2.3.3. Data Acquisition System

The ADCs and TDCs for each detector are housed in a Computer-Automated Measurement and Control (CAMAC) crate which interfaces to a PC via a custom parallel port interface. Also in this crate is a counter which stores the number of laser shots since the beginning of a given trap cycle, in order to sort events by trapping time. A total of 34 channels of data are read, 8 each of QXDL x, y, and t, four quadrant charges, one total charge, three WSZ charges, one electron time signal, and the laser shot counter. The CAMAC crate is polled and read continuously, one event at a time, into a custom-written LabVIEW acquisition code that discriminates, histograms, and records events in quasi-real time. Values read from the ADCs and TDCs are first checked to fall within an acceptable range, and the channels in this range are tallied to determine the event multiplicity. If the multiplicity meets the requirements for the experiment, the data is stored to memory and written to disk at 5 minute time intervals. Otherwise, the data is thrown out. Stored data is also roughly converted on-the-fly into positions for display and diagnostics during the experiment, and histogrammed in on-the-fly as well for diagnostic purposes.

2.4. Data Analysis

The raw data produced by this data acquisition system is essentially unintelligible in its recorded form. These digital numbers must be discriminated to determine event multiplicity, converted to positions and times, and Newtonian mechanics calculations must be performed to get velocity vectors and correlations between electrons and particles. With these values calculated for each event, histograms can be created of virtually any observable or calculated quantity, or multi-dimensional set of these. A thorough understanding of the calculations involved allows relevant features to be separated from background processes such as falsely coincident events, multiple fragment mass channels, among others. Furthermore, features hidden in one way of looking at data may become apparent by looking at the data differently. The calculations involved in this are outlined in this section, along with strategies for maximizing the information that can be extracted from a data set.

2.4.1. Discrimination

The discrimination stage consists of two parts – first events are separated by multiplicity, i.e. electron only, N-particles only, and events with an electron and N-particles in coincidence. In order for a neutral particle hit to be counted, it must have valid x , y , and t data, while electrons must have valid Q_w , Q_s , and Q_z data along with a valid time. These events are grouped into separate data files corresponding to their multiplicity which can be later analyzed. Files are loaded into the analysis program according to user-selected multiplicity, at which point events pass through a second

discrimination step. Here each channel is compared to upper- and lower-level discriminators to remove contributions from data that is known to be bad, such as multi-electron events, neutrals from masses other than the target mass, electrons detached from pre- or post-pulses of the laser, and other known mechanisms.

2.4.2. Calibration

Once discrimination is finished, the resulting reduced dataset must be converted from uncalibrated integer numbers to positions and times. This procedure is significantly different between the two detectors due to the differences in their operating principles. The simplest calibration is for the neutral particle detector, which features a linear relationship between recorded value and temporal/spatial coordinates $\mathbf{x} = [x, y, t]$ given by

$$x_i = DMC_{x_i} * N + DAC_{x_i} \quad (2.1)$$

where DMC and DAC are the multiplicative and additive constants, respectively. In principle, for the time component, $DAC_t = \Delta t_{det} + TOF_{CM}$ where Δt_{det} is a calibration constant and TOF_{CM} depends on beam energy and parent mass.

The electron detector, working by charge division, is somewhat more complex. While in principle, the x and y positions of electrons are given by the ratios of wedge and strip charges, respectively, to the total charge on the anode, capacitive couplings between the anode segments prevents the straightforward conversion of these ratios to spatial

coordinates. Accounting for these “cross-talk factors,” the position of an electron impact can be approximated by

$$X = \frac{\left(\frac{Q_W}{Q_{tot}} - C_{ZW}\right) p_{x1} - p_{x2} \left(\frac{Q_S}{Q_{tot}} + C_{SZ}\right)}{p_{x3}} \quad (2.2)$$

$$Y = \frac{\left(\frac{Q_S}{Q_{tot}} - C_{SZ}\right) p_{y1} - p_{y2} \left(\frac{Q_W}{Q_{tot}} + C_{ZW}\right)}{p_{y3}} \quad (2.3)$$

and

$$p_{x1} = 1 - 2C_{SZ} - C_{WS} \quad (2.4)$$

$$p_{x2} = C_{WS} - C_{ZW} \quad (2.5)$$

$$p_{x2} = 1 - 2(C_{WS} + C_{SZ} + C_{ZW}) + 3(C_{WS}C_{ZW} + C_{SZ}C_{ZW} + C_{WS}C_{SZ}) \quad (2.6)$$

and the p_y constants can be obtained simply by swapping C_{SZ} and C_{ZW} . While these equations give particle impact positions, to obtain “effective” positions they must still be corrected for second-order effects and focusing effects of the VMI setup. Before these second-order corrections can be calculated, however, the electron time-of-arrival must be determined in a manner similar to the neutral detector,

$$TOF = DMC_t * N + DAC_t \quad (2.7)$$

which gives the true time of flight of the electron.

2.4.3. Neutral Fragment Kinematics

With the times and positions of arrival determined for all neutral particles, the laboratory frame velocity vectors can be calculated straightforwardly using simple kinematics. Since this thesis addresses only two-body neutral dissociation, all examples here will assume only two particles. For general three-body or symmetric four-body dissociation, see the theses of John Savee²⁴ or Todd Clements,²⁵ respectively. With the laboratory frame positions and times of arrival determined as described above, the three-dimensional particle velocities can be approximated by

$$v_x = x/TOF_{CM} \quad (2.8)$$

$$v_y = y/TOF_{CM} \quad (2.9)$$

$$v_z = v_{beam} * (TOF - TOF_{CM}) \quad (2.10)$$

for each particle hit. However, this set of equations does not account for the fact that particles ejected toward the detector have flight times less than the CM flight time, and particles ejected away have flight times that are longer. This causes particles ejected forward to arrive at the detector with smaller radii than they should have when the CM passes the detector, and the opposite effect for particles ejected backwards. While the effect is small for $KER < 1$ eV, it becomes noticeable and has been addressed in dissociative charge exchange experiments. A general geometric solution to correct for this problem has been developed and implemented for charge exchange experiments,²⁴

but has not yet been included in the analysis for these experiments due to its minimal impact.

These laboratory frame velocity vectors contain an inherent error due to the finite distribution of single-event CM trajectories, which causes an increased uncertainty in all momentum and energy calculations. In order to correct for this, the “true” CM can be calculated by guessing the masses of each particle, then enforcing conservation of momentum for each event, so that

$$\mathbf{r}_{lab} = \mathbf{r}_{CM} + \mathbf{r} \quad (2.11)$$

By subtracting the CM vector from each event, the blurring due to the CM trajectory distribution is eliminated, and the detector radial resolution approaches the fundamental spatial and temporal resolution of the system. With particle momentum vectors calculated, the total Kinetic Energy Release (KER) for the neutral particles can be expressed simply as

$$KER = \frac{p_1^2}{2m_1} + \frac{p_2^2}{2m_2}. \quad (2.12)$$

2.4.4. Electron Kinematics

Determination of the electron recoil velocities is less straightforward due to the inhomogeneous fields in the VMI detector, requiring careful correction and calibration of each electron dataset. Due to the focusing effects of VMI, electron velocities can not be calculated directly from the electron TOF. Therefore, an effective TOF is calculated as

$$TOF_{eff} = TOF - t_{cal} \quad (2.13)$$

which behaves as a scaling factor for x and y velocities, given by

$$v_x = x/TOF_{eff} \quad (2.14)$$

$$v_y = y/TOF_{eff} \quad (2.15)$$

In order to determine v_z , a phenomenological linearization is used

$$v_z = \frac{\Delta v_z}{\Delta TOF_{eff}} (TOF_{eff} - TOF_0) \quad (2.16)$$

where TOF_0 is the effective TOF for a zero-energy electron. As with the neutral particles, electron Kinetic Energy (eKE) is given by

$$eKE = \frac{m_e |\mathbf{v} - \mathbf{v}_{CM}|^2}{2} . \quad (2.17)$$

2.4.5. Gating

Many different types of gating are used, with the purpose of 1) reducing the contribution of bad data to the analysis, 2) improving the resolution of the experiment, 3) restricting the data used in the various histograms, and 4) selecting data from a specific range of trapping times of interest. When applied judiciously, these gating methods can significantly enhance the resolution of the experiment and the help resolve competing processes which might otherwise be indistinguishable.

Centroid gating – contributions from other mass channels and false coincidences can largely be removed by centroid gating. The centroids are the distributions or CM vectors as calculated above. Take the example of the following system:



In this system, where $m_A \neq m_B \neq m_C$, three separate processes can lead to two-particle events on the neutral detector, dissociation to $A + BC$; dissociation to $AB + C$; and false coincidences occurring, for example, when two ions are photodetached with one laser pulse, leading to two impacts of ABC . When analyzing data for channel $A + BC$, the improper assignment of masses to $AB + C$ and false coincidences typically causes these events to have wildly scattered CM vectors. By reducing the window of acceptable CM radii, the contribution of these events to the overall data can be minimized.

Mass gating – in cases where centroid gating is not selective enough, a second round of neutral gating can be imposed, in which ranges of apparent mass most closely matching the channel of interest are defined, and all events with apparent masses lying outside this range are thrown out. This gating method, while slightly less physically rigorous than centroid gating, can help to remove unwanted events which, purely coincidentally, have calculated CM radii within the centroid gate. This type of gating must be used carefully, however. In cases where the masses of the dissociation channel

are not well known, or incorrect, mass gating may lead to subjectively better-looking but significantly flawed analysis, in which “bad” events are treated as good data.

Time gating – a major advantage of performing the PPC experiment in the cryogenic trap is that data can be separated by amount of time in the trap. Not only does this allow the rejection of early trapping times, where ion cooling is expected to be most rapid, but it also allows data to be presented in intervals to reveal cooling dynamics and trap dynamics as a function of trapping time.

Slicing – For electron detector calculations, the uncertainty in timing is significantly larger than the uncertainty in position. This uncertainty is primarily due to the poor dynamic range of the timing measurements (~ 200 ps resolution over a several ns full range), but also nonlinearities in the $t \rightarrow v_z$ conversion which are not accounted for in the kinematic calculations. The overall error in calculations of the magnitude of the velocity vector can be given by

$$\frac{\delta E}{E} \propto \frac{2(v_x \delta v_x + v_y \delta v_y + v_z \delta v_z)}{v_x^2 + v_y^2 + v_z^2} \quad (2.18)$$

so if the error in v_z is largest, it is clear that selecting a subset of the electrons with $v_z \sim 0$ yields a photoelectron spectrum of highest resolution. However, this process significantly reduces the signal-to-noise of the photoelectron spectrum and must be used with care. Additionally, slicing modulates the relative intensity of the spectrum as a function of eKE and ejection angle θ , since more low-energy electrons and electrons emitted along the laser vector are retained by a given slice than high-energy or

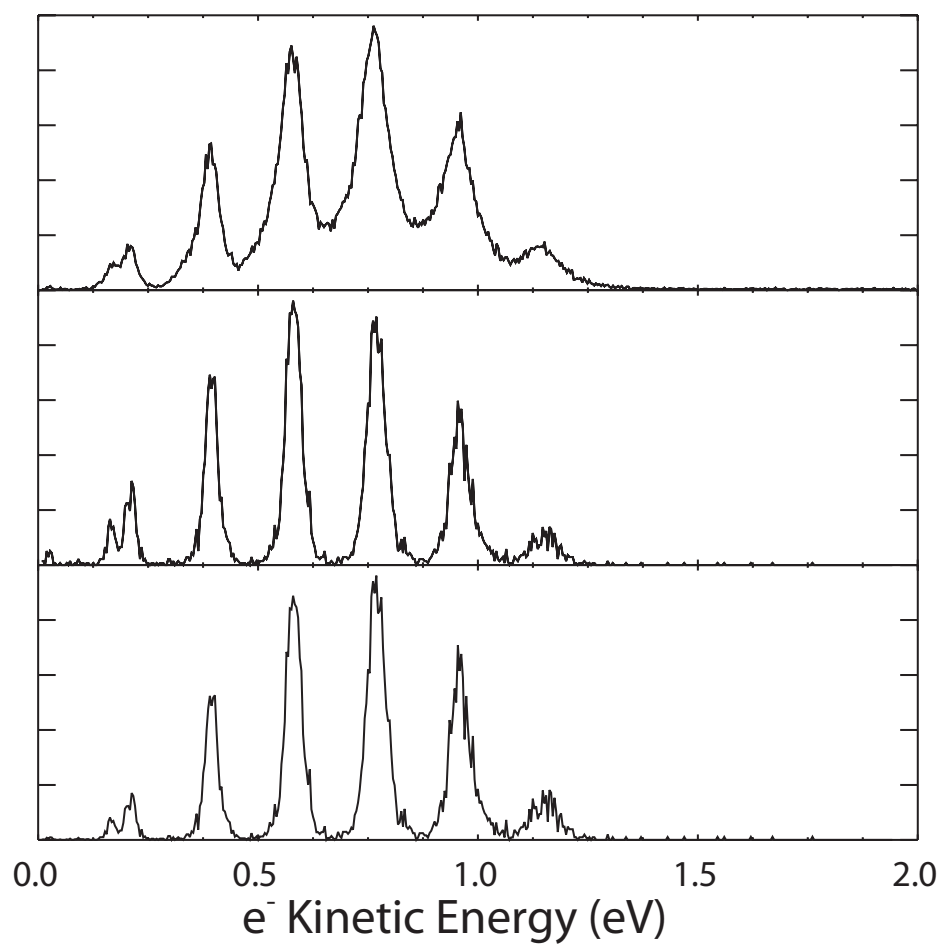


Figure 2.7: An example of the efficacy of slicing and the slice correction. The raw spectrum is shown on top, the sliced spectrum in the middle, and the sliced and corrected spectrum on the bottom. Note the change in the weighting of the peaks from unsliced to sliced, and the reproduction of this weighting by the correction.

perpendicular electrons. Correction of this issue is accomplished by a simple geometric calculation of the “slice acceptance function” (SAF) that gives the probability of an electron

$$SAF = \begin{cases} \frac{2}{\pi} \arcsin \frac{v_z^{slice}}{|\mathbf{v}| \sin \theta}, & |\mathbf{v}| > v_z^{slice}, \theta(|\mathbf{v}|) > \theta^{slice}(|\mathbf{v}|) \\ 1, & |\mathbf{v}| \leq v_z^{slice} \\ 1, & \theta(|\mathbf{v}|) \leq \theta^{slice}(|\mathbf{v}|) \end{cases} \quad (2.19)$$

which yields a “slice acceptance function” that can be applied to a sliced photoelectron spectrum to recover the correct intensities at each energy. The effects of slicing and SAF correction are shown in Figure 2.7.

2.4.6. Coincidence Calculations

With the fragment kinetic energies and electron energy computed, the total energy release can be calculated by

$$E_{tot} = eKE + KER \quad (2.20)$$

which, when histogrammed, gives a spectrum that directly reflects the total internal energy of the fragments

$$E_{int} = h\nu - AEA - D_0 - E_{tot} \quad (2.21)$$

and features in this spectrum correspond to internal coordinates of the fragments.

Often, a more illuminating way to look at the data is the coincidence spectrum, which is a two-dimensional histogram showing the probability of obtaining a given

combination of eKE and KER. For each set of final electronic states of product fragments, a diagonal line exists on the coincidence plot marking the maximum total energy for creation of those products. When integrated along the diagonal axis, this spectrum gives the total energy spectrum, but it contains much more information than the total energy spectrum. For instance, the position of a signal along a given diagonal directly reports the energy of the Franck-Condon region above the associated repulsive curve's asymptotic energy. Processes that would not necessarily be separable in a single-dimensional technique can be easily identified in coincidence spectra. Examples include electron autodetachment following direct ionic photodissociation, which appears as horizontal stripes at low eKE, and sequential or coherent multi-photon absorption, which can give vertical features. Additionally, false coincidence events and events ascribed to the wrong combination of masses can typically be identified in coincidence spectra due to odd patterns which do not match known physical phenomena and which also do not behave properly with gating as described above.

2.4.7. Photoelectron Angular Distributions

By employing the velocity map imaging technique for photoelectron detection, the angular distribution of photoelectrons (PAD) with respect to the laser polarization vector can be determined. In principle, for detachment of an electron from a singly charged anion by a single linearly polarized photon, the PAD is given by

$$I(\theta) \propto 1 + \beta_2 P_2(\cos \theta) \quad (2.22)$$

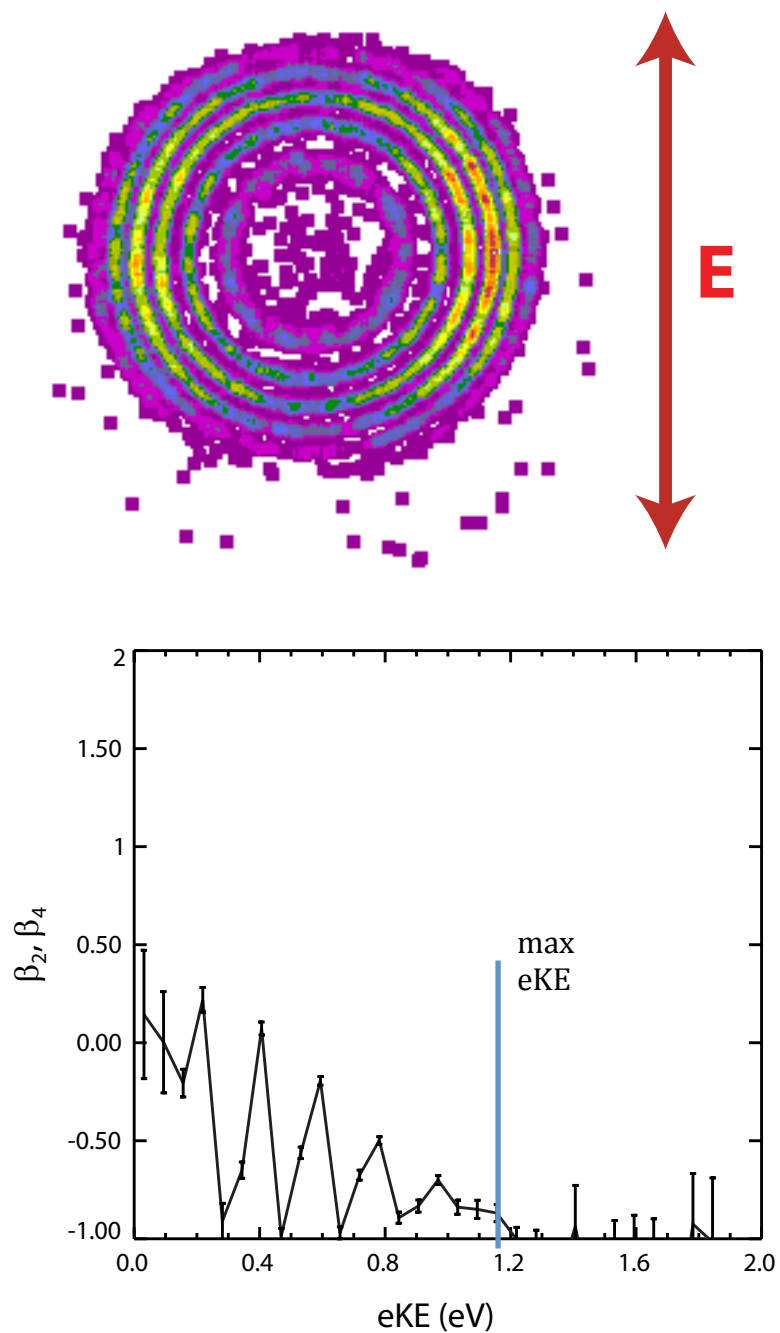


Figure 2.8: Sliced photoelectron image for O_2^- photodetachment at 775 nm (top). Corresponding $\beta(\text{eKE})$ (bottom).

where θ is the angle between the polarization vector and the electron velocity vector and β_2 is an asymmetry parameter which can be rigorously calculated for atomic anions but is only qualitative for molecular anions.^{26,27} Energy-resolved PADs can be fit to this equation to reveal the evolution of β_2 as a function of electron energy and the allowed values of β_2 span the range from 2 to -1, corresponding to distributions given by $\cos^2\theta$ and $\sin^2\theta$, respectively, for a one-photon transition. An example, from photodetachment of O_2^- at 1.60 eV, is shown in Figure 2.8. Here the angular distribution is peaked primarily perpendicular to the laser polarization vector, consistent with interfering partial waves of opposite polarity centered at each O atom.

In a two-photon process, the dipole selection rules for linear polarization are $\Delta l = 0, \pm 1$, and the additional electron angular momentum allows for higher anisotropy in the PAD, which now is characterized by

$$I(\theta) \propto 1 + \beta_2 P_2(\cos \theta) + \beta_4 P_4(\cos \theta) \quad (2.23)$$

and can be fit similarly to the one-photon case. Unfortunately, no systematic method to relate these two-photon PADs to molecular orbitals yet exists. It is possible to decompose the PAD to spherical harmonic partial waves by

$$I(\theta, E) \propto \left| c_{00}(E)e^{i\delta_0(E)}Y_{00} + c_{20}(E)e^{i\delta_2(E)}Y_{20} \right|^2 \quad (2.24)$$

where only $m_l = 0$ remains for linearly polarized light.²⁸ Since only two parameters, β_2 and β_4 , exist in the fit, only two relative values for the partial wave coefficients can be determined, namely the ratio of partial wave amplitudes

$$\frac{c_{20}}{c_{00}} = \left(\frac{18}{7\beta_4} - 1 \right)^{-\frac{1}{2}} \quad (2.25)$$

and the relative phase shift

$$\cos(\delta_0 - \delta_2) = \frac{\frac{c_{20}}{c_{00}} \left(\frac{9\beta_2}{\beta_4} - 5 \right)}{7\sqrt{5}} \quad (2.26)$$

which is sufficient to recreate the PAD in the spherical harmonic basis. A phenomenological approach will be outlined in Chapter 8 of this thesis for reproducing these PADs given basic information on the molecular orbital of the anion from which an electron is detached.

References

- (1) Dahan, M.; Fishman, R.; Heber, O.; Rappaport, M.; Altstein, N.; Zajfman, D.; van der Zande, W. *Rev. Sci. Instrum.* **1998**, *69*, 76.
- (2) Andersen, L.; Heber, O.; Zajfman, D. *J. Phys. B-At. Mol. Opt.* **2004**, *37*, R57.
- (3) Zajfman, D.; Rudich, Y.; Sagi, I.; Strasser, D.; Savin, D.; Goldberg, S.; Rappaport, M.; Heber, O. *Int. J. Mass. Spectrom.* **2003**, *229*, 55.
- (4) Bhushan, K. G.; Gadkari, S. C.; Yakhmi, J. V.; Sahni, V. C. *Rev. Sci. Instrum.* **2007**, *78*, 083302.
- (5) Greenwood, J. B.; Kelly, O.; Calvert, C. R.; Duffy, M. J.; King, R. B.; Belshaw, L.; Graham, L.; Alexander, J. D.; Williams, I. D.; Bryan, W. A.; Turcu, I. C. E.; Cacho, C. M.; Springate, E. *Rev. Sci. Instrum.* **2011**, *82*, 043103.
- (6) Pedersen, H.; Strasser, D.; Amarant, B.; Heber, O.; Rappaport, M. L.; Zajfman, D. *Phys. Rev. A* **2002**, *65*, 042704.
- (7) Pedersen, H.; Strasser, D.; Ring, S.; Heber, O.; Rappaport, M. L.; Rudich, Y.; Sagi, I.; Zajfman, D. *Phys. Rev. Lett.* **2001**, *87*, 055001.
- (8) Pedersen, H.; Strasser, D.; Heber, O.; Rappaport, M. L.; Zajfman, D. *Phys. Rev. A* **2002**, *65*, 042703.
- (9) Attia, D.; Strasser, D.; Heber, O.; Rappaport, M. L.; Zajfman, D. *Nucl. Instrum. Meth. A* **2005**, *547*, 279.
- (10) Hanold, K.; Luong, A.; Clements, T.; Continetti, R. *Rev. Sci. Instrum.* **1999**, *70*, 2268.
- (11) Smalley, R.; Ramakris, B. L.; Levy, D.; Wharton, L. *J. Chem. Phys.* **1974**, *61*, 4363.
- (12) Levy, D. *Annu. Rev. Phys. Chem.* **1980**, *31*, 197.
- (13) Lu, Z.; Continetti, R. *J. Phys. Chem. A* **2004**, *108*, 9962.
- (14) Lu, Z.; Hu, Q.; Oakman, J. E.; Continetti, R. E. *J. Chem. Phys.* **2007**, *126*, 194305.
- (15) Continetti, R.; Cyr, D.; Neumark, D. *Rev. Sci. Instrum.* **1992**, *63*, 1840.
- (16) Bakker, J. *J. Phys. E-Sci. Instrum.* **1974**, *7*, 364.

- (17) Eppink, A.; Parker, D. *Rev. Sci. Instrum.* **1997**, *68*, 3477.
- (18) Neumark, D. M. *J. Phys. Chem. A* **2008**, *112*, 13287.
- (19) Martin, C.; Jelinsky, P.; Lampton, M.; Malina, R.; Anger, H. *Rev. Sci. Instrum.* **1981**, *52*, 1067.
- (20) Siegmund, O.; Clothier, S.; Thornton, J.; Lemen, J.; Harper, R.; Mason, I.; Culhane, J. *IEEE T. Nucl. Sci.* **1983**, *30*, 503.
- (21) Continetti, R.; Cyr, D.; Osborn, D.; Leahy, D.; Neumark, D. *J. Chem. Phys.* **1993**, *99*, 2616.
- (22) Lampton, M.; Siegmund, O.; Raffanti, R. *Rev. Sci. Instrum.* **1987**, *58*, 2298.
- (23) Siegmund, O.; Lampton, M.; Raffanti, R.; Herrick, W. In *Nuclear Instruments & Methods in Physics Research Section A-Accelerators Spectrometers Detectors and Associated Equipment*; 1991; Vol. 310, pp. 311–316.
- (24) Savee, J. D. An Experimental Probe of Electronic Interactions in Excited Molecules Produced By Charge Exchange, University of California, San Diego, 2009, pp. 1–235.
- (25) Clements, T. G. Multi-Body Dissociative Photodetachment Dynamics of Small Molecular and Cluster Anions, University of California, San Diego, 2002, pp. 1–456.
- (26) Cooper, J.; Zare, R. *J. Chem. Phys.* **1968**, *48*, 942.
- (27) Ritchie, B.; *Phys. Rev. A* **1976**, *13*, 1411.
- (28) Reid, K. L.; *Annu. Rev. Phys. Chem.* **2003**, *54*, 397.

Chapter 3. Photoelectron-Photofragment Coincidence Spectroscopy in a Cryogenically Cooled Linear Electrostatic Ion Beam Trap

3.1. Introduction

Since its introduction in the late 1990s,^{1,2} the electrostatic ion beam trap (EIBT) has found a variety of uses in ion spectroscopy,³⁻⁵ dissociation dynamics,^{6,7} and mass spectrometry.⁸⁻¹⁰ This type of device, which allows the storage of a fast (keV) beam of ions for seconds or longer, is a relatively simple and compact alternative to magnetic or electrostatic ion storage rings.¹¹ Several favorable properties, such as a large field-free region at the center of the trap and the ability to cool the entire apparatus,¹² make it a favorable platform for the integration of targets¹³ and detectors⁶ to study processes occurring in ionic systems. Here we report the adaptation of an existing photoelectron-photofragment coincidence (PPC) spectrometer to include a cryogenically-cooled EIBT, allowing PPC experiments to be performed on cold molecular anions and enhancing the ability to energetically resolve the dissociation dynamics of neutral molecular reaction intermediates and clusters.^{14,15}

The use of translationally and internally cold neutral molecular beams has, over the last few decades, become a standard element of many gas-phase experiments. Supersonic jet expansions have been shown to produce molecules with vibrational temperatures below 100 K and rotational temperatures below 20 K, enabling extremely

high-resolution spectroscopy to be carried out in the gas phase on a wide variety of cold molecular and cluster systems.¹⁶ However, in the case of molecular ion beams the ionization process can reintroduce significant amounts of internal energy, particularly into vibrational degrees of freedom. For molecular ions that are efficiently created only late in the expansion or through multi-step ion chemistry, some internal degrees of freedom remain excited, giving rise to characteristic “hot bands” in spectra. Significant internal excitation in anion precursors complicates analysis of photoelectron and photofragment kinetic energy spectra. Examples from this laboratory include studies of the acetyloxyl radical,¹⁷ which was found to have up to 0.2 eV of extra internal energy residing in the precursor anion,¹⁸ and the HOCO radical,¹⁹ which was shown using the instrument described here to have contained as much as 0.6 eV of internal excitation in the HOCO anion.¹⁴ Though this would seem to be an extreme amount of internal excitation, in small molecules the formation and vibrational energy redistribution mechanisms can be highly non-statistical, leading to large disparities between energy partitioning among internal degrees of freedom²⁰ and the inapplicability of the concept of temperature and thermal equilibrium among the degrees of freedom of a single molecule. Thus, in discussions here the term cooling should be interpreted loosely as the process of removing energy from the molecule.

Several approaches have been employed to reduce the effects of internal excitation. Cold ions can be generated by argon or hydrogen solvation, in which the weakly-bound solvent is clustered with ions prior to mass selection.^{21,22} Evaporation of the solvent removes heat from the ion, setting an upper limit to the internal energy (temperature) of the ion.²³ The solvent has been shown to exert a small influence on the

spectroscopy of the ion in most cases, allowing for high-resolution measurements. Nanodroplet spectroscopy, a similar technique in which molecules are cooled by insertion into a large cluster of atoms, typically helium, has also shown the ability to produce high-resolution spectra of cold neutral molecules and ions.²⁴⁻²⁷ Another technique employs a radiofrequency ion trap to store ions in a cryogenic environment surrounded by a cold buffer gas prior to measurement.^{28,29} In these conditions thermalization of ions with the buffer gas removes internal excitation from the ions over a period of several tens or hundreds of milliseconds. Once cold, experiments are either conducted inside the trap, or the ions may be extracted for further measurements.^{30,31}

Unfortunately, these techniques are not suited for the photoelectron-photofragment coincidence (PPC) experiments performed in this laboratory.³² PPC spectroscopy is a kinematically complete experiment in which dissociative neutral intermediates of known internal energy are created by photodetachment of an electron from a stable molecular anion. By collecting all resultant neutral fragments from the dissociation event in coincidence with the detached electron using time- and position-sensitive detectors, the correlated momenta and energies of all products can be calculated. This technique provides insight into the electronic structure of the parent anion and neutral species as well as the energy-resolved dynamics on the neutral potential energy surface. Coincidence experiments generally require a high duty cycle and low event rate to avoid contamination of data due to false coincidences, and thus low-repetition-rate techniques such as nanodroplets and radiofrequency ion traps may necessitate significantly longer acquisition times or increased difficulty in separating false coincidence events than current methods. Further, the addition of an extra body in Ar-

tagging methods requires increased complexity in data analysis for multiparticle three-dimensional fragment imaging techniques and a reduction in overall detection efficiency per event due to the efficiency of microchannel plates. Finally, none of these techniques allow PPC experiments to be performed on ions as they cool and thus information related to the cooling process itself is lost.

In order to address these issues we have adapted an EIBT for use in PPC experiments. This trap is a type of focusing linear double-reflectron setup analogous to an optical resonator. Under ultrahigh vacuum conditions, this trap is capable of storing ion beams for many seconds. The EIBT is ideal because it can maintain ions in collimated, beam-like trajectories required for translational spectroscopy experiments and features a large field-free region in the center of the trap that can be used for electron detection. These features allow experiments to be performed on ions while they are trapped, providing the high (kHz) duty cycle required for coincidence experiments without the need to repeatedly cool ions on the hundred microsecond timescale. Furthermore, this type of trap is compact and relatively simple to construct and operate, making integration with the current experiment straightforward.

This EIBT has also been constructed to enable the mirror elements and surrounding blackbody radiation shields to be cooled to cryogenic temperatures, ensuring that trapped ions have minimal exposure to room temperature radiation. Under these conditions the stored ions can radiatively decay to ground or near ground vibrational and rotational levels on millisecond to second time scales. Additionally, the use of an intense, low-repetition-rate supersonic source allows inherently colder ions to be generated and injected into the trap. This allows study of the DPD of precursor anions

with well-characterized internal energy distributions, giving increased energetic accuracy, and opens new avenues of investigation that were not practical in a single-shot PPC instrument, such as the cooling processes of ions with long-lived ro-vibrational states and controlled internal excitation of anions prior to photodetachment.

3.2. Experimental

The cryo-PPC spectrometer consists of the same ion source and time-of-flight mass spectrometer previously reported³³ with virtually no modifications, and is depicted in Figure 3.1. Anions are synthesized in a 10 Hz pulsed supersonic expansion with a coaxial pulsed discharge crossed by a 1 keV electron beam, which can subsequently be intersected by a second pulsed supersonic beam if needed. This expansion is skimmed, accelerated to 4-12 keV, and rereferenced to ground in a fast potential switch. Anion packets typically 2-5 μs in length are separated by time of flight and guided into an electrostatic chopper (“mass gate”) consisting of two parallel electrodes biased at ± 450 V to deflect ions into a microchannel plate (MCP) based timing detector, and pulsed to ground to allow the mass of interest to pass into the trap. The entrance mirror and lens are held at ground until the ion packet is fully in the trap cavity, and are then quickly switched to operational potential using fast high voltage switches. Ions with proper trajectories are stored in the trap and are lost primarily due to collisions with background gas. Trapped ions are bunched and phase-locked to a modelocked kHz laser using a small RF potential on a coaxial cylindrical electrode, and ion bunch evolution is monitored using a charge-sensitive preamplifier (Amptek A250) attached to another coaxial electrode.^{1,34} Photodetached electrons are detected intracavity, while resulting neutrals are collected downstream from the trap. Data from each detector is collected in

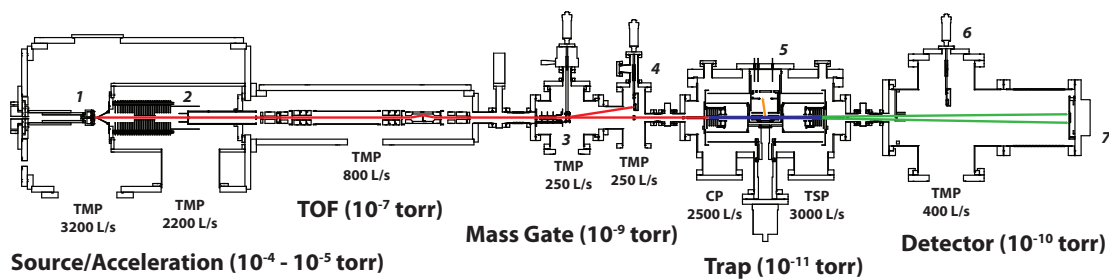


Figure 1.1: Overview of the cryo-PPC instrument. Labeled components are 1. Pulsed valve/discharge assembly, 2. Acceleration stack and potential switch, 3. Electrostatic chopper, 4. Pre-trap ion detector, 5. Electron detector, 6. Post-trap ion detector, 7. Neutral particle detector.

coincidence, along with a timestamp for the amount of time trapped, using a CAMAC-based data acquisition system connected to a personal computer.

3.2.1. Trap design

The overall design of the ion trap assembly is shown in Figure 3.2. The plate thickness, spacing, and hole diameters of the individual electrodes in the mirror assemblies are identical to those previously described by the Zajfman group.² These mirror assemblies consist of a stack of reflecting electrodes coupled to a cylindrical electrostatic lens, with grounded electrodes at the front and rear of each assembly. Electrode spacing is set using insulating sapphire balls to enhance thermal conductivity. Each assembly is individually mounted to a vacuum flange via a thermally insulating system analogous to an optical kinematic mount, with a ball-bearing pivot and two linear manipulators at opposite corners to allow inclination about two axes. This design permits precise control of mirror alignment while the trap is under vacuum, alleviating the need to carefully control thermal contraction during temperature cycling. The angular resolution of this system is < 0.3 mrad. The total length of the trap cavity is 50 cm measured from the back of the first ground plate on the entrance mirror to the same plate on the exit mirror.

Two sets of radiation shields surround the trap cavity and are mounted directly on a closed-cycle He refrigerator (Austin Scientific, CryoPlex 1020). The inner set, held at ~ 20 K, consists of cylindrical surfaces attached to a copper platform directly connected to the 2nd stage of the cryocooler. These cylindrical surfaces are attached to the rear grounded electrodes of the trap mirrors by several layers of flexible copper foil to provide good thermal contact throughout the 20 K region. Surrounding this assembly is a second

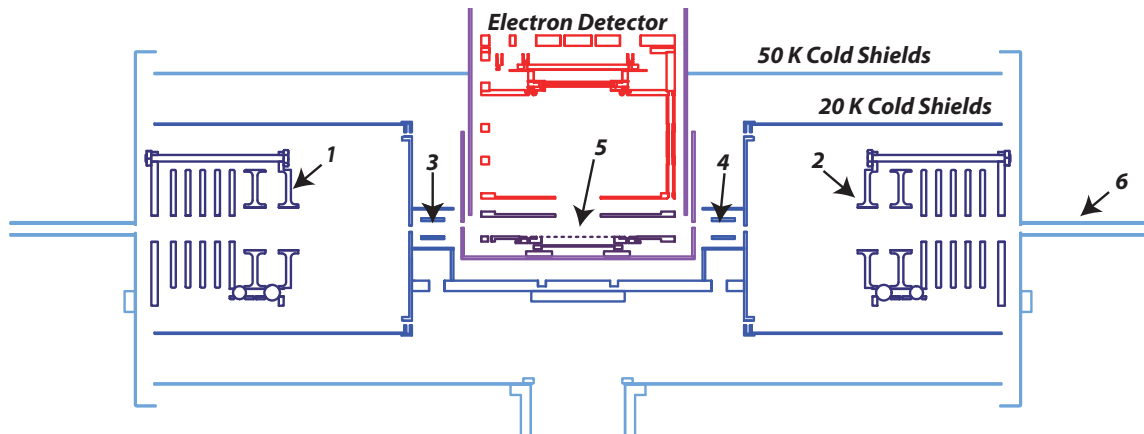


Figure 3.2: Detailed diagram of the trap assembly. Labeled components are 1. Entrance mirror, 2. Exit mirror, 3. Bunching electrode, 4. Pickup electrode, 5. Laser-ion interaction point, 6. Coaxial blackbody radiation baffles. Elements in dark blue are nominally 20 K, elements in light blue are nominally 50 K, and red is nominally room temperature. The magnetic shields span the 20 – 50 K range, and are shown in purple. Mirror electrode voltages are ordered in the same manner described in Ref. 2.

set of polished copper shields attached to the 1st stage of the cryocooler and typically held at ~50 K. These shields are also connected via stacked copper foils to a set of copper endcaps attached to the mirror assemblies, to reduce the heat load on the cold mirrors and eliminate line-of-sight from the room-temperature vacuum chamber to 20 K elements.

Trapping voltages are transferred to the mirrors by 0.8 mm diameter bare stainless steel wires to reduce thermal conductivity from the room-temperature feedthrus. The voltage on the trap lenses is provided by a high voltage power supply (Bertan 210B) attached directly to the exit side lens and through a fast push-pull high voltage switch (Behlke HTS series) on the entrance side lens to allow grounding during ion injection. Mirror voltages are generated by voltage division of the output of another high voltage power supply (Matsusada AE series) in a V, V/2, V/4, V/8 arrangement, again acting directly upon the exit mirror and through another fast HV switch on the entrance mirror. The slow RC time constant of the lower voltage electrodes is bypassed by the innate capacitance of the mirror plates and wiring, and tuning of the capacitance of the voltage divider allows all plates to be switched to full stable voltages with minimal drift well before the first recurrence of the ion packet in the trap.

3.2.2. Vacuum system

Since trapping lifetimes are inversely proportional to background pressure in this type of trap, pressures below 10^{-10} torr are essential to allow trapping for several seconds.² The trap assembly is housed within a custom-built 603 mm ID wire-seal vacuum chamber pumped by a 2500 L/s cryopump (Austin Scientific CP-8) and a home-built 3000 L/s titanium sublimation pump. Additional pumping occurs, when the entire assembly is cooled, by cryosorption of gases onto the system itself. Pressures are

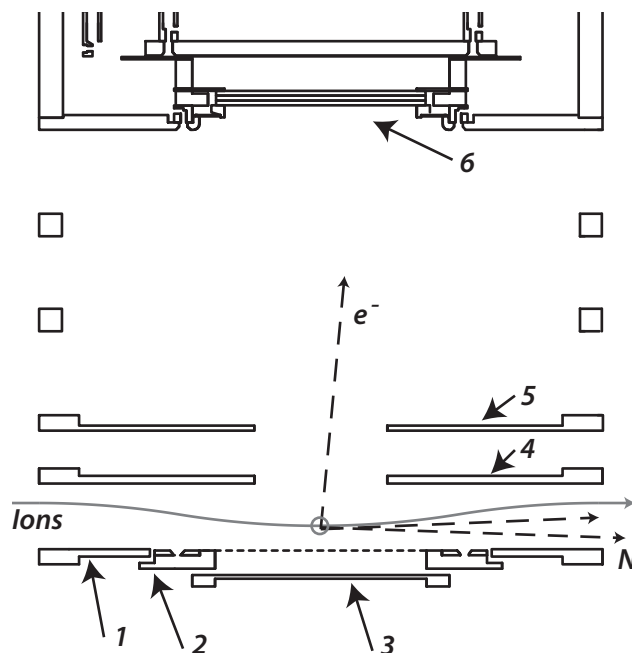


Figure 3.3: Detail of the interaction region and electron detector. The interaction point is shown with a gray circle, and example electron (e^-) and neutral fragment (N) trajectories are shown. Labeled components are 1. Ion correction plate (positive bias), 2. Repeller plate and central grid (negative bias), 3. Electron background reducer plate (positive bias), 4. Extraction lens (grounded), 5. Focusing lens (positive bias), 6. Microchannel plates for electron detector. All parts have cylindrical symmetry. The ion trajectory through this region is exaggerated for clarity.

monitored using a UHV ion gauge (Varian) with an x-ray background of 6×10^{-12} torr, and typical base pressures of 4×10^{-11} torr are achieved after several days under vacuum.

The ion beam apparatus is constructed with several stages of differential pumping ensuring a low gas load from upstream sections by use of a 3 mm aperture between the mass gate and trap regions. A much larger 12 mm aperture must be used to separate the neutral detector chamber from the trap chamber in order to expose the full field of view of the multiparticle detector to the recoiling neutral particles, requiring lower pressures in the detector chamber. Experimental loads from these chambers typically raises the background pressure in the trap chamber by $1-2 \times 10^{-11}$ torr.

3.2.3. Synchronization with pulsed laser

In order to ensure high ion density and good temporal overlap of oscillating ion pulses with the intersecting laser pulses, a stable bunching and synchronization scheme is required, with timings shown diagrammatically in Figure 3.4. By applying a small RF field, at the fundamental (typically ~ 100 kHz) or a harmonic of the natural ion oscillation frequency, on a cylindrical electrode on the oscillation axis, ions can be forced to bunch in packets typically < 200 ns long. This also eliminates detachment signal from anions travelling in the reverse direction in the trap, increasing the coincidence rate of the experiment and removing a significant Doppler offset in photoelectron images as seen in Figure 3.5. Triggerable kHz q-switched lasers can be simply used by prescaling the RF frequency to an appropriate value for use as the laser repetition rate. However the use of femtosecond or picosecond modelocked lasers is more complex due to the constraint that the laser repetition rate must be fixed to a divisor of the laser master oscillator frequency and thus is only coarsely adjustable.

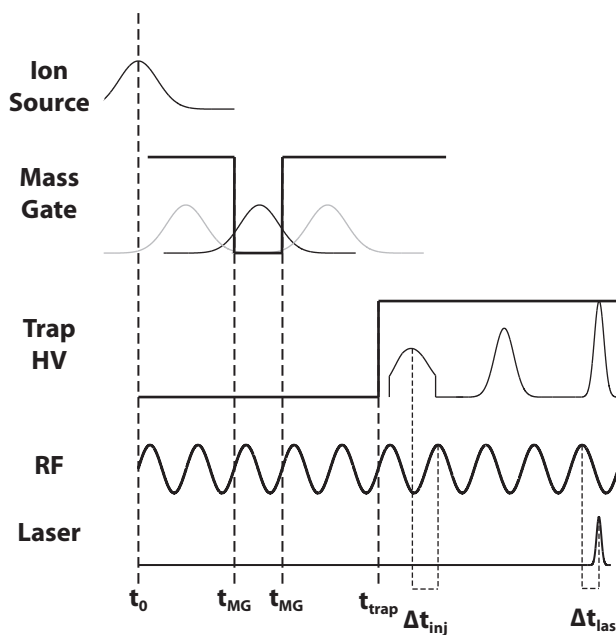


Figure 3.4: Timing diagram showing the propagation of an ion pulse through the instrument and the relevant pulse times (long dashed lines), where t_0 is the time at which the beam potential is switched, t_{MG} is the mass gate opening and closing, and t_{trap} is the trap closing. The phases important to proper synchronization, the RF-injection phase (Δt_{inj}) and RF-laser phase (Δt_{las}), are denoted with short dashed lines. The rate of ion bunch evolution is greatly exaggerated.

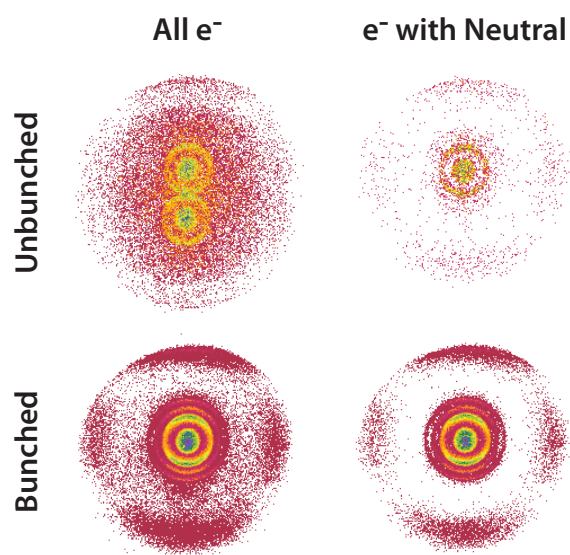


Figure 3.5: Example of unbunched and bunched photoelectron images for photodetachment of DOCO^- at 775 nm. For each set of conditions, the images in the first column are of all electrons, regardless of neutral signal, while the second column images are from events with one neutral particle detected in coincidence. In these images, a signal present at large radii arising from two-photon absorption by a single ion is intentionally cut by the edge of the detector, allowing enhanced resolution for low-energy electrons.

To maintain consistent phaselocking of the bunching RF field to the pulsed laser, the bunching signal must be driven by the master oscillator of the laser and the ion oscillation frequency tuned to resonance with this signal by optimizing the beam energy. The system implemented for this purpose, outlined in Figure 3.6, begins with integer division and multiplication of the laser master oscillator frequency, generating a phaselocked signal that can be used to override the reference oscillator of an analog function generator (HP 3325B). This forces the function generator output to be phaselocked to the laser repetition rate and allows simple control over the laser-RF phase and the RF amplitude through normal function generator operation. The current laser systems used are a Ti:Sapphire regenerative amplifier (Clark-MXR, CPA2000) seeded by a 43.58 MHz diode-pumped Kerr-lens-modelocked fiber oscillator, and an actively modelocked, q-switched, cavity dumped Nd:YAG (Quantronix 116) with a cavity frequency of 50.01 MHz. The Ti:Sapphire system will be used as the example for the synchronization system, though the approach is essentially the same for either laser. The fiber oscillation rate is prescaled by 42,000 to drive the regenerative amplifier system, leading to a repetition rate of 1038 Hz. By multiplying the fiber oscillator frequency by $5/7$, a phaselocked 31.13 MHz signal is obtained which drives the nominally 30.00 MHz reference oscillator of the function generator, with a factor of 1.038 (by definition exactly the laser rate divided by 1000) relating the two. Thus any frequency input to the function generator that is an integer multiple of 1000 will automatically induce bunching at an integer multiple of the laser repetition rate. In this case, the “frequency” entered into the function generator is actually the number of RF periods per laser shot x 1000, which when scaled by 1.038 gives the precise bunching frequency. The function generator

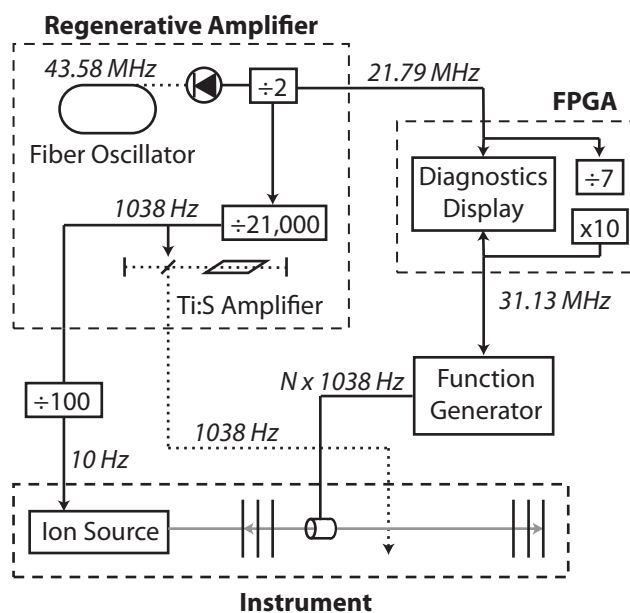


Figure 3.6: Diagram of the phaselocking system. Solid connectors represent electrical signals and dotted connectors represent laser light.

reference frequency is synthesized in the phase-locked loop segments of a field-programmable gate array (Altera Cyclone II), which also provides diagnostic systems. This synchronization technique typically results in a ~ 10 ns RMS jitter between the RF and laser pulse phases, with a phase resolution of 0.03% of the RF period. Bunching at the second harmonic of the ion oscillation frequency has been found to produce temporally shorter ion bunches with negligible impact on the laboratory frame energy distribution of trapped ions (see Sec. 3.3.3).

3.2.4. Intracavity electron detector

The field-free nature of the center of this type of trap allows relatively simple integration of a velocity-map imaging (VMI)³⁵ photoelectron detector in the trap cavity. Electrons are extracted perpendicularly to the laser-ion plane, with electric fields in the interaction region typically ~ 10 V/cm. Deflection of the ion beam by the extraction field requires correction of the ion trajectories in order to maintain stable trapping. This is accomplished by splitting the repeller in standard VMI designs into two concentric discs, a repeller and corrector, with opposite polarities. As ions traverse this region, they are first deflected downward by the first correction field, then deflected upward by the repeller and leveled by the second correction field. Proper adjustment of voltage of the correction plate allows undetached ions to exit the electron detector on the same trajectory they entered, while still providing a homogeneous repeller field to extract electrons to the detector, and ensuring the neutral center-of-mass recoil trajectory remains parallel to the ion beam. Vertical deflections of ~ 0.5 mm are calculated for typical ion masses and beam energies. Additionally, the central area of the repeller is composed of a 90% transmissive grid with a positively biased plate underneath, a design that has been

shown to significantly reduce electron background from scattering of photons in ultraviolet experiments.³⁶

The VMI extraction optics are held at ~ 20 K, and the entire photoelectron spectrometer is encased in a magnetic shield composed of Cryoperm-10 on the cold side and mu-metal on the warm side (Amuneal, Inc.). Since the detectors used in these experiments are time- and position-sensitive, the VMI geometry has been optimized to increase the dynamic range for the electron time of arrival, enhancing timing resolution. The detector is composed of a Z-stack of microchannel plates (MCPs) whose emitted charge is detected by a wedge-and-strip anode³⁷ to determine position of arrival, and capacitively coupled to a fast amplifier feeding a constant fraction discriminator and time-to-amplitude converter for timing measurement, as previously described.³³

3.2.5. Experimental details

All timing signals for source, mass gate, and trap triggers are controlled by a digital delay generator (Stanford Research DG645) triggered by and prescaled to $1/100^{\text{th}}$ of the laser repetition rate (~ 10 Hz) to achieve consistent timing between ions, RF bunching, and laser pulses. The ion beam energy must be tuned to produce a natural oscillation frequency close to the bunching frequency, with example oscillation frequencies for a number of ions shown in Table 3.1. Optimization of the synchronization system involves two phases with respect to the RF signal: 1) the phase at which ions are injected, controlled by the digital delay generator, and 2) the phase at which the laser pulse crosses the ion beam, controlled by the function generator. Laser pulses are injected perpendicular to the trap axis in the center of the trap, and focused to a

Table 3.1: Selected ion oscillation frequencies for given trapping voltages and beam energies.

Anion	Mass (amu)	Freq. (kHz)	Voltages (V)		
			Beam	Mirror	Lens
O^-	16	259.50	6874	10500	6360
O_2^-	32	184.70	7034	10580	6524
$HOCO^-$	45	154.45	6903	10550	6467
$DOCO^-$	46	152.55	6820	10550	6294
NO_2^-	46	153.63	6937	10550	6421
O_4^-	64	130.14	6996	10550	6468
$C_4H_9O^-$	73	121.50	6875	10550	6337

diameter of less than 1 mm. Neutral particles resulting from photodetachment recoil over a 1.29 m flight path along the trap centerline with a center-of-mass velocity equal to the beam velocity and are detected by another 40 mm MCP based time- and position-sensitive quad-delay-line multiparticle detector.³³ Data is acquired on an event-by-event basis in a similar system to that described previously. In order to group events by trapping time, each laser pulse increments a CAMAC counter, which is reset for each trap injection. Recording this count for each event allows for trap time gating of data during analysis and also allows dynamics to be monitored as a function of trapping time.

3.3. Results

3.3.1. Trapping lifetimes

No detailed study of trapping lifetimes has been performed on this instrument, however approximate lifetimes can be extracted directly from PPC data by binning photoelectrons as a function of trapping time. Several example systems are shown in Figure 3.7, revealing exponential lifetimes on the order of seconds at pressures in the high 10^{-11} torr range. Since the data use for lifetime extraction is taken from bunched experiments, the first 500 ms are ignored in exponential fits, removing the influence of the initial adjustment of the ion packet to the bunching field and any other short-time dynamical effects. After this time, decay is essentially monoexponential with no significant difference in decay rates seen between bunched and unbunched operation. Unsurprisingly, larger systems such as the tert-butoxide anion show shorter lifetimes despite their reduced path length per unit trapping time, likely due to larger charge-exchange cross-sections with the background gas,³⁸

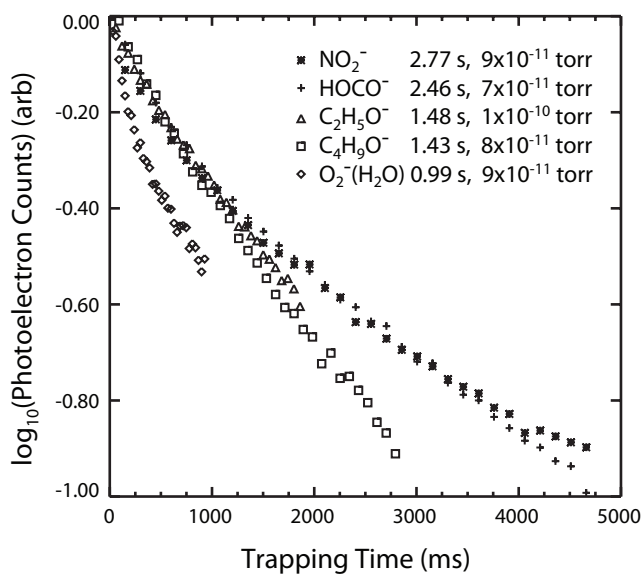


Figure 3.7: Decay times for various species and operational pressures. The vertical axis represents the number of photoelectrons detected in a given trapping interval in logarithmic scale. Fast dynamics due to bunching effects on the overall photodetachment effects are seen for the first few hundred milliseconds, and decay times are measured after the first 500 ms of trapping to reduce the influence of this effect. All data is taken at ~ 7 keV beam energy except $\text{C}_2\text{H}_5\text{O}^-$ which is 4 keV.

though a detailed analysis of these loss mechanisms is beyond the scope of this work. While experiments are typically performed over 1-5 sec trapping time, significant signal remains at the end of the trap cycle allowing experiments over much longer times to be performed if necessary.

3.3.2. Recoil trajectories

A crucial requirement for these translational spectroscopy measurements is the attainment of a low-divergence ion beam with a small cross-section at the interaction region, yielding a small distribution of center-of-mass positions at the neutral particle detector. Optimization of this distribution was performed by observing the distribution of neutral particle impacts on the neutral particle detector for non-dissociative photodetachment of NO_2^- at 388 nm. Representative results of this optimization are shown in Figure 3.8. A strong correlation exists between observed signal rate and neutral position distribution, implying that a narrow, well-collimated beam is only reliably obtained through reduction of the stable trapping phase space. The minimum practical neutral distribution, as projected onto the neutral detector, was ~ 0.9 mm standard deviation with a circular and approximately Gaussian profile. This is significantly smaller than the 3 mm injected beam diameter as determined by the entrance apertures upstream from the trap and approximately the same size as the laser focus. At the lower limit of this optimization, fragment times-of-flight were found to be broadened to later times, implying that trapped ion laboratory energies are not conserved and that inelastic ion-ion scattering may become significant under these conditions. This is consistent with a small stable phase space necessarily leading to a narrow beam, with ions scattered to

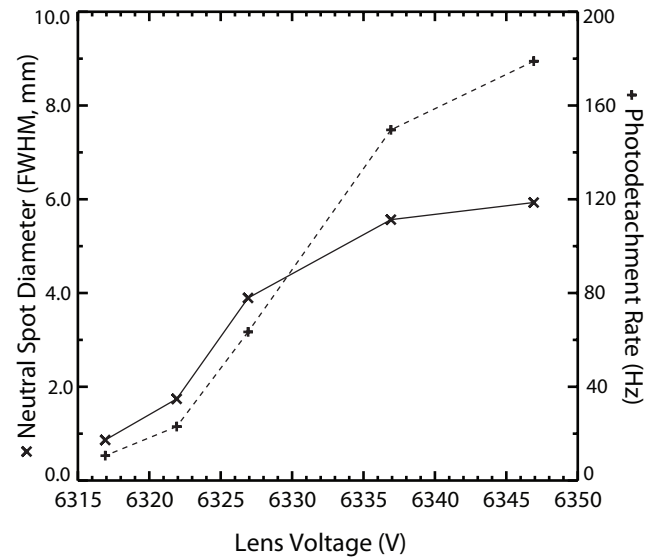


Figure 3.8: Neutral position distribution width (FWHM) (x) and photodetachment rate (+) as a function of trap lens voltage. Here the beam energy and mirror voltages are 6872 eV and 10.490 kV respectively, and ions are not bunched. Total trapping time is 90 ms.

higher energy being lost while ions scattered to lower energy remain in the stable trapping space. No ion heating was observed within the experimental photoelectron resolution in this mode of operation implying these ion-ion collisions do not partition significant amounts of energy into internal degrees of freedom.

3.3.3. Bunching properties

Ion packet dispersion was found to occur on timescales of several tens of milliseconds, requiring the use of bunching even for short trapping times. However, the effect of bunching on the overall kinetic energy spread of the ions must be minimal in order for the three-dimensional neutral particle imaging scheme to be effective. This can be directly determined by observing the time-of-flight of stable neutrals, again from NO_2^- photodetachment, in which the spread of times-of-flight of the neutral particle can be interpreted as an energy spread. In order to assess the effect of the bunching signal amplitude on the beam energy distribution, fragment flight times were recorded at different RF amplitudes, as shown in Figure 3.9. The onset of stable bunching is $\sim 0.6 V_{p-p}$, and the kinetic energy spread remains constant up to 1 V. In this range bunching appears to have little overall effect on the ion velocity profile, and the bunching field acts instead as a time-dependent delay ($\pm \Delta t$) rather than increasing or decreasing the kinetic energies of ions in different parts of the ion packet. This is supported by the fact that no observable change in transverse velocity distributions is seen under low bunching voltages.

A strong dependence on the injection-RF phase was found in the beam energy spread, shown in Figure 3.10 at 1 V_{p-p} amplitude. It is clear that injection off of the optimal phase splits the ion packet into two, each with slightly different average lab

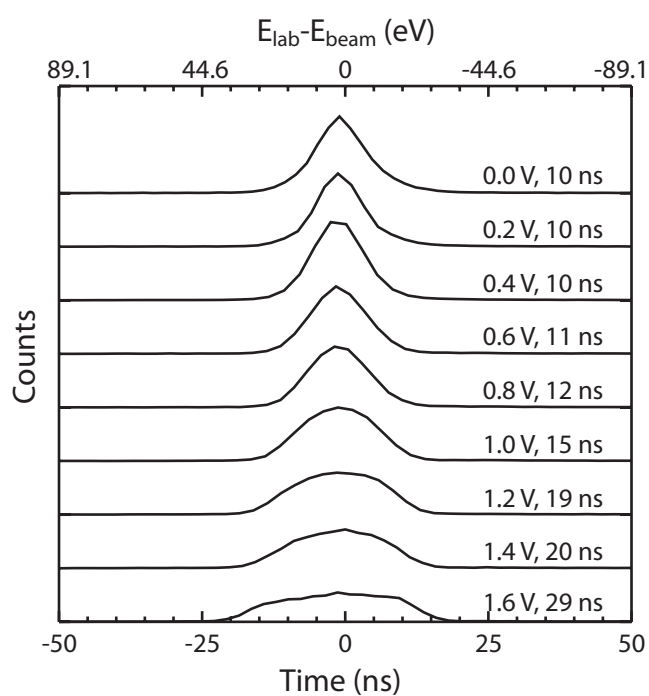


Figure 3.9: Bunch velocity distribution vs. RF amplitude for NO_2^- photodetachment at 388 nm and 6930 eV beam energy. Bunching phases are optimized at $1.0 V_{p-p}$, and the bunching frequency is the second harmonic of the natural ion oscillation frequency of 153.65 kHz. The total trapping time is 90 ms. For each trace, the bunching voltage and peak FWHM are listed.

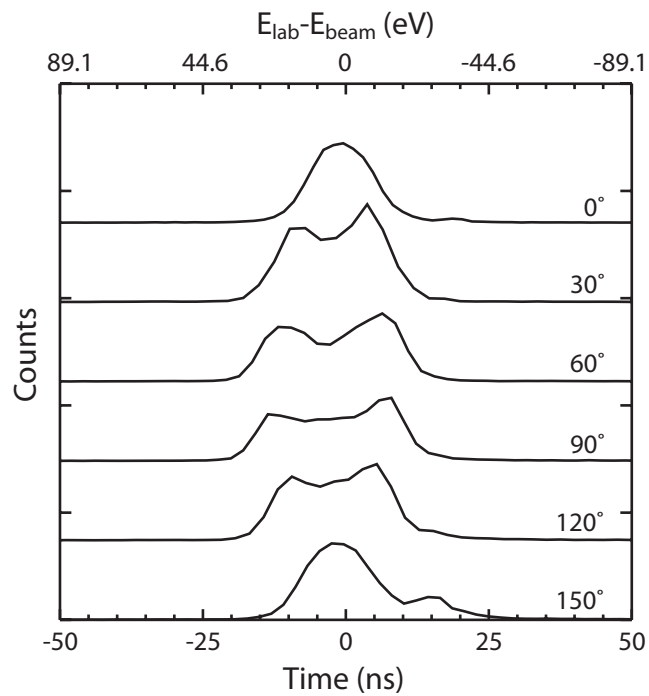


Figure 3.10: Bunch energy distribution vs. RF-injection phase shift for the same conditions as Figure 9. Phases given are with respect to the optimal injection phase. In this case the bunching amplitude is fixed at $1 V_{p-p}$.

frame energies. This effect is less apparent at $0.6 V_{p-p}$ amplitude. This effect implies that the “gentleness” the bunching effect only holds when ions are injected near the correct phase, allowing the bunching field to serve only to compress and maintain bunch width throughout the trapping cycle.

3.3.4. Cooling

An unexpected result that has generally been found with this instrument is that ions in the trap are almost entirely cold throughout the trapping cycle. This is likely due to the ability to generate colder ions in the strong 10 Hz supersonic expansion than the weaker 1 kHz expansion used in previous single-shot experiments in this laboratory.¹⁹ It is also difficult to observe cooling on timeframes shorter than a few milliseconds, due to the 1 kHz laser repetition rate and the fact that ions are trapped approximately 800 μ s prior to the first laser pulse, leading to cooling on these timescales to be missed. However, it has been possible to alter the ion source conditions to form internally excited anions and observe long-time cooling. One example is given in Figure 3.11 for generation of the HOCO radical anion in “hot” source conditions. A clear evolution of the spectrum from early to late trapping times can be seen, as peaks corresponding to the OCO bending vibration of HOCO gradually sharpen towards the end of the trapping period. Though hot anions have thus far proven difficult to generate in the 10 Hz source, it is expected that larger systems and clusters will more readily be generated with measurable amounts of internal energy, allowing radiative cooling dynamics to be observed on long timescales.

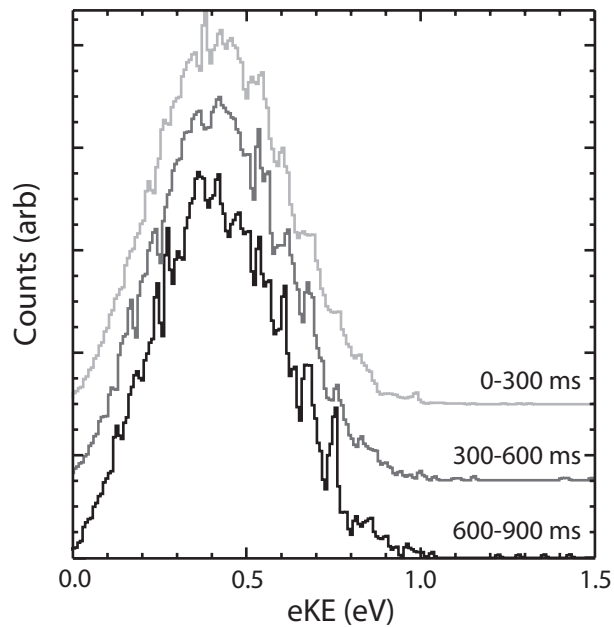


Figure 3.11: An example of cooling in HOCO⁻ anions. All data is from a single data file and each spectrum is composed of events falling within the specified trapping time window. Significant sharpening of spectral features is apparent at later times.

3.3.5. Multimass Experiments

An additional benefit of operating the PPC spectrometer with the ion trap is the ability to collect photoelectron spectra of several species of differing mass simultaneously, particularly when bunching is not enabled. Since all ions traveling within the trap cavity when the entrance mirror closes will be trapped, the coincidence detection scheme allows for electrons from all species to be recorded simultaneously and later separated by mass. This is accomplished by gating, in post-experimental analysis, on electrons in coincidence with specific range of neutral particle time-of-flight corresponding to a given species. This “high-throughput photoelectron spectroscopy” mode has led, for example, to the extraction of $\text{NO}^-(\text{CD}_4)$ and $\text{NO}^-(\text{H}_2\text{O})$ spectra³⁹ from an experiment performed on the DOCOCO^- anion. An example of this extraction is outlined in Figure 12, with photoelectron images and spectra extracted from peaks in the fragment TOF spectrum corresponding to the vinoxide ($\text{C}_2\text{H}_3\text{O}^-$) anion⁴⁰ and NO_2^- , both of which are trapped simultaneously. No detectable crosstalk between the spectra of the two species is seen, allowing photoelectron spectra of multiple species to be collected in a survey experiment.

3.4. Conclusions

The cryo-PPC spectrometer has proven to generate better-resolved data at higher acquisition rates than the single-shot instrument with only a nominal increase in difficulty of operation. In addition, new opportunities are now available for extension of the PPC technique to study systems that were not previously possible due to the ability to couple

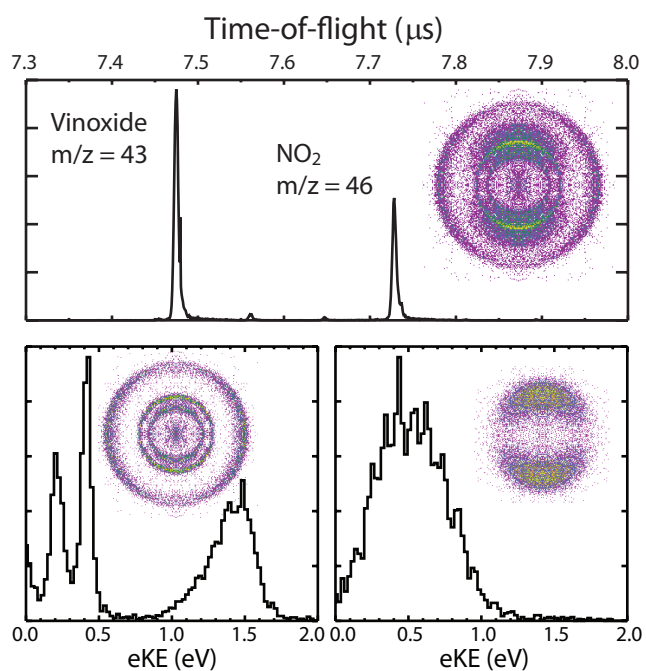


Figure 3.12: An example of multimass operation. The top panel depicts the times-of-flight of the neutral fragments following photodetachment, with the photoelectron image recorded at a photon energy of 3.20 eV for electrons coincident with any neutral particle inset. The bottom left panel is the electron kinetic energy spectrum extracted by enforcing coincidence with only neutrals of $m/z = 43$, ($\text{C}_2\text{H}_3\text{O}^-$) with the resulting photoelectron image inset. The bottom right panel shows the same results for $m/z = 46$ (NO_2^-). All images are quadrant-symmetrized for clarity.

low-repetition-rate sources, such as laser ablation or electrospray, to the kHz rates required for coincidence experiments. New opportunities also exist for studying vibrationally or isomerically prepared systems by laser excitation in the ion source, allowing for much greater control over the conditions and identities of species studied.

Acknowledgements

The text of this Chapter is adapted from the following publication, of which the dissertation author is the primary author and the dissertation advisor is the corresponding author:

Johnson, Christopher J., Shen, Ben B., Poad, Berwyck L. J., and Continetti, R. E. *Rev. Sci. Instrum.*, in press (2011).

References

- (1) Benner, W. H. *Anal. Chem.* **1997**, *69*, 4162-4168.
- (2) Dahan, M.; Fishman, R.; Heber, O.; Rappaport, M.; Altstein, N.; Zajfman, D.; van der Zande, W. J. *Rev. Sci. Instrum.* **1998**, *69*, 76.
- (3) Toker, Y.; Aviv, O.; Erritt, M.; Rappaport, M. L.; Heber, O.; Schwalm, D.; Zajfman, D. *Phys. Rev. A* **2007**, *76*, 53201.
- (4) Knoll, L.; Bhushan, K. G.; Altstein, N.; Zajfman, D.; Heber, O.; Rappaport, M. L. *Phys. Rev. A* **1999**, *60*, 1710.
- (5) Reinhed, P.; Orbán, A.; Werner, J.; Rosén, S.; Thomas, R. D.; Kashperka, I.; Johansson, H. A. B.; Misra, D.; Brännholm, L.; Björkhage, M.; Cederquist, H.; Schmidt, H. T. *Phys. Rev. Lett.* **2009**, *103*, 213002.
- (6) Aviv, O.; Toker, Y.; Errit, M.; Bhushan, K. G.; Pedersen, H. B.; Rappaport, M. L.; Heber, O.; Schwalm, D.; Zajfman, D. *Rev. Sci. Instrum.* **2008**, *79*, 83110.
- (7) Pedersen, H.; Altevogt, S.; Jordon-Thaden, B.; Heber, O.; Lammich, L.; Rappaport, M.; Schwalm, D.; Ullrich, J.; Zajfman, D.; Treusch, R.; Guerassimova, N.; Martins, M.; Wolf, A. *Phys. Rev. A* **2009**, *80*, 012707.
- (8) Bhushan, K. G.; Gadkari, S. C.; Yakhmi, J. V.; Sahni, V. C. *Rev. Sci. Instrum.* **2007**, *78*, 83302.
- (9) Greenwood, J. B.; Kelly, O.; Calvert, C. R.; Duffy, M. J.; King, R. B.; Belshaw, L.; Graham, L.; Alexander, J. D.; Williams, I. D.; Bryan, W. A.; Turcu, I. C. E.; Cacho, C. M.; Springate, E. *Rev. Sci. Instrum.* **2011**, *82*, 43103.
- (10) Zajfman, D.; Rudich, Y.; Sagi, I.; Strasser, D.; Savin, D. W.; Goldberg, S.; Rappaport, M.; Heber, O. *Int. J. Mass Spectrom. Ion Proc.* **2003**, *229*, 55.
- (11) Andersen, L. H.; Heber, O.; Zajfman, D. *J. Phys. B-At. Mol. Opt.* **2004**, *37*, R57.
- (12) Lange, M.; Froese, M.; Menk, S.; Varju, J.; Bastert, R.; Blaum, K.; Lopez-Urrutia, J. R. C.; Fellenberger, F.; Grieser, M.; Hahn, R. von; Heber, O.; Kuehnel, K.-U.; Laux, F.; Orlov, D. A.; Rappaport, M. L.; Repnow, R.; Schroeter, C. D.; Schwalm, D.; Shornikov, A.; Sieber, T.; Toker, Y.; Ullrich, J.; Wolf, A.; Zajfman, D. *Rev. Sci. Instrum.* **2010**, *81*, 55105.
- (13) Heber, O.; Witte, P. D.; Diner, A.; Bhushan, K. G.; Strasser, D.; Toker, Y.; Rappaport, M. L.; Ben-Itzhak, I.; Altstein, N.; Schwalm, D.; Wolf, A.; Zajfman, D. *Rev. Sci. Instrum.* **2005**, *76*, 13104.

- (14) Johnson, C. J.; Continetti, R. E. *J. Phys. Chem. Lett.* **2010**, *1*, 1895.
- (15) Johnson, C. J.; Poad, B. L. J.; Shen, B. B.; Continetti, R. E. *J. Chem. Phys.* **2011**, *134*, 117106.
- (16) Smalley, R. E.; Wharton, L.; Levy, D. H. *Accounts Chem. Res.* **1977**, *10*, 139.
- (17) Lu, Z.; Continetti, R. E. *J. Phys. Chem. A* **2004**, *108*, 9962.
- (18) Wang, X. B.; Woo, H. K.; Wang, L. S.; Minofar, B.; Jungwirth, P. *J. Phys. Chem. A* **2006**, *110*, 5047.
- (19) Lu, Z.; Hu, Q.; Oakman, J. E.; Continetti, R. E. *J. Chem. Phys.* **2007**, *126*, 194305.
- (20) Sanz, M. E.; McCarthy, M. C.; Thaddeus, P. *J. Chem. Phys.* **2005**, *122*, 194319.
- (21) Okumura, M.; Yeh, L. I.; Myers, J. D.; Lee, Y. T. *J. Phys. Chem.* **1990**, *94*, 3416.
- (22) Bailey, C. G.; Kim, J.; Dessent, C. E. H.; Johnson, M. A. *Chem. Phys. Lett.* **1997**, *269*, 122.
- (23) Nielsen, S. B.; Ayotte, P.; Kelley, J. A.; Johnson, M. A. *J. Chem. Phys.* **1999**, *111*, 9593.
- (24) Callegari, C.; Lehmann, K. K.; Schmied, R.; Scoles, G. *J. Chem. Phys.* **2001**, *115*, 10090.
- (25) Kuepper, J.; Merritt, J. M. *Int. Rev. Phys. Chem.* **2007**, *26*, 249.
- (26) Makarov, G. N. *Phys. Usp.* **2004**, *47*, 217.
- (27) Toennies, J. P.; Vilesov, A. F. *Annu. Rev. Phys. Chem.* **1998**, *49*, 1.
- (28) Gerlich, D.; Horning, S. *Chem. Rev.* **1992**, *92*, 1509.
- (29) Wang, X. B.; Woo, H. K.; Wang, L. S. *J. Chem. Phys.* **2005**, *123*, 51106.
- (30) Wang, X.-B.; Wang, L.-S. *Rev. Sci. Instrum.* **2008**, *79*, 73108.
- (31) Kamrath, M. Z.; Relph, R. A.; Guasco, T. L.; Leavitt, C. M.; Johnson, M. A. *Int. J. Mass Spectrom.* **2010**, *300*, 91.
- (32) Continetti, R. E. *Annu. Rev. Phys. Chem.* **2001**, *52*, 165.

- (33) Hanold, K. A.; Luong, A. K.; Clements, T. G.; Continetti, R. E. *Rev. Sci. Instrum.* **1999**, *70*, 2268.
- (34) Pedersen, H. B.; Strasser, D.; Amarant, B.; Heber, O.; Rappaport, M. L.; Zajfman, D. *Phys. Rev. A* **2002**, *65*, 42704.
- (35) Eppink, A.; Parker, D. H. *Rev. Sci. Instrum.* **1997**, *68*, 3477.
- (36) Parsons, B. F.; Sheehan, S. M.; Kautzman, K. E.; Yen, T. A.; Neumark, D. M. *J. Chem. Phys.* **2006**, *125*, 244301.
- (37) Martin, C.; Jelinsky, P.; Lampton, M.; Malina, R. F.; Anger, H. O. *Rev. Sci. Instrum.* **1981**, *52*, 1067.
- (38) Pedersen, H. B.; Strasser, D.; Heber, O.; Rappaport, M. L.; Zajfman, D. *Phys. Rev. A* **2002**, *65*, 42703.
- (39) Poad, B. L. J.; Johnson, C. J.; Continetti, R. E. *Faraday Discuss.* **2011**, *150*, 481.
- (40) Bowen, M. S.; Continetti, R. E. *J. Phys. Chem. A* **2004**, *108*, 7827.

Chapter 4. Dissociative Photodetachment Studies of Cooled HOCO^- Anions Revealing Dissociation Below the Barrier to $\text{H} + \text{CO}_2$

4.1. Introduction

Considerable experimental and theoretical effort has focused on the hydroxyl formyl (HOCO) radical owing to its importance as a combustion reaction intermediate, particularly in the reaction of $\text{OH} + \text{CO} \rightarrow \text{H} + \text{CO}_2$.¹ Important recent contributions have been summarized elsewhere and will only briefly be outlined here. Kinetics studies have found that the thermal behavior of the rate coefficient for formation of $\text{H} + \text{CO}_2$ from $\text{OH} + \text{CO}$ is distinctly non-Arrhenius² and sensitive to vibrational excitation of the OH reactant,³ and several trans-HOCO vibrational modes have been characterized by direct absorption and matrix isolation techniques.⁴⁻⁷ Theoretical efforts have focused on the construction of an accurate potential energy surface (PES), one of which is given in Figure 7.1, for the HOCO intermediate and characterization of important stationary states⁸⁻¹¹ to provide a basis for RRKM,^{12,13} quasiclassical^{1,9,14} and quantum dynamical¹⁵⁻¹⁹ studies of the reaction pathways on this surface as well as reactions of the HOCO radical with other species.²⁰ However, direct experimental information about dynamics on the HOCO intermediate PES, particularly behavior in the well and near the barrier to the exit channel, is scarce due to difficulties in preparing this reactive intermediate.

In order to study directly this region of the PES, Clements *et al.* used photoelectron-photofragment coincidence (PPC) measurements of the dissociative photodetachment (DPD) of HOCO^- at 258 nm (4.80 eV) combined with *ab initio* calculations to probe the HOCO ground and excited PESs.²¹ These experiments measured the photoelectron kinetic energy (eKE) in coincidence with the center-of-mass translational energy release (E_T) for neutral dissociation, and found dissociation to both OH+CO and H+CO₂ as well as stable HOCO. Lu *et al.* extended these DPD experiments to 386 nm (3.21 eV) to obtain a better understanding of the dynamics occurring on the HOCO ground potential energy surface, and saw evidence for a tunneling mechanism for dissociation to H+CO₂.²² However, these results also confirmed the presence of considerable internal excitation in the parent HOCO^- anions that resulted in uncertainties in the measured energetics and presented an alternate but less likely explanation to the tunneling hypothesis.

4.2. Experimental

A new apparatus has been built, integrating a cryogenically cooled variant of a linear electrostatic ion beam trap (EIBT)²³ into an existing PPC spectrometer.²⁴ By storing ions in a cryogenic environment and carrying out PPC experiments on ions inside the trap, this method provides cold ions from a low-duty-cycle source but maintains the high duty cycle required for coincidence experiments. DPD of cold HOCO^- with 3.20 eV photons has been undertaken using this apparatus to gain a clearer understanding of the dynamics on the HOCO PES by removing the uncertainties in the anion internal energy.

HOCO^- anions were created in a pulsed discharge crossed by a 1 keV electron beam acting upon a pulsed supersonic expansion of a mixture of CH₄, CO, N₂O, and N₂

at 60 psi at 10 Hz. These ions were accelerated to 7 keV, re-referenced to ground in a fast high voltage switch, and mass selected by time of flight. HOCO anions at $m/e = 45$ were selected from the beam by an electrostatic chopper and injected into the EIBT, where they were stored for 990 ms in a cryogenic environment of approximately 20 K. Throughout the entire trapping cycle this packet of ions was bunched and phase-locked to a 387 nm, 1.8 ps laser pulse from the 1 kHz Ti:Sa regenerative amplifier that intersected the ion bunch at the center of the trap. Photodetached electrons were collected in a velocity mapping time- and position-sensitive electron detector and neutral particles recoiled out of the trap onto a multiparticle time- and position-sensitive detector. Data was recorded on an event-by-event basis and stored on a PC for analysis at a later time. Calibration by O_2^- photodetachment and O_4^- DPD showed energy resolution of ~ 0.05 eV FWHM for photoelectrons and ~ 0.1 eV FWHM for neutral particles. No evidence for cooling or heating of anions during the 990 ms timescale of these measurements was seen in any spectrum, suggesting that the anion population is roughly in thermal equilibrium with the surrounding environment.

4.3. Results and Discussion

These new measurements show a considerable cooling effect, providing higher-resolution, less congested spectra and allowing the clear separation of contributions from the three observed processes; photodetachment to stable HOCO and DPD to both OH + CO and H + CO₂. Additionally, as a result of the higher spectral resolution, these results further constrain the mechanism for the poorly understood H+CO₂ exit channel, confirming dissociation of HOCO to H+CO₂ well below any calculated barrier to

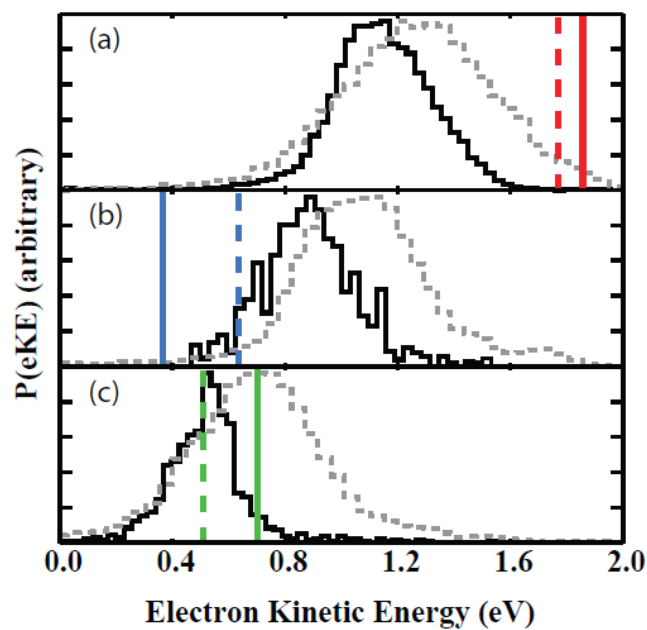


Figure 4.1: Channel-resolved Photoelectron Spectra (a) $\text{HOCO} + e^-$ (b) $\text{H} + \text{CO}_2 + e^-$ (c) $\text{OH} + \text{CO} + e^-$. Solid histograms indicate data from the current study, data from Ref. 22 are shown as dashed histograms. Vertical lines represent the maximum eKE expected from calculations in Refs. 22 and 9 for each channel.

dissociation from the *cis*- or *trans*-HOCO⁸⁻¹¹ well and suggesting an additional possible mechanism for this process.

Figure 4.1 summarizes the channel-resolved photoelectron spectra from “cold” (this work) and “hot” (Lu *et al.*) HOCO⁻ for each product channel with maximum expected electron kinetic energies ($eKE_{\max} = h\nu - \text{adiabatic electron affinity (AEA)} - \text{calculated barrier height}$) in each channel shown for photodetachment of *cis*- (dashed) and *trans*- (solid) HOCO⁻, respectively. The spectra from dissociative events correspond to events with two detected neutral particles and are separated into the two channels by enforcing conservation of momentum. Additionally, due to the large recoil velocity of H atoms in dissociation to H + CO₂, this spectrum is corrected for the detector acceptance function (DAF) which represents the probability of detecting both particles at a given kinetic energy release (KER) with respect to detector geometry and acquisition limitations.²⁵ This allows the recorded spectrum to be deconvolved to extract the true probability of detecting a photoelectron of given kinetic energy, or P(eKE). The HOCO and OH + CO spectra are not affected by the DAF and are not corrected. Events leading to stable HOCO are separated by analyzing only single-particle events with less than 0.5 mm deviation from the ion beam center-of-mass, thereby reducing the contribution of events where only the heavy CO₂ fragment of dissociation to H + CO₂ is detected. Three distinct regions of the photoelectron spectrum are apparent, each corresponding to a specific process on the HOCO potential energy surface. Figure 4.1(a) shows a comparison of P(eKE) obtained from events leading to stable HOCO neutrals. Of primary importance in the cold spectrum is the fact that all observed photoelectrons fall

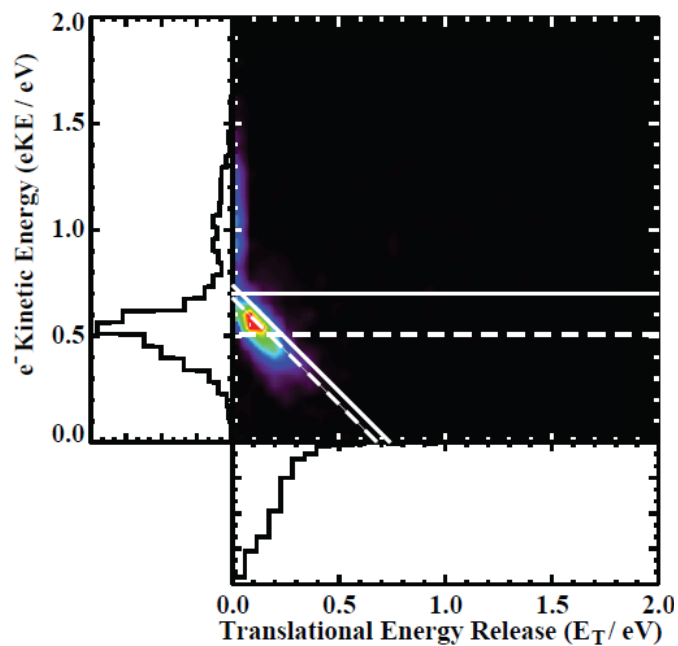


Figure 4.2: Coincidence spectrum for $\text{HOCO}^- + h\nu \rightarrow \text{OH} + \text{CO} + \text{e}^-$. Diagonal lines mark the maximum total energy available for DPD from *cis*- (dashed) and *trans*- (solid) HOCO^- based upon refs. 22 and 9. Horizontal lines represent maximum eKEs for dissociation over barriers on the neutral surface following photodetachment from *cis*- (dashed) and *trans*- (solid) HOCO^- .

below the two limits while the hot spectrum reveals photoelectrons of ~ 0.3 eV higher eKE, providing strong evidence that the ion precursors in the current experiment contain significantly lower internal energy. In the case of dissociation to H+CO₂, shown in Figure 4.1(b), nearly all photoelectrons occur above the maximum predicted eKE for HOCO \rightarrow H + CO₂, indicating that all dissociation to the H+CO₂ limit occurs below the calculated barrier as observed by Lu *et al.* This spectrum too shows an overall shift towards lower eKE of ~ 0.3 eV consistent with the removal of hot band contributions. Finally, Figure 4.1(c) shows the photoelectron spectrum for dissociation to OH+CO which is similarly shifted to lower eKE by ~ 0.4 eV and significantly narrowed as a result of cooling of the precursor HOCO⁻.

More detailed dynamical information can be extracted from the coincidence spectra for the H+CO₂ and OH+CO channels. Figure 4.2 shows the correlation spectrum for dissociation to OH+CO fragments, with a pair of diagonal lines representing the predicted total energy release ($E_{\text{TOT}} = \text{eKE} + \text{KER}$) for *cis*- and *trans*-HOCO⁻ isomers.²² As in the P(eKE) spectra, these results also fall below the predicted E_{TOT} as would be expected of cooled ions. This spectrum is dominated by a narrow diagonal feature with FWHM of less than 0.1 eV. No vibrational excitation in either the OH or CO products is observed, consistent with photodetachment to a directly repulsive part of the PES.

Figure 4.3 shows the DAF-corrected coincidence spectrum for dissociation to H+CO₂. The diagonal lines in this spectrum again represent the predicted maximum E_{TOT} for each anion isomer, and again nearly all data falls below these limits. In this channel the diagonal band is quite broad, > 0.5 eV, indicating a high level of internal excitation in

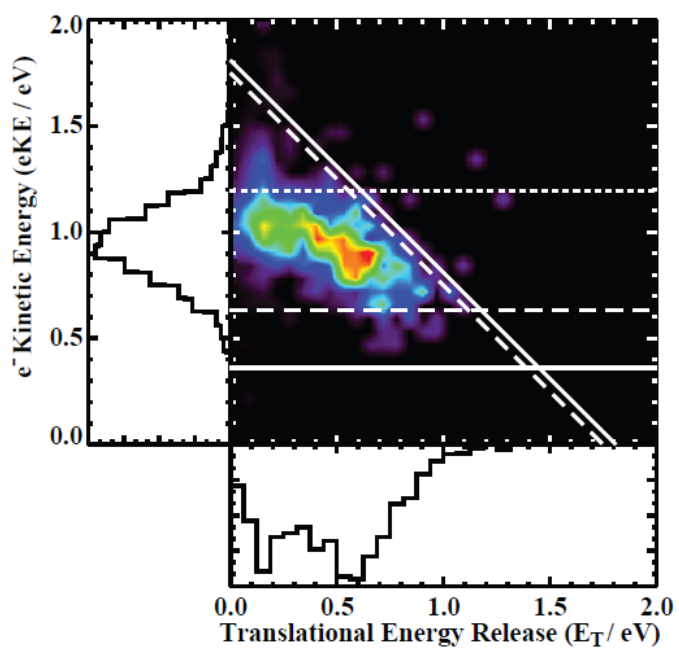


Figure 4.3: Coincidence spectrum for $\text{HOCO}^- + h\nu \rightarrow \text{H} + \text{CO}_2 + \text{e}^-$. Diagonal lines mark the maximum total energy available for DPD from *cis*- (dashed) and *trans*- (solid) HOCO^- based upon refs. 22 and 9. Lower horizontal lines represent maximum eKEs for dissociation over barriers on the neutral surface following photodetachment from *cis*- (dashed) and *trans*- (solid) HOCO^- . The dashed horizontal line marks the maximum eKE allowing for isomerization to the C_{2v} HCO_2 structure.

the CO₂ products. All dissociation is seen to occur above the eKE limits for both isomers, however there appears to be a break in the diagonal band in the range of 1.1 – 1.2 eV which results in a horizontal feature towards low KER. It is interesting to note that this feature nearly matches the maximum eKE expected for detachment from *trans*-HOCO⁻ to the C_{2v} HCO₂ isomer on the neutral surface.⁹ This suggests the possibility that detachment of HOCO⁻ to HOCO is followed by isomerization to HCO₂ prior to dissociation to H+CO₂, an alternative to direct tunneling through the dissociation barrier from the *cis*-HOCO isomer which has been proposed but considered unlikely.^{1,10} The barrier to isomerization from *trans*-HOCO has been calculated to be much higher than the *cis*-HOCO barrier to H + CO₂, therefore this process would also require a tunneling mechanism given the calculated energetics, though H-atom migration is not unprecedented in systems of this size such as H₂CO.^{26,27}

Further information can be drawn from direct comparison of the new data to the previous hot data. In the case of photoelectron spectra, shifts to lower energy of >0.3 eV are seen in all channels. This shift to lower energy is likely due not only to a reduction in internal energy of the anions, but also to the corresponding reduction in the extent of the Franck-Condon region sampled on the neutral potential energy surface resulting from the vibrationally cold anions and the resulting decrease in overlap of the anion and the neutral well. More strikingly, the eKE and coincidence spectra for the OH+CO channel show huge differences, with dissociation occurring nearly entirely above the energetic limit in the hot data but nearly entirely below but near the limit for the cold data. The fact that there is relatively little signal in the hot spectrum that corresponds to the signal in the cold spectrum implies that this process was dominated by dissociation from

vibrationally excited anions, an implication that is further strengthened by the fact that this channel also shows the largest shift to lower eKE of the three processes. Surprisingly, however, the $\text{H}+\text{CO}_2+\text{e}^-$ coincidence spectrum shows only the removal of a higher energy feature found in the hot data, with the lower energy feature virtually unchanged. The higher energy feature was previously assigned to hot bands while the lower energy structure was proposed to result from tunneling through the barrier to $\text{H} + \text{CO}_2$ from cold anions, an assignment supported by this finding. This suggests that, in the Franck-Condon region determined by the cold anions, the neutral PES couples strongly to dissociation to $\text{H}+\text{CO}_2$ despite the apparent presence of high energetic barriers, but only weakly to dissociation to $\text{OH} + \text{CO}$. As the Franck-Condon region grows, however, the coupling to $\text{H} + \text{CO}_2$ apparently changes little while the coupling to $\text{OH} + \text{CO}$ is greatly increased.

By examining the $\text{P}(\text{eKE})$ spectra in more detail, the relative contributions of *cis*- and *trans*-isomers to the observed DPD dynamics can be estimated to aid further analysis. Consideration of the $\text{OH} + \text{CO}$ channel in particular shows that the majority of the photoelectrons detected lie above the calculated barrier from the *cis*-HOCO well but below that for *trans*-HOCO, providing evidence that this process is dominated by dissociation from *trans*-HOCO. However, isomerization from *cis*- to *trans*-HOCO is facile in this part of the PES. In the case of detachment to stable HOCO, all photoelectrons occur below the limits for either isomer, with the observed maximum eKE lying close to the limit for *cis*-HOCO. It is therefore likely that the anion precursors are predominantly the lower-energy *cis*-isomers in this experiment.

An important metric for comparison to theoretical predictions and earlier experiments is the extraction of branching fractions, representing the relative probabilities of the three processes seen. By normalizing to unit area the $P(eKE)$ spectra and scaling each to fit the total detected photoelectron signal, branching fractions may be estimated. In the bottom frame of Figure 4.4 the best fit using the three channel-resolved spectra is shown, giving a $\text{HOCO} : \text{H} + \text{CO}_2 : \text{OH} + \text{CO}$ branching fraction of $0.57 : 0.37 : 0.06$, a significant change from those reported in earlier DPD studies^{21,22} and in stark contrast to calculated ratios which generally show production of the two dissociation channels in approximately equal low yields.¹⁸ This observation provides additional evidence that, in the Franck-Condon region, $\text{H} + \text{CO}_2$ is the dominant dissociation pathway. Energy-resolved branching fractions are plotted in the top frame of Figure 4.4, showing three clear energetic regions dominated by a single process, as well as transitions between each process. Unsurprisingly, in the lowest energy region on the PES the sole process seen is photodetachment to stable HOCO. However it is interesting to note that while the next highest region leads almost exclusively to $\text{H} + \text{CO}_2$, the highest region leads almost exclusively to $\text{OH} + \text{CO}$ even though both channels are energetically allowed. In fact, dissociation to $\text{H} + \text{CO}_2$ essentially ceases as soon as calculations predict that it becomes energetically allowed over the top of the barrier from *cis*-HOCO to $\text{H} + \text{CO}_2$. The transitions between these three distinct regions may also hold important clues about the interplay between these processes. Between the $\text{OH} + \text{CO}$ channel and the $\text{H} + \text{CO}_2$ channel there is a ~ 0.1 eV wide area that leads to roughly equal amounts of $\text{OH} + \text{CO}$ and $\text{H} + \text{CO}_2$, suggesting that low-energy collisions of OH and CO exploring this part of the PES find an efficient path to $\text{H} + \text{CO}_2$. Furthermore, the fact that

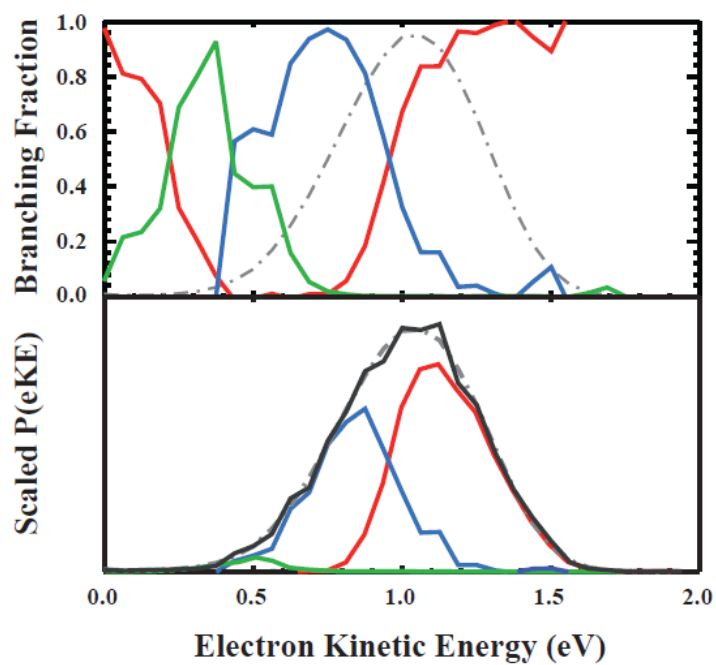


Figure 4.4: (Top) Branching fractions for the three channels as a function of eKE. Also shown is the total photoelectron yield for reference. (Bottom) Fit (solid black line) of scaled channel resolved spectra to the total photoelectron yield. In both figures, red indicates stable HOCO, blue indicates H + CO₂, green indicates OH + CO, and gray dot-dash indicates the total photoelectron spectrum.

dissociation to $H + CO_2$ is available well below the entrance channel indicates that collisional stabilization of the HOCO intermediate may greatly enhance the yield of $H + CO_2$ by cutting off the entrance channel and allowing the intermediate sufficient time to tunnel through the exit barrier. The transition between the $H + CO_2$ and HOCO regions contains, in principle, information about the tunneling probability as a function of energy and could provide an important test for more precise calculations of tunneling through the barrier to $H + CO_2$.

A clearer picture of the discrepancies between kinetic, theoretical, and previous experimental work in this laboratory can now be seen. The large branching ratio to $H + CO_2$ lying entirely below the barrier from either *cis*- or *trans*- isomers requires the existence of a yet-uncharacterized mechanism on this surface which allows the system to bypass large energetic barriers as it dissociates to $H+CO_2$ at low energies. It may be that the portion of the neutral surface explored in this experiment is far enough away from the primary reaction pathway that this mechanism has been previously missed. Tunneling through the *cis*- barrier to $H+CO_2$ is commonly invoked as an explanation for the failure of calculations on *ab initio* surfaces to properly capture the reaction rates, and is supported by statistical calculations which include a correction for tunneling.¹³ However, tunneling from *trans*-HOCO through the HCO_2 barrier appears not to have been studied in detail. The clear break in $P(eKE)$ at the predicted energy for the HCO_2 isomer suggests that this possibility warrants further study. In either case, the present experiments provide unambiguous proof that further refinement of the exit channel region of the HOCO PES is necessary to fully understand this important combustion reaction.

Acknowledgements

The text of this Chapter is adapted from the following publications, of which the dissertation author is the primary author and the dissertation advisor is the corresponding author:

Johnson, Christopher J. and Continetti, Robert E. *J. Phys. Chem. Lett.*, **1**, 1895 (2010).

References

- (1) Kudla, K.; Schatz, G.; Wagner, A. *J. Chem. Phys.* **1991**, *95*, 1635.
- (2) Fulle, D.; Hamann, H.; Hippler, H.; Troe, J. *J. Chem. Phys.* **1996**, *105*, 983.
- (3) Brunning, J.; Derbyshire, D.; Smith, I.; Williams, M. *J. Chem. Soc. Farad. T. 2* **1988**, *84*, 105.
- (4) Jacox, M. *J. Chem. Phys.* **1988**, *88*, 4598.
- (5) Sears, T.; Fawzy, W.; Johnson, P. *J. Chem. Phys.* **1992**, *97*, 3996.
- (6) Petty, J.; Moore, C. *J. Mol. Spectrosc.* **1993**, *161*, 149.
- (7) Forney, D.; Jacox, M.; Thompson, W. *J. Chem. Phys.* **2003**, *119*, 10814.
- (8) Yu, H.; Muckerman, J.; Sears, T. *Chem. Phys. Lett.* **2001**, *349*, 547.
- (9) Lakin, M.; Troya, D.; Schatz, G.; Harding, L. *J. Chem. Phys.* **2003**, *119*, 5848.
- (10) Valero, R.; van Hemert, M.; Kroes, G. *Chem. Phys. Lett.* **2004**, *393*, 236.
- (11) Song, X.; Li, J.; Hou, H.; Wang, B. *J. Chem. Phys.* **2006**, *125*, 094301.
- (12) Golden, D.; Smith, G.; McEwen, A.; Yu, C.; Eiteneer, B.; Frenklach, M.; Vaghjiani, G.; Ravishankara, A.; Tully, F. *J. Phys. Chem. A* **1998**, *102*, 8598.
- (13) Chen, W.; Marcus, R. *J. Chem. Phys.* **2005**, *123*, 094307.
- (14) Bradley, K.; Schatz, G. *J. Chem. Phys.* **1997**, *106*, 8464.
- (15) Yu, H.; Muckerman, J. *J. Chem. Phys.* **2002**, *117*, 11139.
- (16) Valero, R.; McCormack, D.; Kroes, G. *J. Chem. Phys.* **2004**, *120*, 4263.
- (17) Garcia, E.; Saracibar, A.; Zuazo, L.; Lagana, A. *Chem. Phys.* **2007**, *332*, 162.
- (18) Zhang, S.; Medvedev, D. M.; Goldfield, E. M.; Gray, S. K. *J. Chem. Phys.* **2006**, *125*, 164312.
- (19) He, Y.; Goldfield, E.; Gray, S. *J. Chem. Phys.* **2004**, *121*, 823.
- (20) Yu, H.-G.; Poggi, G.; Francisco, J. S.; Muckerman, J. T. *J. Chem. Phys.* **2008**, *129*, 214307.
- (21) Clements, T.; Continetti, R.; Francisco, J. *J. Chem. Phys.* **2002**, *117*, 6478.

- (22) Lu, Z.; Hu, Q.; Oakman, J. E.; Continetti, R. E. *J. Chem. Phys.* **2007**, *126*, 194305.
- (23) Dahan, M.; Fishman, R.; Heber, O.; Rappaport, M.; Altstein, N.; Zajfman, D.; van der Zande, W. *Rev. Sci. Instrum.* **1998**, *69*, 76.
- (24) Hanold, K.; Luong, A.; Clements, T.; Continetti, R. *Rev. Sci. Instrum.* **1999**, *70*, 2268.
- (25) Continetti, R.; Cyr, D.; Osborn, D.; Leahy, D.; Neumark, D. *J. Chem. Phys.* **1993**, *99*, 2616.
- (26) Townsend, D.; Lahankar, S.; Lee, S.; Chambreau, S.; Suits, A.; Zhang, X.; Rheinecker, J.; Harding, L.; Bowman, J. *Science* **2004**, *306*, 1158.
- (27) Goncharov, V.; Lahankar, S. A.; Farnum, J. D.; Bowman, J. M.; Suits, A. G. *J. Phys. Chem. A* **2009**, *113*, 15315.

Chapter 5. New Insight into the Barrier Governing CO₂ Formation from OH + CO

5.1. Introduction

The elementary reaction $\text{OH} + \text{CO} \rightarrow \text{H} + \text{CO}_2$ has been the subject of extensive theoretical and experimental studies yet the detailed dynamics remain poorly understood. This reaction governs CO/CO₂ ratios in hydrocarbon combustion and the upper atmosphere and impacts the HO_x/NO_x/SO_x atmospheric cycles through destruction of OH radicals.¹ It is one of the simplest complex-forming elementary reactions; it is strongly exothermic but features a very stable intermediate, HOCO, and a barrier to activation in the product channel of roughly similar energy to the reactants.²⁻⁴ As a four-atom system, the $\text{OH} + \text{CO} \rightarrow \text{HOCO} \rightarrow \text{H} + \text{CO}_2$ reaction is amenable to a broad range of theoretical treatments,^{2,5-8} and several high-level potential energy surfaces (PESs) exist.⁹⁻¹³ The reaction proceeds through the strongly bound *cis*-HOCO intermediate¹⁴ and shows striking non-Arrhenius behavior.³ The exact height and shape of the barrier to formation of H + CO₂ are critical to the overall kinetics of the reaction. However, beyond limited spectroscopic studies¹⁵⁻²¹ and measurements of excited state dynamics,²² little experimental information exists on the isolated HOCO radical and there is no quantitative agreement on the nature of the barrier and the role that tunneling plays in the overall kinetics of the OH + CO reaction.^{9,23-25}

Photoelectron-Photofragment Coincidence (PPC) spectroscopy²⁶ has been used to directly probe the HOCO PES governing the dynamics of this reaction, resolving three

processes: detachment to internally excited HOCO radicals (stable channel), dissociation to H + CO₂ (exit channel), and dissociation to OH + CO (entrance channel).^{27,28} All dissociation to H + CO₂ was found to occur below the calculated barrier on the neutral PES, consistent with tunneling dissociation. Further analysis revealed dissociation to OH + CO with lifetimes less than 9×10^{-13} s, indicating that when energetically allowed, this process is facile.²⁹ However, these results were complicated by the presence of strong hot bands evident in the photoelectron spectra. Recent incorporation of a cryogenic electrostatic ion beam trap, providing internally cold anions, allowed for unprecedented insight into these dynamics, confirming the occurrence of tunneling through the exit-channel barrier.³⁰ Energy-resolved branching fractions were measured for the three processes, revealing a range of internal energy in which tunneling lifetimes to H + CO₂ are similar to the timescale of the experiment indicative of competition between the stable and exit channels. In the present work these studies are extended to the deuterated DOCO radical and the set of energy-resolved branching fractions are analyzed in detail in the tunneling regime, enabling the development and optimization of a realistic one-dimensional (1D) potential barrier that accurately reproduces the observed tunneling dynamics and independently predicts the observed product internal energy distributions.

5.2. Experimental

Experiments were carried out on a newly constructed PPC spectrometer, similar to one previously reported³¹ but incorporating an electrostatic ion beam trap³² held at cryogenic temperatures (CEIBT) below 30 K in our experiments. Ions were created by crossing a 1 keV electron beam with a 10 Hz coaxial pulsed discharge on a pulsed supersonic expansion of 6% CH₄(CD₄), 6% CO, 13% N₂O, and a balance of N₂. These

ions were accelerated to 7 keV, re-referenced to ground in a potential switch, and mass selected by time of flight. HOCO^- (DOCO^-) anions at m/z 45(46) are selected in a pulsed electrostatic chopper and enter the CEIBT. Once the ions passed the entrance mirror of the CEIBT, it was pulsed to full voltage and the ions trapped for 990 ms. Trapped ions were bunched and synchronized to the 388 nm 2nd harmonic of a 1 kHz, 1.8 ps Ti:Sapphire regenerative amplifier that crossed the ion beam at the center of the trap. Photodetached electrons were extracted out of the laser-ion plane in a velocity-mapping time- and position-sensitive electron detector, and the resulting neutral fragments recoiled through the end of the trap towards a multiparticle time and position sensitive neutral detector. Data from both detectors was recorded in coincidence on an event-by-event basis by a PC-controlled CAMAC system and stored for later analysis. In order to reduce the contribution of false coincidence events, the data acquisition rate was held below 0.1 per laser shot. A full description of the experimental apparatus will be available in an ensuing publication.

5.3. Computational

All potential energy surface calculations were performed using Gaussian 09³³ at the CCSD/aug-cc-pVTZ level of theory and basis set on in-house systems and the Triton Compute Cluster at the San Diego Supercomputer Center. Relaxed potential energy surfaces were zero-point corrected at each geometry using harmonic frequencies for all modes except the one primarily composed of OH stretching. Anharmonic vibrational calculations were performed using CFOUR³⁴ at the CCSD(T) level of theory using the atomic natural orbital basis set of Almlöf and Taylor³⁵ truncated to 4s3p2d1f on C and O atoms and 4s2p1d on the H atom.

5.4. Results

The PPC spectra for $\text{HOCO}^-(\text{DOCO}^-) + h\nu \rightarrow \text{H}(\text{D}) + \text{CO}_2 + e^-$ in Figure 5.1 provide the primary evidence for the presence of tunneling in the exit channel. All dissociation to $\text{H} + \text{CO}_2$ occurs above the maximum electron Kinetic Energy (eKE) limit denoted by horizontal lines and, barring significant errors in the computed surfaces, is therefore due entirely to tunneling. However, an interesting horizontal feature is present in both spectra at the high eKE (low energy on the PES) limit. In dissociative systems PPC spectra generally exhibit diagonal features due to the correlation of energy in the system to energy along the dissociative coordinate. The transition from diagonal to horizontal character at the high eKE limit of both spectra indicates that the tunneling lifetime approaches the time-of-flight (TOF) of the translational spectrometer, 7.8 μs for HOCO and 7.9 μs for DOCO, at these energies. If a metastable HOCO^* neutral travels a significant portion of the TOF before dissociating, the measured translational energy release (E_T) is reduced, and thus a discrete E_T is mapped into a band of apparent E_T extending from the actual value to zero. This horizontal feature appears at lower eKE (higher E_{int}) in the DOCO spectrum as expected due to the reduction in tunneling probability from the larger reduced mass of $\text{D} + \text{CO}_2$. The spectra are also shifted below the maximum total energy release (diagonal lines), indicating that 0.1 to 0.4 eV of the available energy is stored as internal energy in the CO_2 product.

Energy-resolved branching fractions are determined from the relative contribution of each product channel at a given eKE to the overall photoelectron spectrum. Figure 5.2

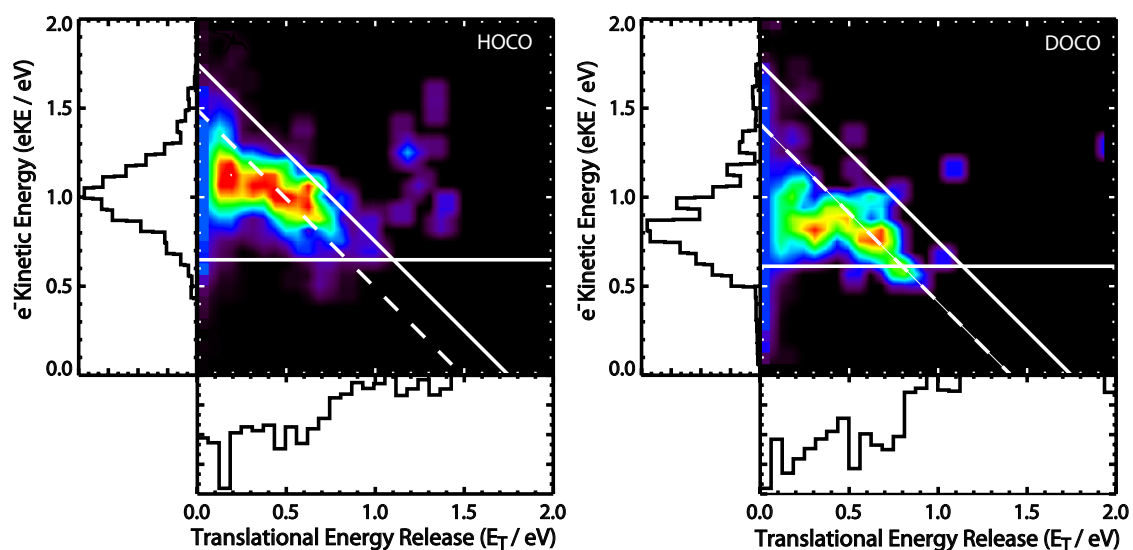


Figure 5.1: PPC spectra for $\text{HOCO}^- (\text{DOCO}^-) \rightarrow \text{H}(\text{D}) + \text{CO}_2 + \text{e}^-$, corrected for the finite acceptance of the neutral particle detector.³⁶ Solid diagonal lines indicate the calculated maximum total kinetic energy available to the system, dashed diagonal lines denote the observed product internal energy peak, and horizontal lines indicate the maximum eKE expected for above-barrier dissociation of *cis*-HOCO(DOCO). The signal above the maximum kinetic energy line is due to a small number of false coincidences and is ignored.

shows the fraction of events resulting in stable HOCO and DOCO as a function of eKE. These fractions are determined from the relative contribution of each product channel at a given energy to the overall spectrum, though only the stable channel is shown here for clarity. Consistent with the PPC spectra, the stable DOCO fraction begins to drop at lower eKE than for HOCO as expected for isotopic substitution. In the region of competition between the stable channel and the exit channel, the stable fraction can be used to compute tunneling probabilities.

5.5. Tunneling Analysis

Tunneling probabilities can not be reliably extracted where the branching fractions are effectively either 0 or 1, as the linear error in the branching fraction causes exponential error in the tunneling probabilities in these cases. A 1D barrier to dissociation can be optimized to fit the selected tunneling probabilities using a quasi-1D model, simplified from one outlined by Miller.³⁷ In this model nuclear motion is assumed to be separable into dissociative and non-dissociative components and dissociative motion is treated as a two-body 1D system (H-OCO). All non-dissociative internal energy resides entirely in OCO and the partitioning of this energy is controlled by an experimentally-determined linear parameter χ , while only dissociative energy is considered for tunneling through the barrier.

A semiclassical analysis consisting of a classical oscillator with a quantum tunneling probability at the outer turning point is used to invert the stable fraction to energy-resolved transmission coefficients by

$$T(E_{int}) = \left(1 - f(E_{int})^{1/N}\right) \quad (1)$$

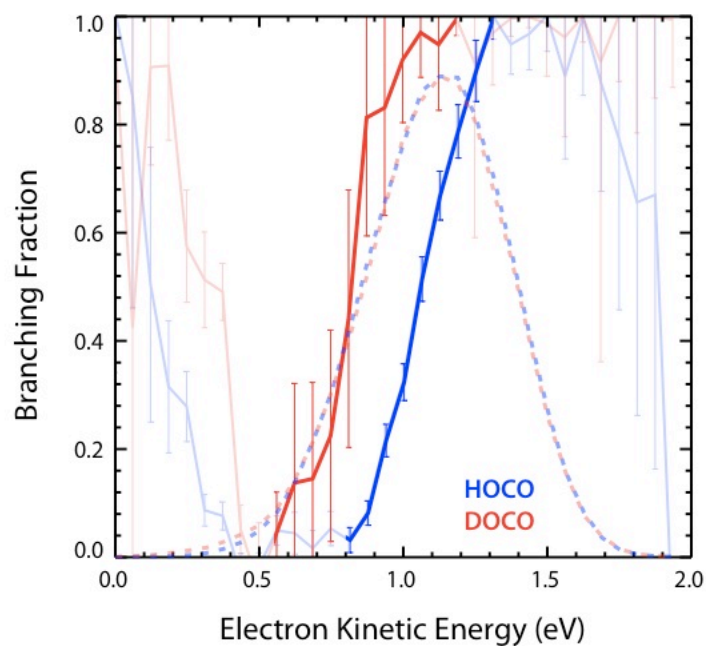


Figure 5.2: Energy resolved stable fractions for DPD of HOCO^- (blue) and DOCO^- (red). Error is estimated by propagating the Poisson error at each eKE through the full analysis procedure. Total photoelectron spectra (dashed lines) are included to indicate areas of poor overall signal-to-noise. Segments of the curves that are shaded represent data that is outside the region with tunneling lifetimes on the order of the experiment.

where $f(E_{int})$ is the measured stable HOCO* fraction at a given energy and N is the number of classical oscillations with frequency f_{osc} that occur during the TOF given by $N = f_{osc}t_{TOF}$.

A parameterized potential energy curve can now be produced and optimized to minimize the difference between the experimental and computed tunneling coefficients at each energy. For an arbitrarily shaped 1-D barrier, the tunneling coefficients may be calculated using the WKB approximation with a parabolic correction to account for inaccuracy as the classical turning points become close,³⁸

$$T(E_{int}) \approx \left[1 + \exp \left\{ -2 \int_{r_1(E_{diss})}^{r_2(E_{diss})} \sqrt{\frac{2\mu}{\hbar^2} (V(r) - E_{diss})} dr \right\} \right]^{-1} \quad (2)$$

with μ as the reduced mass, $V(r)$ as the potential function, r_1 and r_2 as the classical inner and outer turning points, and E_{diss} as the energy in the dissociation coordinate. Due to the separation of dissociative and non-dissociative motion, only energy in the OH bond (E_{diss}) is considered in the WKB integral, while the tunneling coefficients are given in terms of the total internal energy E_{int} determined from the eKE. To account for this partitioning phenomenologically, we approximate the energy along the bond dissociation coordinate by adding a fraction χ of the energy in the other five modes to the energy in the HOCO normal mode dominated by OH stretching, giving

$$E_{diss} = E_{OH(OD)}(v_{max}) + \chi [E_{int} - E_{OH(OD)}(v_{max})] \quad (3)$$

where $E_{OH(OD)}(v_{max})$ is the anharmonic vibrational energy at the highest level of excitation in the OH(OD) stretching mode.

In order to generate a barrier with a realistic shape, an adiabatic potential is generated using a two-state model consisting of a coupled Morse oscillator and repulsive

potential. The use of a Morse oscillator allows some quantities to be fixed at known values, reducing the number of fitting parameters significantly. The potential around the avoided crossing is

$$V_{a,b}(r) = \frac{V_1(r) + V_2(r)}{2} \pm \sqrt{\left(\frac{V_1(r) - V_2(r)}{2}\right)^2 + H_{12}(r)^2} \quad (4a)$$

where we define

$$V_1(r) = D_e [1 - \exp\{-\alpha(r - r_e)\}]^2 \quad (4b)$$

$$V_2(r) = Ar^{-n} + \Delta V_{BD} \quad (4c)$$

$$H_{12}(r) = H_{12}^0 \exp\{-a|V_1(r) - V_2(r)|\} \quad (4d)$$

Here $V_1(r)$ is the Morse potential with well depth D_e , curvature constant α , and equilibrium bond length r_e , while the repulsive potential $V_2(r)$ is determined by the amplitude, A , and the order n , and a small offset ΔV_{BD} corresponding to the difference in ground state energies between the bound and dissociated states. Finally, H_{12}^0 is the coupling energy and a is the damping of the coupling between the two adiabatic surfaces. An implicit assumption of this scheme is that the generated curve is zero-point corrected in all dimensions but the OH stretch.

The preceding model has been used to optimize a barrier by the Nelder and Mead “amoeba” algorithm.³⁹ In the potential function the Morse well depth is set to produce the asymptotic energy expected for a separated H atom and CO₂ in the first electronic excited state $\tilde{A}'(B_2)$ at 5.70 eV,⁴⁰ while the equilibrium bond length is generally agreed to be approximately 0.98 Å among the various PESs. The parameters a and ΔV_{BD} are set to 0.05 (unitless) and 0.07 eV, respectively. However, α , H_{12}^0 , A , and n are allowed to vary, as is the energy partitioning parameter χ . Since the values of E_{diss} depend strongly on the

choice of v_{max} good fits for HOCO and DOCO simultaneously were found only when $v_{OH} = 1$ and $v_{OD} = 2$, consistent with the tunneling in DOCO occurring only at higher internal energy. Anharmonic calculations give fundamental energies of 3457 cm^{-1} for HOCO and 2555 cm^{-1} for DOCO and anharmonicity terms of 97 cm^{-1} and 52 cm^{-1} respectively. The optimized parameters producing the best-fitting barrier are $\alpha = 1.96$, $A = 4.02 \text{ eV}$, $n = 2.27$, $H_{12}^0 = 0.49 \text{ eV}$, and $\chi = 0.19$.

The experimentally derived potential is composed of a Morse oscillator coupled to a dissociative potential, and is plotted in Figure 5.3 along with a fully relaxed, zero-point corrected scan of the energy along the OH bond length using the CCSD/aug-cc-pVTZ level of theory.

5.6. Discussion

Comparison of the experimental barrier with the computed minimum-energy barrier shows good agreement for the bound part of the surface and distinct differences for the dissociative part. The curvature parameter of the Morse potential gives an OH stretching frequency of 3486 cm^{-1} , in good agreement with the computed value.³¹ The zero-point corrected barrier height is found to be 1.13 eV at 1.44 \AA , displaced to larger r_{OH} by 0.09 \AA and 0.02 eV higher than the minimum-energy barrier but significantly wider. Among the available full PESs,¹⁰⁻¹³ ZPE-corrected saddle points range from 0.97 to 1.28 eV , consistent with the model barrier.

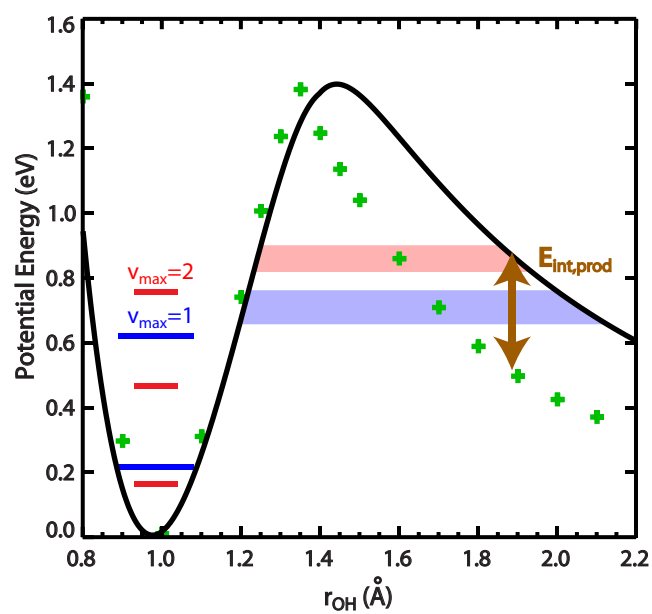


Figure 5.3: Model PES for *cis*-HOCO \rightarrow H + CO₂, shown in black, and calculated minimum-energy barrier (green crosses). Also included are the relevant OH (blue) and OD (red) vibrational levels and the range of E_{diss} where long-lifetime tunneling is observed for each isotopologue. An example of expected product internal energy, given by $E_{\text{int,prod}}$, is also shown.

The computed minimum energy barrier is not expected to properly reproduce the tunneling dynamics in the HOCO system. Calculations show significant geometrical changes as the system crosses the barrier, particularly in the OCO angle, which changes by nearly 40° over a 0.05 \AA change in r_{OH} . Thus, relaxed scans along r_{OH} reflect these geometrical changes and represent a lower limit, at each bond length, to the barrier through which tunneling occurs. Since H atom tunneling occurs rapidly compared to the motion of OCO, tunneling must occur at essentially constant CO_2 geometry, and therefore is nearly perpendicular to the minimum-energy pathway in the relevant (r_{OH} , \angle_{OCO}) plane of the surface, exemplified in Figure 5.4.

Using the model barrier the internal energy in the CO_2 products resulting from tunneling can be estimated and compared to the experimental values. Significant vibrational excitation in the CO_2 product is expected due to the difference between the tunneling geometry and the equilibrium CO_2 geometry. Thus the energy at the outer limit of the tunneling path gives an estimate of the internal energy in the CO_2 fragment. The difference between the calculated and experimentally derived barriers in the repulsive region is approximately 0.2 to 0.3 eV, arising from the un-relaxed nature of the OCO fragment during tunneling. Comparison of this expectation with the average internal energy from the coincidence spectra of 0.2 eV for HOCO and 0.3 eV for DOCO shows close agreement. A second independent confirmation involves the energy partitioning factor χ relating total internal energy to internal energy in the bond-breaking coordinate. While the quasi-1D model implicitly requires vibrational adiabaticity, this is not enforced in the extraction procedure. This implies that the CO_2 fragment internal energy once dissociation is complete should equal the non-dissociative energy component, $E_{\text{int}} - E_{\text{diss}}$,

which also ranges from 0.1 to 0.3 eV. The agreement of both of these checks without inclusion of experimental information regarding product internal energy provides strong evidence that the model captures most of the important dynamical aspects of the system. The slight discrepancy in the internal energy distribution ranges from the model indicate that vibrational adiabaticity does not strictly hold, with partitioning of energy between kinetic and internal degrees of freedom as the OCO equilibrium geometry relaxes suddenly from bent to linear in the exit channel.

While the model potential is able to reproduce the experimental tunneling rates extremely well, tunneling lifetimes become too short relative to the time-scale of the measurement to determine the fraction of stable radicals near the top of the barrier. Given the 1D approximation used here, the possibility that the actual barrier and tunneling rates deviate from the model at the top of the barrier cannot be ruled out. As the tunneling distance approaches zero the tunneling pathway must approach the minimum energy pathway implying that the extracted barrier shape should approach the shape of the minimum-energy barrier at the saddle-point. The failure to do so could indicate inapplicability of the barrier at these energies, dynamics beyond those explicitly considered in the model, or that the minimum-energy barrier fails to capture the tunneling dynamics at any energy. However, the veracity of the model barrier is supported by the observation in Figure 5.4 that the tunneling pathway and minimum-energy pathway intersect near the saddle point, implying little geometric change as a function of energy for this plane of the PES.

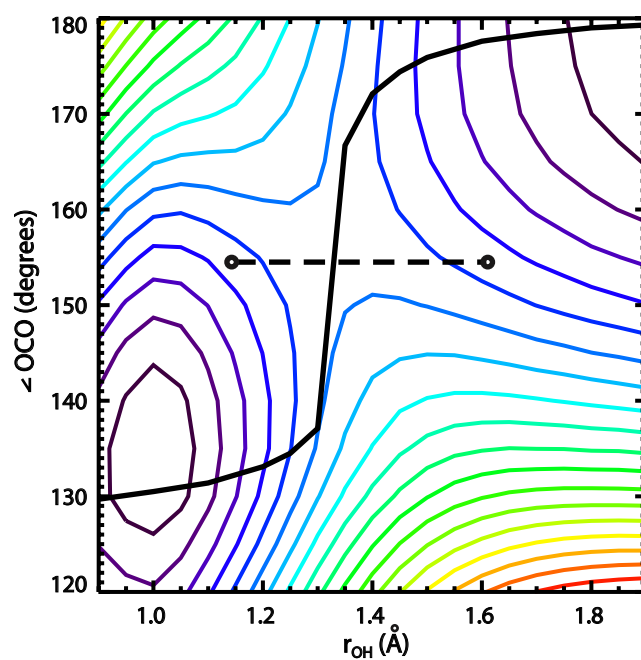


Figure 5.4: An example 2D slice (r_{OH} , \angle_{OCO}) at fixed $r_{OC} = r_{CO} = 1.18 \text{ \AA}$ of the HOCO PES (non-ZP corrected). The computed minimum energy path (solid) is overlaid and the path of highest tunneling probability (dashed) is shown for an example value of E_{diss} .

Tunneling lifetimes are computed using the model barrier over its full energy range, shown in Figure 5.5 as a function of energy in the dissociation coordinate. It can be seen that in the particularly relevant region near the entrance channel energy of 1.2 eV, the tunneling lifetimes are predicted to be less than 1 psec, similar to the measured lifetime of the $\text{HOCO} \rightarrow \text{OH} + \text{CO}$ process,²⁹ implying that slight collisional stabilization or temporarily bound complexes could lead to non-negligible dissociation through this barrier. Even above the barrier, where dissociation is expected to be facile, frustration due to curvature of the reaction path may also cause tunneling *above* and away from the saddle point energy to become competitive,⁴¹ Tunneling rates for the minimum energy barrier, also in Figure 4, give a lower limit to the tunneling lifetimes and thus can be used in concert with the model lifetimes to constrain the rates of processes occurring in this energy regime of the PES.

The data presented here can be of direct use in more sophisticated treatments of the tunneling process⁴¹⁻⁴³ particularly with regard to the role of vibrational energy distribution in the HOCO^* intermediate which is treated crudely in this model. Additionally, the effect of isomerization to *trans*- HOCO acting as a sink for *cis*- HOCO^* that would otherwise tunnel is not considered. If this process occurs, the actual tunneling rates could be significantly higher than those predicted by the model barrier. The lowest-energy transition state between *cis*- and *trans*- HOCO is reached by out-of-plane torsional motion of the H atom. Excitation of the torsional mode of HOCO is not expected in photodetachment due to the planarity of both the anion and neutral and inefficient vibrational redistribution due to the A'' symmetry of the torsional mode, so this transition

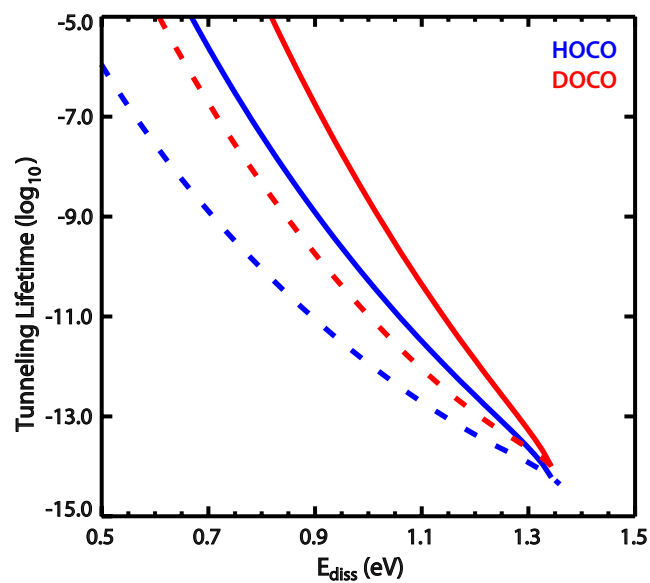


Figure 5.5: Prediction of tunneling lifetimes as a function of energy in the OH (red) and OD (blue) stretch (solid lines) compared to those taken from the theoretically predicted minimum energy barrier (dashed).

state should be inactive as a mechanism for loss of *cis*-HOCO*. However, a poorly characterized higher energy planar isomerization transition state also exists which could result in a reduction in the actual tunneling yield if it is found to have low enough energy. Work on a more detailed transition-state-theory model of the global kinetics on this surface which can accurately reproduce these dissociative photodetachment results should help to further illuminate the role that tunneling plays in the overall dynamics of this reaction.

Acknowledgements

The text of this Chapter is adapted from the following publication, of which the dissertation author is the primary author and the dissertation advisor is the corresponding author:

Johnson, Christopher J., Poad, Berwyck L. J., Shen, Ben B., and Continetti, Robert E. *J. Chem. Phys.*, **134**, 117106 (2011).

References

- (1) Berry, R.; Lehman, P. *Annu. Rev. Phys. Chem.* **1971**, *22*, 47.
- (2) Smith, I. *Chem. Phys. Lett.* **1977**, *49*, 112.
- (3) Fulle, D.; Hamann, H.; Hippler, H.; Troe, J. *J. Chem. Phys.* **1996**, *105*, 983.
- (4) Francisco, J. S.; Muckerman, J. T.; Yu, H.-G. *Accounts Chem. Res.* **2010**, *43*, 1519.
- (5) Frost, M.; Sharkey, P.; Smith, I. *J. Phys. Chem.* **1993**, *97*, 12254.
- (6) Kudla, K.; Schatz, G.; Wagner, A. *J. Chem. Phys.* **1991**, *95*, 1635.
- (7) Yu, H.; Muckerman, J. *J. Chem. Phys.* **2002**, *117*, 11139.
- (8) He, Y.; Goldfield, E.; Gray, S. *J. Chem. Phys.* **2004**, *121*, 823.
- (9) Aoyagi, M.; Kato, S. *J. Chem. Phys.* **1988**, *88*, 6409.
- (10) Yu, H.; Muckerman, J.; Sears, T. *Chem. Phys. Lett.* **2001**, *349*, 547.
- (11) Lakin, M.; Troya, D.; Schatz, G.; Harding, L. *J. Chem. Phys.* **2003**, *119*, 5848.
- (12) Valero, R.; van Hemert, M.; Kroes, G. *Chem. Phys. Lett.* **2004**, *393*, 236.
- (13) Song, X.; Li, J.; Hou, H.; Wang, B. *J. Chem. Phys.* **2006**, *125*, 094301.
- (14) Alagia, M.; Balucani, N.; Casavecchia, P.; Stranges, D.; Volpi, G. *J. Chem. Phys.* **1993**, *98*, 8341.
- (15) Sears, T.; Fawzy, W.; Johnson, P. *J. Chem. Phys.* **1992**, *97*, 3996.
- (16) Petty, J.; Moore, C. *J. Mol. Spectrosc.* **1993**, *161*, 149.
- (17) Forney, D.; Jacox, M.; Thompson, W. *J. Chem. Phys.* **2003**, *119*, 10814.
- (18) Milligan, D.; Jacox, M. *J. Chem. Phys.* **1971**, *54*, 927.
- (19) Oyama, T.; Funato, W.; Sumiyoshi, Y.; Endo, Y. *J. Chem. Phys.* **2011**, *134*, 174303.
- (20) Petty, J.; Moore, C. *J. Chem. Phys.* **1993**, *99*, 47.
- (21) Jacox, M. *J. Chem. Phys.* **1988**, *88*, 4598.
- (22) Savee, J. D.; Mann, J. E.; Continetti, R. E. *J. Phys. Chem. A* **2010**, *114*, 1485.

- (23) Golden, D.; Smith, G.; McEwen, A.; Yu, C.; Eiteneer, B.; Frenklach, M.; Vaghjiani, G.; Ravishankara, A.; Tully, F. *J. Phys. Chem. A* **1998**, *102*, 8598.
- (24) Medvedev, D.; Gray, S.; Goldfield, E.; Lakin, M.; Troya, D.; Schatz, G. *J. Chem. Phys.* **2004**, *120*, 1231.
- (25) Zhang, S.; Medvedev, D. M.; Goldfield, E. M.; Gray, S. K. *J. Chem. Phys.* **2006**, *125*, 164312.
- (26) Continetti, R. *Int. Rev. Phys. Chem.* **1998**, *17*, 227.
- (27) Clements, T.; Continetti, R.; Francisco, J. *J. Chem. Phys.* **2002**, *117*, 6478.
- (28) Lu, Z.; Hu, Q.; Oakman, J. E.; Continetti, R. E. *J. Chem. Phys.* **2007**, *126*, 194305.
- (29) Lu, Z.; Oakman, J. E.; Hu, Q.; Continetti, R. E. *Mol. Phys.* **2008**, *106*, 595.
- (30) Johnson, C. J.; Continetti, R. E. *J. Phys. Chem. Lett.* **2010**, *1*, 1895.
- (31) Hanold, K.; Luong, A.; Clements, T.; Continetti, R. *Rev. Sci. Instrum.* **1999**, *70*, 2268.
- (32) Dahan, M.; Fishman, R.; Heber, O.; Rappaport, M.; Altstein, N.; Zajfman, D.; van der Zande, W. *Rev. Sci. Instrum.* **1998**, *69*, 76.
- (33) Frisch, M. J.; Trucks, G. W.; Schlegel, H. B.; Scuseria, G. E.; Robb, M. A.; Cheeseman, J. R.; Scalmani, G.; Barone, V.; Mennucci, B.; Petersson, G. A.; Nakatsuji, H.; Caricato, M.; Li, X.; Hratchian, H. P.; Izmaylov, A. F.; Bloino, J.; Zheng, G.; Sonnenberg, J. L.; Hada, M.; Ehara, M.; Toyota, K.; Fukuda, R.; Hasegawa, J.; Ishida, M.; Nakajima, T.; Honda, Y.; Kitao, O.; Nakai, H.; Vreven, T.; Montgomery, J. A., Jr; Peralta, J. E.; Ogliaro, F.; Bearpark, M.; Heyd, J. J.; Brothers, E.; Kudin, K. N.; Staroverov, V. N.; Kobayashi, R.; Normand, J.; Raghavachari, K.; Rendell, A.; Burant, J. C.; Iyengar, S. S.; Tomasi, J.; Cossi, M.; Rega, N.; Millam, N. J.; Klene, M.; Knox, J. E.; Cross, J. B.; Bakken, V.; Adamo, C.; Jaramillo, J.; Gomperts, R.; Stratmann, R. E.; Yazyev, O.; Austin, A. J.; Cammi, R.; Pomelli, C.; Ochterski, J. W.; Martin, R. L.; Morokuma, K.; Zakrzewski, V. G.; Voth, G. A.; Salvador, P.; Dannenberg, J. J.; Dapprich, S.; Daniels, A. D.; Farkas, O.; Foresman, J. B.; Ortiz, J. V.; Cioslowski, J.; Fox, D. *J. Gaussian 09*.
- (34) Stanton, J. F.; Gauss, J.; Harding, M. E.; Szalay, P. G. CFOUR, Coupled-Cluster techniques for Computational Chemistry.
- (35) Almlöf, J.; Taylor, P. *J. Chem. Phys.* **1987**, *86*, 4070.
- (36) Continetti, R.; Cyr, D.; Osborn, D.; Leahy, D.; Neumark, D. *J. Chem. Phys.*

- 1993**, *99*, 2616.
- (37) Miller, W. *Chem. Rev.* **1987**, *87*, 19.
- (38) Forst, W. *Unimolecular Reactions*; Cambridge University Press: Cambridge, UK, 2003.
- (39) Nelder, J.; Mead, R. *Comput. J.* **1965**, *7*, 308.
- (40) Herzberg, G. *Electronic Spectra of Polyatomic Molecules*; D. van Nostrand Company, Inc.: Princeton, 1966.
- (41) Miller, W.; Handy, N.; Adams, J. *J. Chem. Phys.* **1980**, *72*, 99.
- (42) Skodje, R.; Truhlar, D.; Garrett, B. *J. Phys. Chem.* **1981**, *85*, 3019.
- (43) Makri, N.; Miller, W. *J. Chem. Phys.* **1989**, *91*, 4026.

Chapter 6. The Electron Affinities, Well Depths, and Vibrational Spectroscopy of *cis*- and *trans*-HOCO

6.1. Introduction

The reaction $\text{OH} + \text{CO} \rightarrow \text{H} + \text{CO}_2$ and its intermediate species, the HOCO radical, have garnered a significant amount of attention over the last several decades due to its importance in atmospheric¹ and combustion processes,² but significant gaps still exist in the understanding of the detailed mechanism of this reaction. The HOCO radical has proven relatively difficult to isolate, limiting the range of techniques brought to bear upon it and thus it remains poorly characterized. It is believed that the HOCO intermediate can be stabilized by a third body, opening the potential for significant radical chemistry,³ and a more thorough understanding of the isolated radical is necessary to evaluate the role these types of interactions may play in bulk processes. Matrix isolation studies in CO, neon, and argon have identified most of the fundamental frequencies of *cis*-/*trans*-HOCO/DOCO,⁴⁻⁶ and the related normal modes are shown in Figure 6.1, but gas phase experiments have been limited to direct absorption measurements of the OH⁷⁻⁹ and terminal CO¹⁰ stretching modes of *trans*-HOCO. Recent pure rotational spectra of *cis*- and *trans*-HOCO are consistent with *ab initio* structures.¹¹ Electron affinities (EAs) for both isomers have been calculated and found to be in rough

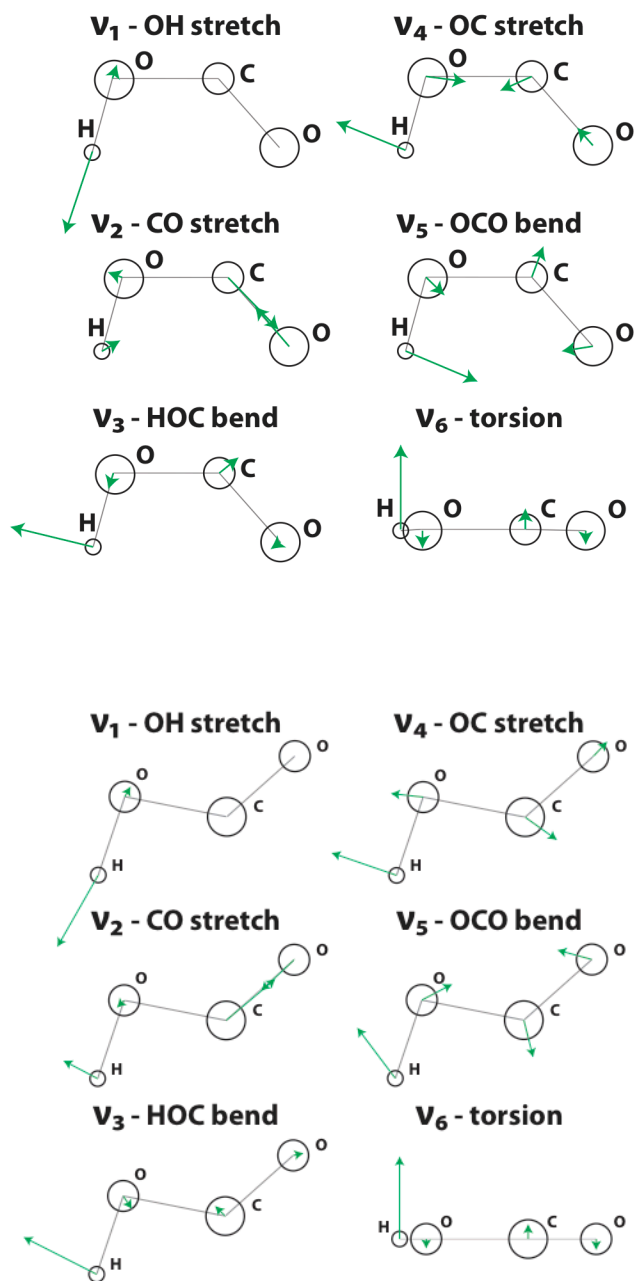


Figure 6.1: Normal modes for *cis*- (top) and *trans*- (bottom) HOCO. The mode displacements are taken from the CCSD(T)/ANO1 harmonic frequency calculations..

agreement with dissociative photodetachment results,^{12,13} though the isomeric composition in those experiments was unknown. Photoelectron spectra near threshold (772 nm) revealed two peaks at low electron kinetic energy that were not conclusively assigned, as a broad background arising from internally excited anions prevented unambiguous resolution of these features.¹⁴ These features were recently suggested to arise from vibrational Feshbach resonances in dipole-bound states, though the potential for pure photodetachment was not ruled out.¹⁵

Here we report a systematic photoelectron imaging study of HOCO and DOCO by detachment of vibrationally cold HOCO⁻ and DOCO⁻ anions. Photoelectron spectra with well-resolved vibrational structure are presented and compared to high-level calculations. Revised electron affinities are presented for both isomers as well as the first gas-phase frequencies of several vibrational modes of *cis*-HOCO and one mode of *trans*-HOCO. Additionally, the well depths for both isomers are calculated, making use of previously reported dissociative photodetachment results.¹⁶

6.2. Results

Figures 6.2 and 6.3 show photoelectron spectra for HOCO⁻ and DOCO⁻ respectively at 660 nm and 775 nm, respectively. Both 660 nm spectra include a phenomenological fit of the experimental ν_3 , ν_4 , and ν_5 frequencies of *cis*-HOCO and the ν_5 frequency of *trans*-HOCO, obtained by setting the vibrational frequencies and generating Gaussian-convolved peaks with variable widths and intensities. Calibration to spin-orbit splitting in O⁻ photodetachment at 775 nm yields an instrumental resolution of 0.014 eV at 0.14 eV, and at 660 nm 0.020 eV at 0.42 eV. Also included are the

Table 6.1: Comparison of experimental and calculated vibrational frequencies for HOCO and DOCO. Gas phase absorption measurements are italicized, all other previous experiments performed in Ar/Ne/CO matrix.

Mode	Description	This Expt.	Prev. Expt.	Harmonic	Anharmonic
<i>cis</i> -HOCO (DOCO)					
v₁	OH stretch		3316 ^a	3667 (2666)	3458 (2555)
v₂	CO stretch		1797 ^a	1852 (1851)	1815 (1814)
v₃	HOC bend	1290	1261 ^a	1313 (1155)	1282 (1121)
v₄	OC stretch	1040 (968)	1088 ^a	1076 (978)	1042 (949)
v₅	OCO bend	605 (565)	620 ^a	602 (543)	596 (535)
v₆	torsion			578 (476)	545 (454)
<i>trans</i> -HOCO (DOCO)					
v₁	OH stretch		3636 ^b (2684 ^c) 3628 ^d (2678 ^d)	3830 (2788)	3641 (2688)
v₂	CO stretch		1853 ^c (1852 ^c) 1848 ^d (1846 ^d)	1895 (1884)	1854 (1845)
v₃	HOC bend	1194 (1065)	1210 ^d (1083 ^d)	1258 (1119)	1217 (1081)
v₄	OC stretch	1048	1050 ^d	1086 (924)	1057 (900)
v₅	OCO bend	629 (605)	615 ^a	621 (594)	614 (588)
v₆	torsion		508 ^d	536 (411)	507 (395)

- a. Reference 4
- b. Reference 7
- c. Reference 9
- d. Reference 6
- e. Reference 10

photoelectron angular distributions (PADs) at both wavelengths, characterized by the parameter β which is optimized such that

$$I(\theta) \propto 1 + \beta P_2(\cos\theta) \quad (6.1)$$

most accurately reproduces the PAD at a given energy. The best-fitting vibrational frequencies for the above modes are given in Table 6.1, which also summarizes existing vibrational data from gas phase and matrix isolation studies as well as the current *ab initio* calculations of the vibrational energies.

6.3. Discussion

The adiabatic electron affinities are determined directly from the *cis* and *trans* origins for HOCO and DOCO in the 775 nm spectra. For *cis*- and *trans*-HOCO respectively, these are 1.51 ± 0.01 eV and 1.38 ± 0.01 eV, with the HEAT-345(Q) EAs of 1.501 eV and 1.373 eV in better than 100 cm^{-1} agreement, within experimental errors. For the DOCO case, measured EAs are 1.51 eV and 1.37 eV, with similar error, again with good agreement from the calculated DOCO EAs of 1.501 and 1.371 respectively. These assignments of the higher-energy peaks to *trans*-HOCO rather than hot bands is further supported by the measured PADs at 775 nm, which show a small drop in anisotropy between the second to third peaks from what would be expected due to threshold effects,¹⁷ consistent with photodetachment from a slightly different molecular configuration. This anisotropy change is also seen in the 660 nm PADs beyond the *cis* origin.

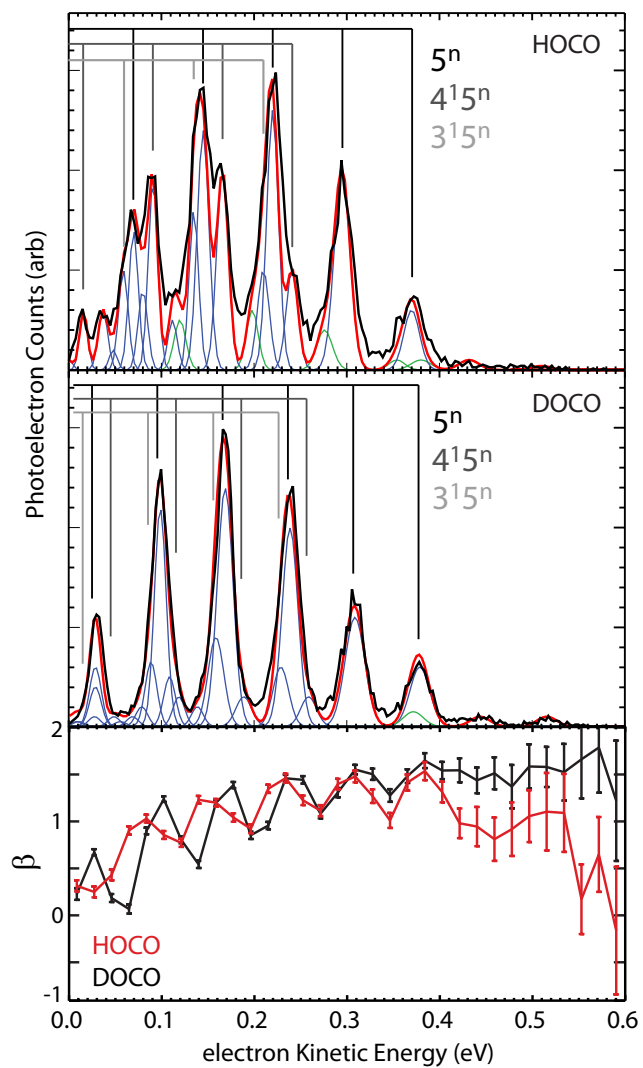


Figure 6.2: Photoelectron spectra and fits at 660 nm for HOCO (top) and DOCO (middle), with extracted anisotropy parameters (bottom) for both HOCO and DOCO (red and black, respectively).

With the EAs established, the simultaneous fits to the 660 and 775 nm spectra are obtained from harmonic combinations of ν_3 , ν_4 , and ν_5 in the *cis* isomer, and ν_5 in the *trans* isomer. The 660 nm HOCO spectrum is dominated by three primary sequences: 5^n , 4^15^n , and 3^15^n of the *cis* isomer. No vibrational excitation of ν_2 is resolved, with little predicted in Franck-Condon simulations. The OH stretching ν_1 mode is not energetically accessible at either wavelength, and is also not predicted to have strong excitation. The anion and neutral structures of both isomers are planar, so no excitation in ν_6 is expected or seen. The 5^1 band of the *trans* isomer is also resolved, though all other features from this isomer are obscured by the dominant *cis* isomer signal. Interestingly, in the case of DOCO, the three primary sequences show a significant degree of overlap, leading to a photoelectron spectrum that appears to contain excitation of only one mode. Though it is not possible to obtain resolved peaks corresponding to the different sets of bands in the DOCO spectrum, for composite peaks which are not limited by instrumental resolution the shape can be reproduced using the same fitting procedure. For example, the peak at 0.1 eV is composed of 5^5 , 3^15^3 , and 4^15^3 contributions, which when fit provide a reasonable estimate of ν_3 and ν_4 .

It is possible to estimate the relative populations of the two isomers in the ion beam by scaling the Franck-Condon simulated spectra of each isomer to fit the data. This method does not take into account the electronic transition cross-sections, but they are expected to be similar due to the high degree of similarity between the HOMOs of the two isomers.¹¹ Computed Franck-Condon factors (FCFs) are scaled by a function approximating the Wigner threshold law, implemented here as $a + b \cdot eKE^{0.5} + c \cdot eKE^{1.5}$.

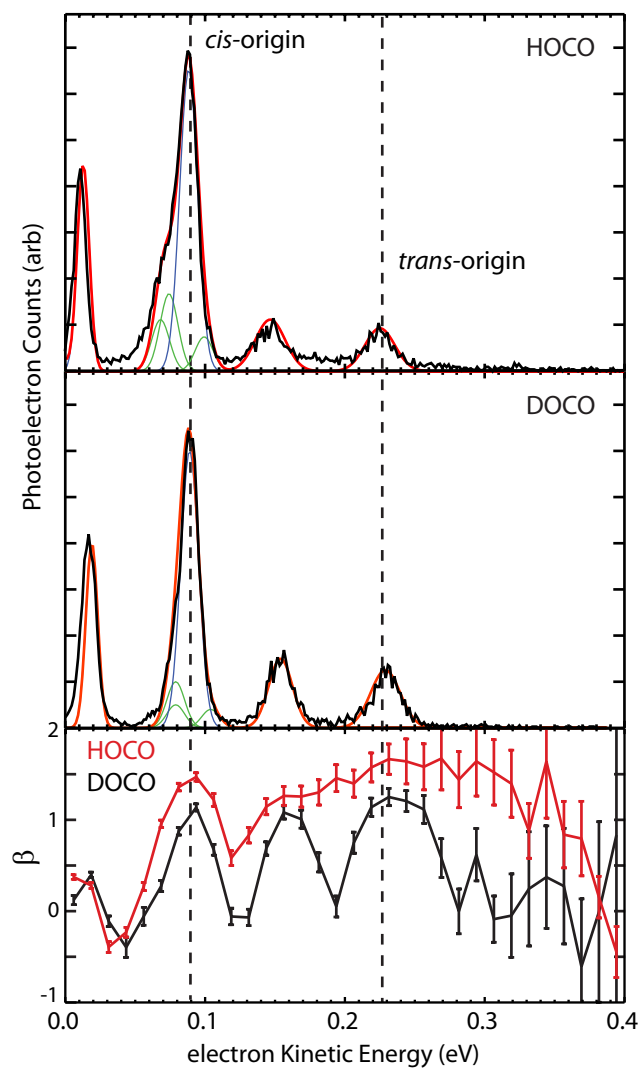


Figure 6.3: Similar to Figure 1, at 775 nm. The origins of *cis* and *trans* spectra are noted by dashed vertical lines.

The spectrum is then simulated by a summation of Gaussian peaks with centers at the calculated peak positions, widths from by the resolution function given in the text, and amplitudes set such that the area of the Gaussian equals the FCF for that peak. With both *cis* and *trans* spectra simulated, each is scaled to produce a best fit to the measured spectrum and the ratio of the scaling factors is used to compute the contribution of each isomer to the overall spectrum. The best fit *trans*-HOCO fractions range from 3-5%, and *trans*-DOCO 5-7%. Difficulties arise from properly accounting for threshold effects,¹⁷ giving rise to the 2% ranges given here.

In order to better resolve these *trans*-HOCO modes the 775 nm spectra were decomposed into appropriate contributions from *cis* and *trans* isomers and the peak heights and locations optimized to best reproduce the shape of the feature centered around 0.09 eV. Though this peak is primarily composed of the *cis*-HOCO origin, the low-energy shoulder was found to contain contributions from *trans*-HOCO 5² and 3¹ as well, allowing for more precise determination of ν_3 . The high energy side of the feature is expected to contain 4¹ but its contribution could not be conclusively extracted. Because this feature narrows significantly in the DOCO spectrum, the above analysis was unable to yield conclusive insight into these modes.

Interestingly, the origin and 5¹ bands of *trans*-HOCO in the 775 nm spectrum are found to be broader (~ 0.025 eV) than the instrument resolution at these energies, which has been found to scale approximately as $0.028 \cdot eKE + 0.010$ eV FWHM. The reason for this is not currently clear, though the potential for broad dipole-supported resonances as outlined by Miyabe *et al.* cannot be overlooked.¹⁵ It is also possible that the ion

formation mechanism, thought to be addition of OH^- to CO, induces a larger rotational temperature for the *trans*-isomer than that of the *cis* isomer, yielding peaks that are rotationally broadened. Given a rotational constant of $\sim 4 \text{ cm}^{-1}$, rotational temperatures of 140 K can reproduce the observed broadening. While no evidence of vibrational hot bands exists in the spectra, inefficient rotation-vibration coupling could lead to a long-lived nonstatistical distribution of energy between vibrational and rotational degrees of freedom. This mechanism could yield sequence bands, also capable of broadening the peaks. No power dependence was observed over a range of power densities from 2×10^{10} and $2 \times 10^9 \text{ W/cm}^2$.

Finally, by comparing these EAs with recent dissociative photodetachment studies of HOCO^- which found a maximum total energy release ($E_{tot} = eKE + \text{fragment translational energy}$) of 0.70 eV for the OH + CO dissociation channel,¹⁶ the well depths of the *cis* and *trans* isomers can be determined quite accurately. These well depths vary by more than 0.3 eV among the various high-level surfaces developed in the last decade.¹⁸⁻²¹ Given the assumption that the beam is essentially entirely *cis*-HOCO, the well depth as referenced to the OH + CO asymptotic energy can be determined by $D_0 = hv - E_{tot} - AEA$, and the *trans* well can be estimated using the absolute difference in energy calculated for the *cis*- and *trans*-HOCO wells. This calculation gives well depths of $0.99 \pm .02 \text{ eV}$ and $1.07 \pm .02 \text{ eV}$ for the *cis* and *trans* isomers, respectively, within the limit of 1.25 eV set by photoionization experiments on *trans*-HOCO²² and in the range of values calculated in the existing full surfaces. These errors are primarily due to uncertainty in the relative contributions of the instrument resolution and the product

Table 6.2: Calculated and experimental adiabatic electron affinities and well depths. Italicized numbers are referenced to the experimental *cis* values but calculated using the difference in energy between the *cis* and *trans* minima from *ab initio* calculations.

	AEA (eV) Exp.	AEA (eV) Calc.	D ₀ (eV) Exp.	D ₀ (eV) Calc.
<i>cis</i> -HOCO	1.51 ± .01	1.501	0.99 ± .02	1.01 ± .01
<i>cis</i> -DOCO	1.51 ± .01	1.501	0.99 ± .02	1.03 ± .01
<i>trans</i> -HOCO	1.38 ± .01	1.373	<i>1.07 ± .02</i>	1.08 ± .01
<i>trans</i> -DOCO	1.37 ± .01	1.371	<i>1.08 ± .02</i>	1.11 ± .01

rotational distribution for the coincidence data in Reference 16. The HEAT-345(Q) values for the well depths, which are available by combining the calculations here with those in 29, are 1.01 and 1.08 eV, respectively, in good agreement with the experimental values and with an expected error of ± 0.01 eV. These results, along with the AEAs are summarized in Table 6.2. If the OH + CO signal originates from *trans*-HOCO⁻, then these well depths are revised to 1.07 eV and 1.13 eV respectively, with the same error, which is inconsistent with the calculated values.

6.4. Experimental Methods

The photoelectron imaging studies were carried out in the same cryogenic-ion-trap photoelectron-photofragment coincidence spectrometer described in previous dissociative photodetachment studies of the OH + CO reaction.¹⁶ HOCO⁻(DOCO)⁻ anions were generated in a 10 Hz pulsed supersonic expansion of a 6% CO, 6% CH₄(CD₄), 13% N₂O, 75% argon gas mix through a pulsed coaxial discharge and crossed by a 1 keV electron beam. Ions were accelerated to 5 or 7 keV, mass selected by time-of-flight, and stored in a cryogenic electrostatic ion beam trap for periods of 100 msec to 1 sec. While trapped, ions are bunched and synchronized to a 1 kHz, 775 nm Ti:Sapphire amplifier and optical parametric amplifier (TOPAS) system providing <2 picosecond pulses at the fundamental and at 660 nm. Photoelectron spectra at both wavelengths were recorded in a velocity map imaging time- and position-sensitive photoelectron detector. Wavelengths were measured using a fiber optic spectrometer calibrated to a helium-neon discharge emission spectrum covering the 600-750 nm range. Photoelectron spectra are

calibrated against O^- photodetachment, which has an EA of approximately 1.46 eV,²³ similar to both isomers of HOCO.

6.5. Computational Methods

The latter were calculated at the CCSD(T) level of theory,²⁴ in conjunction with second-order vibrational perturbation theory (VPT2).²⁵ These *ab initio* calculations, which were done in the frozen-core approximation, used the atomic natural orbital (ANO) basis sets of Almlöf and Taylor.²⁶ The harmonic frequencies (as well as the anharmonicity constants) were calculated using the 4s2p1d (on H); 4s3p2d1f (other atoms) truncation known as ANO1; the harmonic frequencies were determined with the ANO2 basis set, which is contracted as 4s3p2d1f (H); 5s4p3d2f1g (other atoms). The values given in table 1 are the harmonic levels from the ANO2 calculations; and the VPT2 results obtained by using the ANO2 harmonic force field together with the ANO1 cubic and quartic force constants.

Electron affinities of both isomers were calculated using the HEAT (High Accuracy Extrapolated Thermochemistry)²⁷ protocol known as HEAT-345(Q).^{28,29} In this work, however, the zero-point vibrational correction to the energies of all species involved (both conformers and their anions) were obtained at the CCSD(T)/ANO1 level, instead of the CCSD(T)/cc-PVQZ level which is the standard approach. Use of the former is certainly less expensive, and (based on its performance in predicting vibrational frequencies³⁰) at least as accurate. All calculations done here were carried out with the CFOUR quantum chemistry package.³¹

Acknowledgements

The text of this Chapter is adapted from the following publication, of which the dissertation author is the primary author and the dissertation advisor is the corresponding author:

Johnson, Christopher J., Harding, Michael E., Poad, Berwyck L. J., Stanton, John F., and Continetti, R. E. JACS, submitted (2011).

References

- (1) Berry, R. S.; Lehman, P. A. *Annu. Rev. Phys. Chem.* **1971**, *22*, 47.
- (2) Smith, I. W. M. *Chem. Phys. Lett.* **1977**, *49*, 112.
- (3) Francisco, J. S.; Muckerman, J. T.; Yu, H.-G. *Accounts Chem. Res.* **2010**, *43*, 1519.
- (4) Milligan, D. E.; Jacox, M. E. *J. Chem. Phys.* **1971**, *54*, 927.
- (5) Jacox, M. E. *J. Chem. Phys.* **1988**, *88*, 4598.
- (6) Forney, D.; Jacox, M. E.; Thompson, W. E. *J. Chem. Phys.* **2003**, *119*, 10814.
- (7) Petty, J. T.; Moore, C. B. *J. Mol. Spectrosc.* **1993**, *161*, 149.
- (8) Petty, J. T.; Harrison, J. A.; Moore, C. B. *J. Phys. Chem.* **1993**, *97*, 11194.
- (9) Petty, J. T.; Moore, C. B. *J. Chem. Phys.* **1993**, *99*, 47.
- (10) Sears, T. J.; Fawzy, W. M.; Johnson, P. M. *J. Chem. Phys.* **1992**, *97*, 3996.
- (11) Oyama, T.; Funato, W.; Sumiyoshi, Y.; Endo, Y. *J. Chem. Phys.* **2011**, *134*, 174303.
- (12) Clements, T. G.; Continetti, R. E.; Francisco, J. S. *J. Chem. Phys.* **2002**, *117*, 6478.
- (13) Dixon, D. A.; Feller, D.; Francisco, J. S. *J. Phys. Chem. A* **2003**, *107*, 186.
- (14) Lu, Z.; Continetti, R. E. *Phys. Rev. Lett.* **2007**, *99*, 113005.
- (15) Miyabe, S.; Haxton, D. J.; Lawler, K. V.; Orel, A. E. *Phys. Rev. A* **2011**, *83*, 043401.
- (16) Johnson, C. J.; Continetti, R. E. *J. Phys. Chem. Lett.* **2010**, *1*, 1895.
- (17) Farley, J. W. *Phys. Rev. A* **1989**, *40*, 6286.
- (18) Yu, H. G.; Muckerman, J. T.; Sears, T. J. *Chem. Phys. Lett.* **2001**, *349*, 547.
- (19) Lakin, M. J.; Troya, D.; Schatz, G. C.; Harding, L. B. *J. Chem. Phys.* **2003**, *119*, 5848.
- (20) Valero, R.; Hemert, M. C. van; Kroes, G. J. *Chem. Phys. Lett.* **2004**, *393*, 236.

- (21) Song, X.; Li, J.; Hou, H.; Wang, B. *J. Chem. Phys.* **2006**, *125*, 94301.
- (22) Ruscic, B.; Schwarz, M.; Berkowitz, J. *J. Chem. Phys.* **1989**, *91*, 6780.
- (23) Ervin, K. M.; Anusiewicz, W.; Skurski, P.; Simons, J.; Lineberger, W. C. *J. Phys. Chem. A* **2003**, *107*, 8521.
- (24) Raghavachari, K.; Trucks, G. W.; Pople, J. A.; Head-Gordon, M. *Chem. Phys. Lett.* **1989**, *157*, 479.
- (25) Mills, I. M. Academic Press: New York, 1972; p. 115.
- (26) Almlöf, J.; Taylor, P. R. *J. Chem. Phys.* **1987**, *86*, 4070.
- (27) Tajti, A.; Szalay, P. G.; Csaszar, A. G.; Kallay, M.; Gauss, J.; Valeev, E. F.; Flowers, B. A.; Vazquez, J.; Stanton, J. F. *J. Chem. Phys.* **2004**, *121*, 11599.
- (28) Bomble, Y. J.; Vazquez, J.; Kallay, M.; Michauk, C.; Szalay, P. G.; Csaszar, A. G.; Gauss, J.; Stanton, J. F. *J. Chem. Phys.* **2006**, *125*, 064108.
- (29) Harding, M. E.; Vazquez, J.; Ruscic, B.; Wilson, A. K.; Gauss, J.; Stanton, J. F. *J. Chem. Phys.* **2008**, *128*, 114111.
- (30) Vazquez, J.; Harding, M. E.; Stanton, J. F. Unpublished Research.
- (31) CFOUR, Coupled-Cluster techniques for Computational Chemistry, a quantum-chemical program package by J.F. Stanton, J. Gauss, M.E. Harding, P.G. Szalay with contributions from A.A. Auer, R.J. Bartlett, U. Benedikt, C. Berger, D.E. Bernholdt, Y.J. Bomble, L. Cheng, O. Christiansen, M. Heckert, O. Heun, C. Huber, T.-C. Jagau, D. Jonsson, J. Jusélius, K. Klein, W.J. Lauderdale, D.A. Matthews, T. Metzroth, D.P. O'Neill, D.R. Price, E. Prochnow, K. Ruud, F. Schiffmann, W. Schwalbach, S. Stopkowicz, A. Tajti, J. Vázquez, F. Wang, J.D. Watts and the integral packages *MOLECULE* (J. Almlöf and P.R. Taylor), *PROPS* (P.R. Taylor), *ABACUS* (T. Helgaker, H.J. Aa. Jensen, P. Jørgensen, and J. Olsen), and ECP routines by A. V. Mitin and C. van Wüllen. For the current version, see <http://www.cfour.de>.

Chapter 7. Global Dissociative Photodetachment

Dynamics of the HOCO Anion

7.1. Introduction

The preceding chapters describe specific elements of this study of the OH + CO reaction. This chapter will serve as a capstone to develop a global picture of the dissociative photodetachment process in the HOCO⁻ system, and to reveal the insights gained into the bulk reaction $\text{OH} + \text{CO} \rightarrow \text{H} + \text{CO}_2$ during this set of experiments. For reference, an *ab initio* calculation¹ of the stationary points and connectivity of the HOCO PES is given in Figure 7.1. Improvements in the energies of the stationary points, as outlined in Chapter 6, are crucial for accurate calculations of processes occurring on this PES, but this is not sufficient to properly capture the dynamics of these processes. Even for a molecule as small as HOCO, full first-principles calculations, taking into account all processes that could possibly occur, are currently unfeasible. This necessitates the phenomenological inclusion of corrections for processes such as tunneling, internal vibrational redistribution (IVR), or isomerization into statistical and dynamical models of the reaction. The following discussion, while largely qualitative, represents some of the first experimental insights into these specific processes in the OH + CO reaction, and will hopefully serve as a guide for future experimental and theoretical efforts.

7.2. The OH + CO Channel

The OH + CO product channel has been largely ignored in this thesis, and by

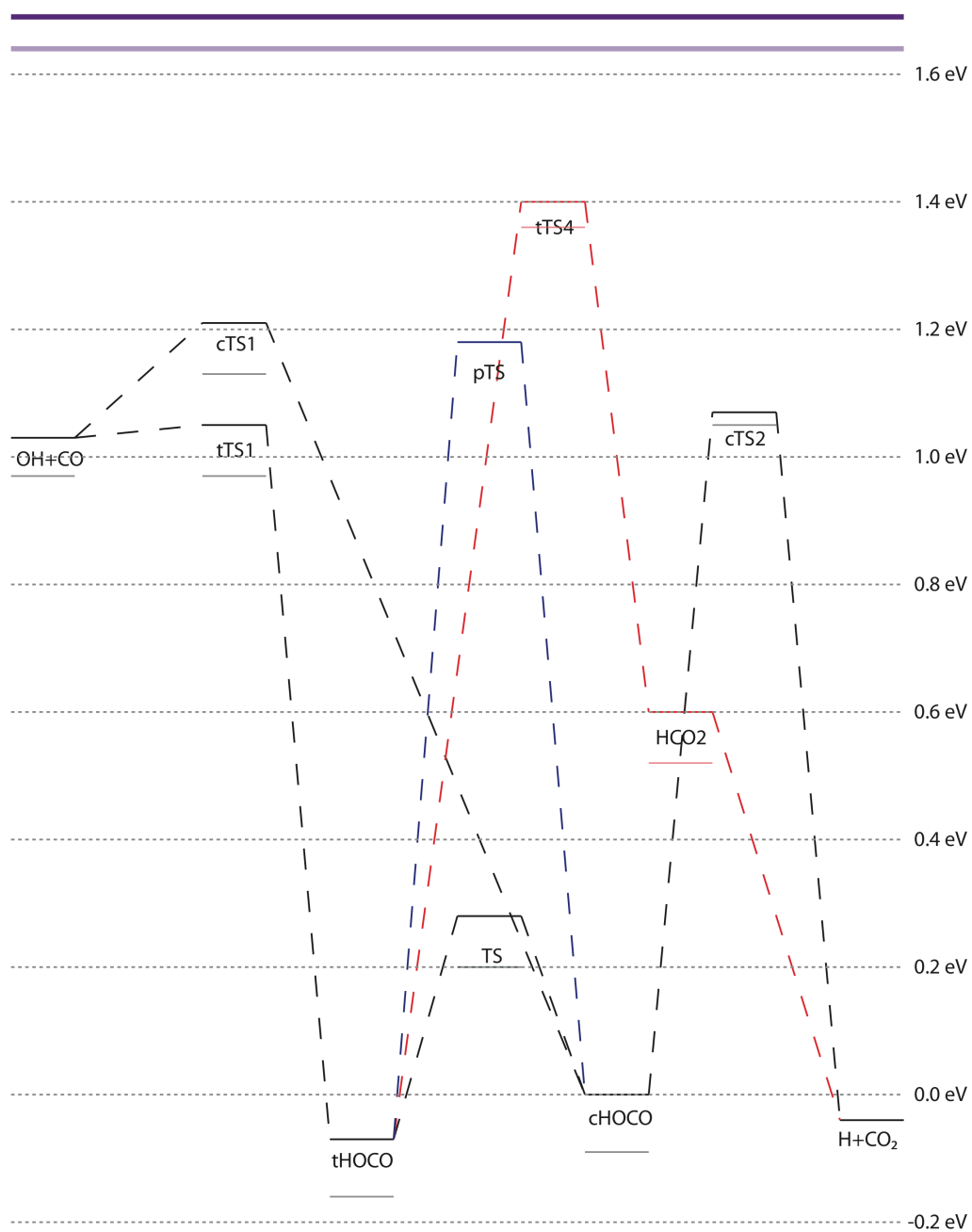


Figure 7.1: A computed potential energy surface for neutral HOCO.¹¹ Dark and light purple lines indicate the level of laser excitation for HOCO and DOCO respectively. Thin lines below each state are the DOCO energies.

itself contains the least new information of the three processes seen in these experiments. However, as the entrance channel of the reaction, it is of critical importance, and an understanding of its role in DPD will help to connect this work to the overall reaction dynamics. Assuming microscopic reversibility, that the process $\text{OH} + \text{CO} \rightarrow \text{HOCO}^*$ is identical to $\text{HOCO}^* \rightarrow \text{OH} + \text{CO}$, then the back reaction studied here allows this connection to be made. The coincidence spectrum for the $\text{OH} + \text{CO}$ channel is shown in Figure 7.2 for both hot² and cold³ experiments. The stark contrast between the two will be discussed in Section 7.6 but for the purposes of this section only the cold spectrum holds relevant information.

It is immediately clear that no vibration is present in either fragment. Analysis of the single diagonal band shows a FWHM of 0.08 eV in the total kinetic energy spectrum (Figure 7.3), setting an upper limit to the internal energy of the anions, or conversely to the internal energy of the OH and CO products. This feature can be fit to a two-component Boltzmann rotational distribution, assuming equipartition of energy between the fragments with $B_e(\text{OH}) = 18.9 \text{ cm}^{-1}$ and $B_e(\text{CO}) = 1.93 \text{ cm}^{-1}$,^{4,5} to find an upper limit of 250 K to the internal temperature of the products. The actual value is likely significantly smaller due to the extra contribution of the experimental resolution and ion internal temperature to the overall width. The diagonal feature is peaked very close to zero KER, implying that in the Franck-Condon region of the anion, the neutral potential energy surface is very flat. This is not entirely surprising, as the anionic central OC bond length is 0.2 Å longer than the neutral,⁶ with OH and CO equilibrium bond lengths close to those of the individual diatomics. In the case of $\text{DOCO} \rightarrow \text{OD} + \text{CO}$, this band is

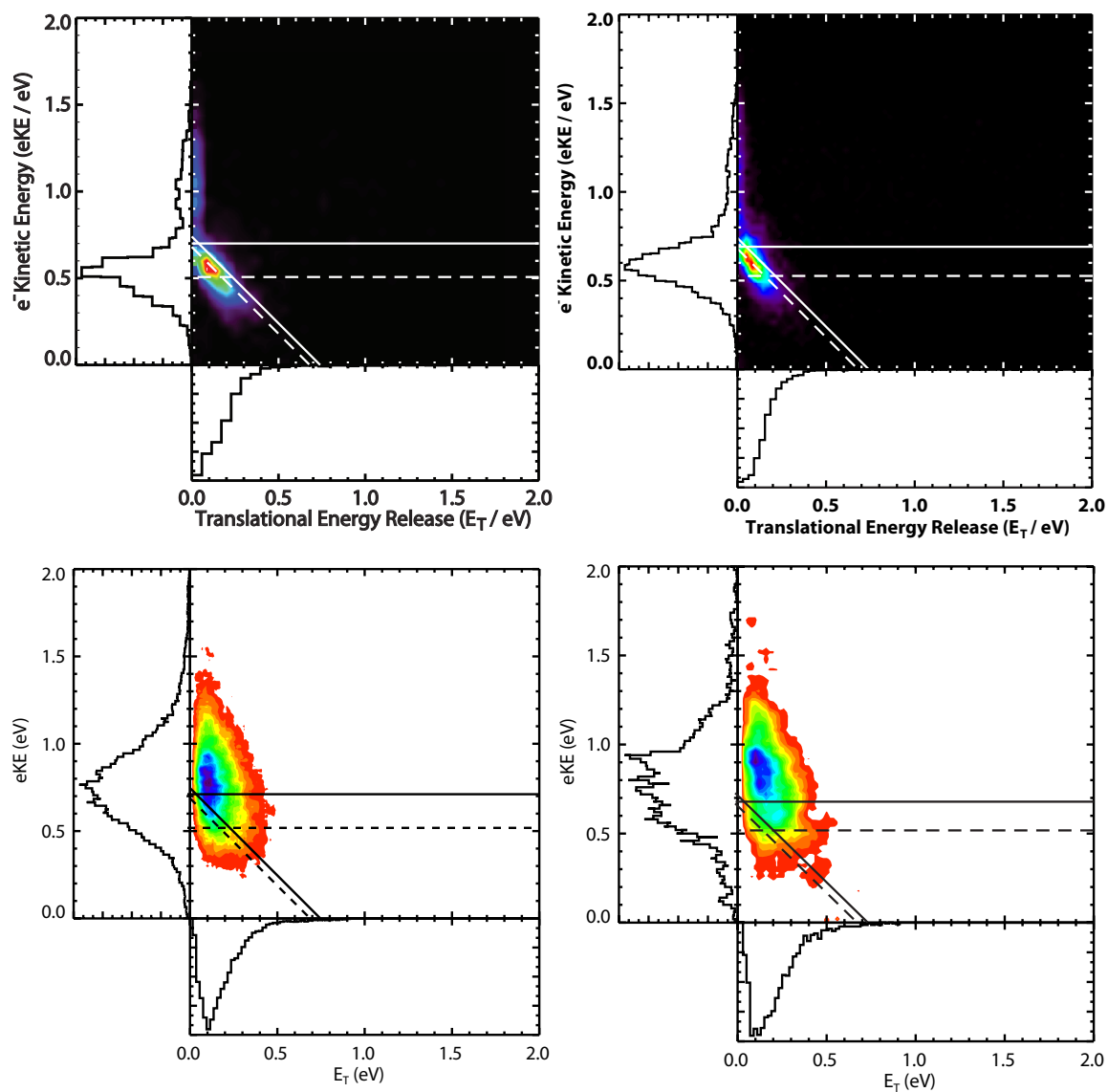


Figure 7.2: Comparison of cold (top) and hot (bottom) $\text{HOCO} \rightarrow \text{OH} + \text{CO}$ coincidence spectra. HOCO spectra are given on the left, while DOCO is on the right. Diagonal lines represent the predicted maximum E_{tot} for *trans*- (solid) and *cis*- (dashed) $\text{HOCO}^- \rightarrow \text{OH} + \text{CO} + e^-$, while horizontal lines represent the predicted maximum eKE for dissociation over the respective barriers (see Figure 7.1).

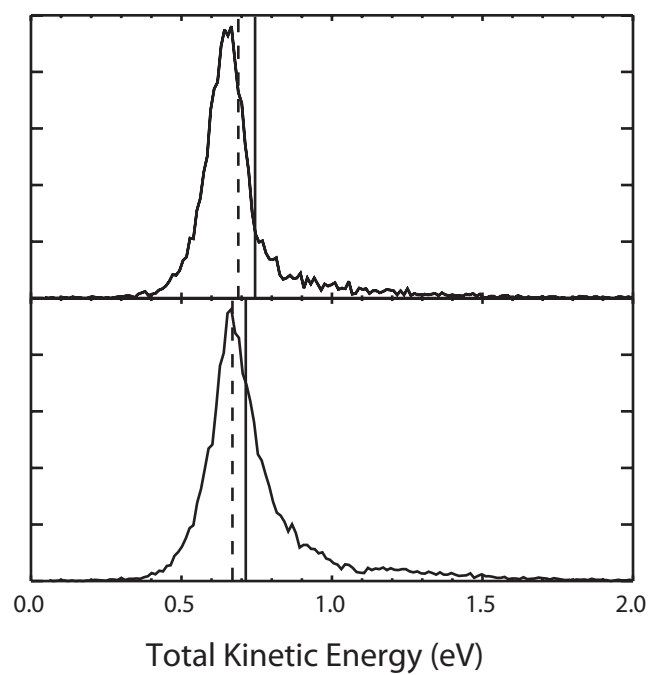


Figure 7.3: Comparison of total energy release for HOCO (top) and DOCO (bottom). Vertical lines represent the maximum total energy expected for *trans*- (solid) and *cis*- (dashed) $\text{HOCO}^- \rightarrow \text{H} + \text{CO}_2 + \text{e}^-$.

slightly wider at 0.10 eV FWHM. It is not clear if the OD + CO rotational distribution is indeed larger than OH + CO, or if other factors are causing this broadening.

7.3. **cis-trans Isomerization**

Interestingly, most of the dissociation to OH + CO found in these experiments occurs from detachment to HOCO* with internal energy below the barrier from *cis*-HOCO to OH + CO but above that of *trans*-HOCO. It was shown in Chapter 6 that the composition of the beam appears to be primarily *cis*-HOCO⁻, giving rise to two possible explanations: that dissociation to OH + CO in this internal energy range proceeds exclusively from *trans*-HOCO anions, or that neutrals which are initially *cis* must first isomerize to *trans*-HOCO prior to dissociation. The energy-resolved branching fractions for DPD of HOCO show that in this energy range, there is competition between the OH + CO and H + CO₂ channels, leading to roughly equal amounts of each product. However, above the barrier from *cis*-HOCO to OH + CO, the only product is OH + CO, implying that, when energetically allowed, this dissociation is significantly faster to the also-allowed dissociation to H + CO₂. These observations are consistent with the isomerization mechanism, with the process of isomerization from *cis*- to *trans*-HOCO occurring at a similar rate to dissociation to H + CO₂, and dissociation of *trans*-HOCO to OH + CO occurring very quickly. This argument is further reinforced by the observation that this region of competition is not present in DOCO, where all signal in this energy range leads to dissociation to OD + CO. Here the isomerization and OD + CO barriers all shift to lower energy due to the reduction in zero-point energy upon deuteration, while the barrier to D + CO₂ remains essentially constant since the OH stretch is unbound here. This shift in relative energies is more than sufficient to explain the loss of the competition

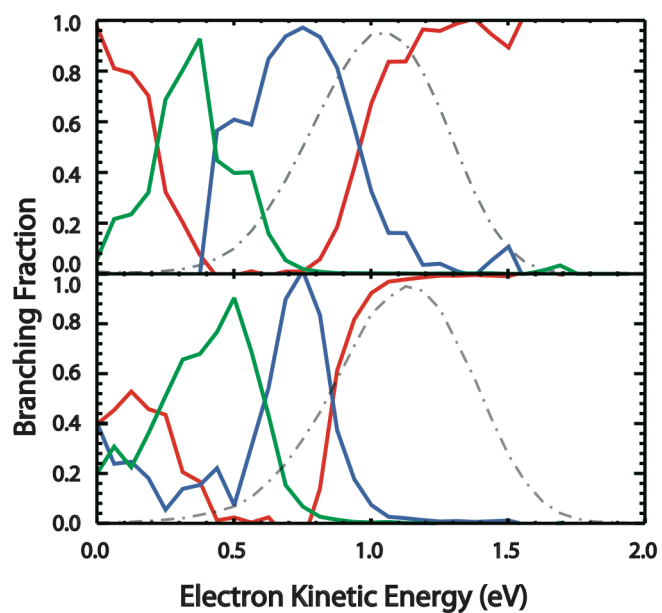


Figure 7.4: Energy-resolved branching fractions for HOCO (top) and DOCO (bottom). Detachment to stable HOCO is shown in red, dissociation to $\text{H} + \text{CO}_2$ in blue, and dissociation to $\text{OH} + \text{CO}$ in green.

feature. Unfortunately, with the current data other mechanisms cannot be conclusively ruled out, and it remains possible that this signal does indeed originate from *trans*- anions. If this is the case, then the noted competition must arise from a combination of a small number of *trans* anions with fast dissociation to OH + CO and a large number of *cis* anions with only slightly slower dissociation to H + CO₂. Future experiments modulating the relative populations of isomers in the beam will definitively answer this question, with two methods already shown to work in other ion beam experiments.^{7,8}

The mechanism behind this isomerization requires additional consideration. The lowest-lying isomerization transition state is out-of-plane, requiring at least four quanta in the torsional mode to pass the barrier. However, since both the anion and neutral for both isomers are planar, no torsional excitation is expected upon photodetachment. This requires either a mechanism to redistribute energy from modes with planar symmetry to out-of-plane modes (disallowed in the harmonic approximation), or a higher-lying planar isomerization transition state through which the system can pass without requiring torsional motion. In order to transfer energy from planar to torsional modes, it is necessary to have either strong anharmonic couplings between the torsional mode and at least one other mode, a resonance such as Fermi resonance, or to have strong Coriolis coupling. High-level anharmonic vibrational calculations show non-negligible couplings on the order of 10 cm⁻¹ between the torsional mode and both the central OC stretch and HOC wagging modes, raising the possibility that this mechanism could be active in HOCO.⁹ While these effects have been shown to allow vibrational redistribution on the picosecond to nanosecond timescale, accurate calculations of both effects are still

difficult even for triatomic molecules without detailed experimental data, which has only recently been measured.¹⁰

For the case of planar isomerization, no first-order stationary point corresponding to this process has been located on the high-level HOCO PESs. Lower-level efforts have been made, yielding a second-order stationary point with imaginary frequencies in both the torsional and HOC wagging modes. Accurate calculations of the energy of this geometry are more sophisticated than those performed in other parts of this thesis owing to the multiconfigurational nature of this transition state, and have not been pursued. Preliminary transition state energies fall within 0.3 eV of the proposed isomerization energy range, calculated at the CCSD/aug-cc-pVTZ level of theory,¹¹ leading to some suspicion that more sophisticated calculations may show that this process is energetically allowed. Due to the variational nature of quantum chemistry calculations, more rigorous calculations can be expected to yield even lower energies.

This process can be analyzed using a similar method to that in Chapter 5, though here the barrier is assumed to be an Eckart potential which is known to be a reasonable approximation for a variety of molecular processes.¹² Tunneling coefficients for the Eckart barrier are given by

$$T(E) = \frac{\sinh a \sinh b}{\sinh^2 [(a + b)/2] + \cosh^2 c} \quad (7.1)$$

where

$$a = \frac{4\pi}{h\nu_v} \frac{(\epsilon_t + V_0)^{\frac{1}{2}}}{V_0^{\frac{1}{2}} + V_1^{\frac{1}{2}}} \quad (7.1a)$$

$$b = \frac{4\pi (\epsilon_t + V_1)^{\frac{1}{2}}}{h\nu_v V_0^{\frac{1}{2}} + V_1^{\frac{1}{2}}} \quad (7.1b)$$

$$c = 2\pi \left(\frac{V_0 V_1}{h\nu_c} - \frac{1}{16} \right)^{\frac{1}{2}} \quad (7.1c)$$

and V_0 and V_1 are the energies below the barrier of the *cis* and *trans* wells respectively, 0.99 and 1.07 eV as found in Chapter 6. The parameter ν_c is the imaginary frequency characterizing the curvature of the top of the barrier, which was found to be 1202 cm^{-1} in the calculation presented in the preceding paragraph. These values lead to a tunneling coefficient of 1.5×10^{-6} , quite low, but this process needs only to be competitive with tunneling to $\text{H} + \text{CO}_2$ to be active. From Figure 5.5 it is clear that, at these energies, the tunneling lifetime ($1/e$) to $\text{H} + \text{CO}_2$ is approximately 100 ps. For isomerization, the most directly active normal mode of *cis*-HOCO is the HOC bend, with a frequency of 38 THz. From this, a lifetime for tunneling to *trans*-HOCO of 18 ns is found, significantly higher than the predicted $\text{H} + \text{CO}_2$ lifetime.¹³ However, further refinements to the transition state energy should further reduce its energy, making this process more viable.

7.4. The $\text{H} + \text{CO}_2$ Channel

Since this channel has already been discussed in detail in Chapter 5, discussion here will remain limited to its role in the overall dynamics of the reaction. It is apparent from these experiments that, at all tunneling energies, CO_2 fragments are created with significant amounts of internal excitation. In this case, the internal energy distribution is highly inverted, with most CO_2 molecules in $v=3$ of the OCO bend mode, and thus the assignment of a temperature is irrelevant. Understanding the dynamical mechanism behind this product channel is somewhat easier than for $\text{OH} + \text{CO}$ because dissociation

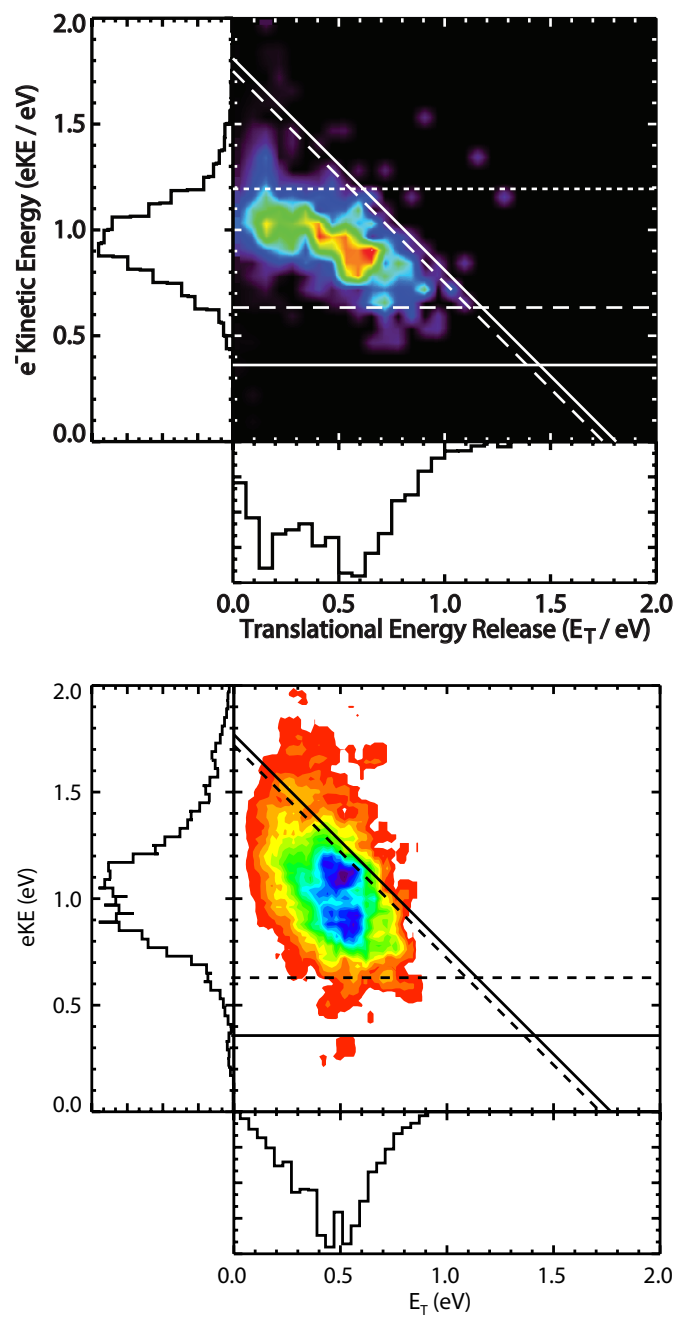


Figure 7.5: Comparison of cold (top) and hot (bottom) $\text{HOCO} \rightarrow \text{H} + \text{CO}_2$ coincidence spectra. Horizontal and vertical lines carry the same meaning as in Figure 7.2.

can only occur from *cis*-HOCO at these energies, and isomerization takes place much more slowly than at the OH + CO channel energy. It was shown in Chapter 5 that significant vibrational energy redistribution among the internal modes of *cis*-HOCO must occur for tunneling dissociation to become probable. This means that, as opposed to the OH + CO case in which the dissociation dynamics are driven largely by the shape of the surface in the anion Franck-Condon region immediately upon photodetachment, in the H + CO₂ channel the system has a relatively long time (up to microseconds) to explore the *cis*-HOCO potential well. By removing the strong influence of the Franck-Condon geometry from the overall dynamics, the DPD experiment can be expected to be a good approximation of the bulk dynamics of the reaction in this energy range.

7.5. Product Branching

The energy-resolved branching fractions for HOCO and DOCO DPD have already been used extensively to extract specific information about processes occurring in two energetic ranges of the PES. A simpler metric for comparison of the results of DPD studies to those from other experiments is the overall branching ratios, the absolute number of events in each product channel divided by the total number of events. These results are summarized in Table 7.1 for three DPD experiments performed in this lab^{2,6} as well as a dissociative charge exchange (DCE) experiment on the neutralization of HOCO⁺ in collisions with cesium.¹⁴ A dramatic increase in the H + CO₂ fraction is apparent, with an equally dramatic decrease in the OH + CO fraction. Clearly, cooling of the precursor anions has a significant effect on the measured dynamics, which will be discussed in an ensuing section. The DCE experiments can not be directly compared to the PPC experiments since a fundamentally different region of the HOCO PES is probed

Table 7.1: Comparison of measured branching ratios. 258 nm data is from Ref. 6, hot data is from Ref. 2, DCE data from Ref. 14, and cold data from this work.

	258 nm	388 nm (hot)	DCE	388 nm (cold)
Stable	0.81	0.67	N/A	0.55
OH + CO	0.13	0.17	0.75	0.03
H + CO ₂	0.06	0.16	0.25	0.42

in this process. However, the DCE results serve to confirm the prevalence of the OH + CO channel on the surface, even for the qualitatively different vibrational excitation induced by charge exchange.

7.6. The Impact of Cooled Anions

This entire thesis is predicated on the idea that significant gains in the understanding of the OH + CO reaction will be achieved by cooling the precursor anions, thereby achieving higher energy resolution in DPD experiments. Figures 7.2 and 7.5 show that while spectral features are indeed more well resolved, even more significant effects are found. Of particular interest is the relative changes in the OH + CO and H + CO₂ coincidence spectra. In the H + CO₂ case, the horizontal feature apparent in the cold data is significantly broadened in the hot data, no longer being easily identifiable as a tunneling feature and adding significant uncertainty to the internal energy measurement. However, both of these spectra are qualitatively similar with strong overlap between the hot and cold signal.

The OH + CO spectra are almost entirely different – almost no signal exists in the hot spectrum in the region of the cold spectrum, indicating that dissociation to OH + CO is very strongly modulated by the anion internal energy. It could be naively expected that internal energy in the anion central OC stretching motion, the OH + CO dissociation coordinate, would most likely lead to an increase in the yield of OH + CO products. In a multidimensional system such as HOCO with an apparently flat potential energy surface in the OH + CO → HOCO entrance channel, the situation is significantly more complex as even small modulations can significantly effect the dynamics on the PES. Even more, the wave functions, consisting of both bound and unbound dimensions, are very difficult

to calculate or even visualize so accurate Franck-Condon factors in this region are nearly impossible to predict.

While complicating the comparison of the hot and cold data sets, this difficulty also provides a significant opportunity for a systematic study of the potential energy surface in this region. By specifically exciting particular vibrational modes in the anion, the Franck-Condon region can be modulated in a well-controllable way. By comparing the dynamics as a function of the excited mode, and thus the initial geometry for the neutralized HOCO radical, the yields of processes and internal energy partitioning can be mapped as a function of normal coordinates to identify the most critical coordinates governing dissociation.¹⁵ Development of a method to perform these measurements is currently underway and should yield unprecedented information about the fine structure of the HOCO PES.

7.7. Conclusions

The contents of this thesis represent the most exhaustive study to date of the detailed dynamics and energetics of the PES governing the reaction $\text{OH} + \text{CO} \rightarrow \text{H} + \text{CO}_2$. This critical but still poorly understood reaction serves as a benchmark for theoretical treatments of molecular reaction dynamics, and the set of data presented here provides the most stringent test of these theories. The existence of highly energetically resolved results directly probing the PES adds significant new constraints to the study of this reaction, as a truly successful theory must be capable of reproducing both thermally averaged bulk kinetic data as well as nonstatistical direct dynamics data such as that presented here. The additional spectroscopic data presented in this thesis will also aid the construction of even more accurate PESs, with benchmark heats of formation and

vibrational energies which must be matched by *ab initio* calculations to verify their accuracy. With several new theoretical studies currently underway as a result of publications from this thesis, it is likely that these results will play an important role in developing a deeper understanding of this chemical reaction.

7.8. Future Directions

Two future experiments have already been mentioned in this chapter, modulation of the isomer populations and vibrational excitation of the anions. An important element to the formation of HOCO in thermal reactions is stabilization by a third body.¹⁶ If the reaction $\text{OH} + \text{CO} \rightarrow \text{HOCO}^*$ is indeed microscopically reversible, in order to form a stable or metastable HOCO intermediate energy must be removed from the excited intermediate to close the possibility of dissociation back to $\text{OH} + \text{CO}$. This effect could be expected to be highly species-dependent, so clusters of HOCO with other atmospheric- or combustion-relevant molecules could show a significant rate increase or decrease for CO_2 production. Additionally, the unique two-photon resonance in HOCO^- photodetachment provides an ideal opportunity for two-color coherent control,¹⁷ potentially leading to the first demonstration of chemical control over an important elementary chemical reaction.

Not discussed in this thesis is the importance of the HOCO^- anion. This species has been proposed to be important in organic and biological mass spectrometry, as a fragmentation product of carboxylic acids. Furthermore, the similarity of the anionic CO bond length to that of lone CO implies that this species could be important as a model for atmospheric CO_2 reduction schemes. Virtually no information about the anion is known,

and studies of its PES and vibrational structure could yield significant insights into this important and timely problem.

References

- (1) Yu, H.; Muckerman, J.; Sears, T. *Chem. Phys. Lett.* **2001**, *349*, 547.
- (2) Lu, Z.; Hu, Q.; Oakman, J. E.; Continetti, R. E. *J. Chem. Phys.* **2007**, *126*, 194305.
- (3) Johnson, C. J.; Continetti, R. E. *J. Phys. Chem. Lett.* **2010**, *1*, 1895.
- (4) Fallon, R.; Vanderslice, J.; Tobias, I. *J. Chem. Phys.* **1961**, *34*, 167.
- (5) Tobias, I.; Fallon, R.; Vanderslice, J. *J. Chem. Phys.* **1960**, *33*, 1638.
- (6) Clements, T.; Continetti, R.; Francisco, J. *J. Chem. Phys.* **2002**, *117*, 6478.
- (7) Relph, R. A.; Bopp, J. C.; Johnson, M. A.; Viggiano, A. A. *J. Chem. Phys.* **2008**, *129*, 064305.
- (8) Roscioli, J. R.; Johnson, M. A. *J. Chem. Phys.* **2007**, *126*, 024307.
- (9) Harding, M. E.; Stanton, J. F. Private Communication.
- (10) Gruebele, M.; Bigwood, R. *Int. Rev. Phys. Chem.* **1998**, *17*, 91.
- (11) Frisch, M. J.; Trucks, G. W.; Schlegel, H. B.; Scuseria, G. E.; Robb, M. A.; Cheeseman, J. R.; Scalmani, G.; Barone, V.; Mennucci, B.; Petersson, G. A.; Nakatsuji, H.; Caricato, M.; Li, X.; Hratchian, H. P.; Izmaylov, A. F.; Bloino, J.; Zheng, G.; Sonnenberg, J. L.; Hada, M.; Ehara, M.; Toyota, K.; Fukuda, R.; Hasegawa, J.; Ishida, M.; Nakajima, T.; Honda, Y.; Kitao, O.; Nakai, H.; Vreven, T.; Montgomery, J. A., Jr; Peralta, J. E.; Ogliaro, F.; Bearpark, M.; Heyd, J. J.; Brothers, E.; Kudin, K. N.; Staroverov, V. N.; Kobayashi, R.; Normand, J.; Raghavachari, K.; Rendell, A.; Burant, J. C.; Iyengar, S. S.; Tomasi, J.; Cossi, M.; Rega, N.; Millam, N. J.; Klene, M.; Knox, J. E.; Cross, J. B.; Bakken, V.; Adamo, C.; Jaramillo, J.; Gomperts, R.; Stratmann, R. E.; Yazyev, O.; Austin, A. J.; Cammi, R.; Pomelli, C.; Ochterski, J. W.; Martin, R. L.; Morokuma, K.; Zakrzewski, V. G.; Voth, G. A.; Salvador, P.; Dannenberg, J. J.; Dapprich, S.; Daniels, A. D.; Farkas, O.; Foresman, J. B.; Ortiz, J. V.; Cioslowski, J.; Fox, D. J. *Gaussian 09*.
- (12) Baer, T.; Hase, W. L. *Unimolecular Reaction Dynamics*; Oxford University Press: New York, 1996.
- (13) Johnson, C. J.; Poad, B. L. J.; Shen, B. B.; Continetti, R. E. *J. Chem. Phys.* **2011**, *134*, 117106.
- (14) Savee, J. D.; Mann, J. E.; Continetti, R. E. *J. Phys. Chem. A* **2010**, *114*, 1485.

- (15) Annesley, C. J.; Berke, A. E.; Crim, F. F. *J. Phys. Chem. A* **2008**, *112*, 9448.
- (16) Francisco, J. S.; Muckerman, J. T.; Yu, H.-G. *Accounts Chem. Res.* **2010**, *43*, 1519.
- (17) Dantus, M.; Lozovoy, V. *Chem. Rev.* **2004**, *104*, 1813.

Chapter 8. Photoelectron Angular Distributions in Two-photon Photodetachment of NO_2^-

8.1. Introduction

Nitrogen dioxide has been an interesting and difficult subject in spectroscopy, in part due to its complex low-lying electronic structure shown in Figure 1, and also its importance in atmospheric oxidation processes and combustion. The optical spectroscopy of NO_2 has been exhaustively studied^{1,2} and photoelectron spectroscopy has provided significant insight into the geometries of the NO_2^- anion and the first few electronic states of the neutral.³⁻⁵ Over the last several decades there has been increasing interest in multiphoton photoelectron techniques due to their ability to resolve time-dependent processes,⁶ their increased species-specificity,⁷ the inherent novelty of the associated physics, and the increased information content in their photoelectron angular distributions (PADs).⁸ For resonant techniques, additional information may also be obtained due to the orientationally selective nature of absorption of the first photon giving rise to PADs from molecules which are no longer averaged over all orientations with respect to the laser E-vector.⁹

The case of non-resonant multiphoton detachment of molecules has received relatively little attention. Multiphoton detachment of atomic H^- has been measured and compared to available models showing good agreement between predicted and observed

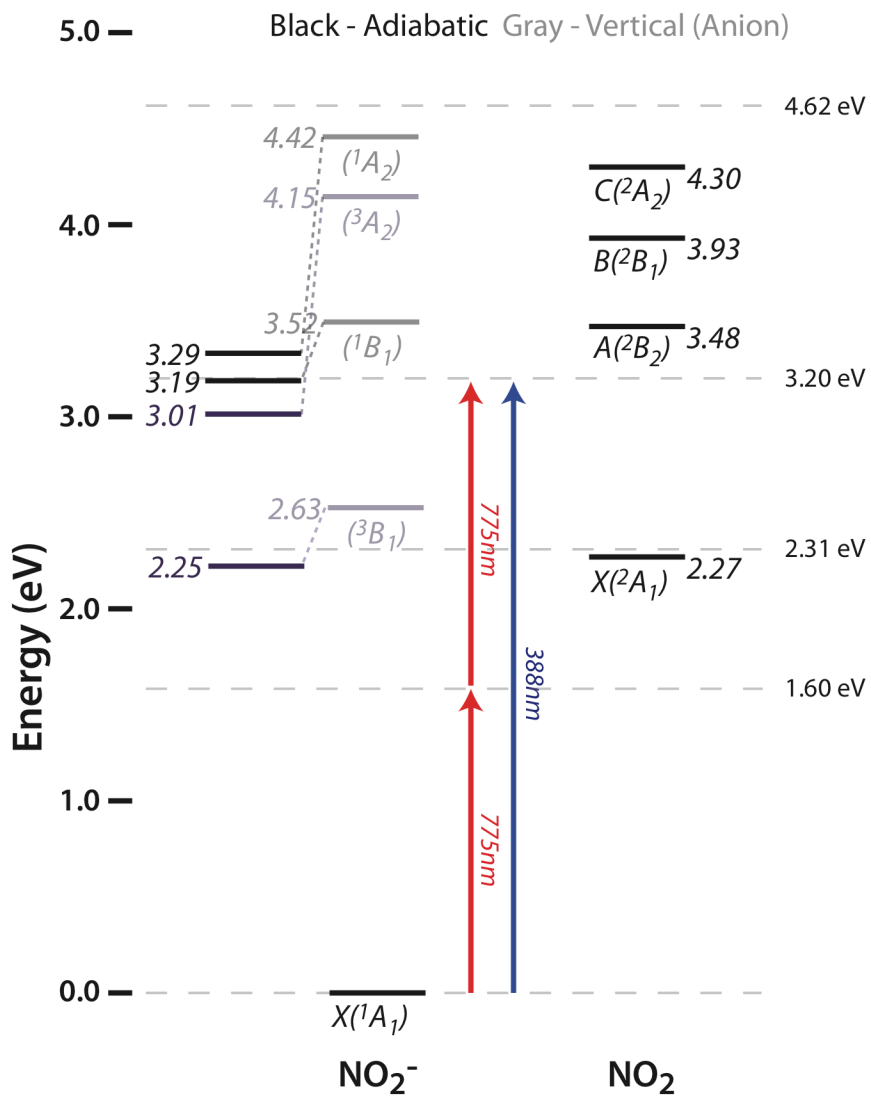


Figure 8.1: An energy level diagram for anionic and neutral NO₂. Photon energies for the two excitation schemes are also presented.

angular distributions.^{10,11} Recently near-threshold two-photon detachment of the HOCO^- anion has been proposed to proceed through a temporarily bound shape resonance¹² or a vibrational Feshbach resonance.¹³ However, little work has been done on multiphoton detachment of molecules with photon energies well below the detachment threshold and away from known resonances. Here we report the two-photon photodetachment of NO_2^- using 1.60 eV photons, and compare to one-photon detachment at 3.20 eV. We find that the photoelectron images, and thus the PADs, show stark differences between the one- and two-photon cases, shown in Figure 8.2, which can be reproduced using a simple interference model for electron detachment.

8.2. Experimental

NO_2^- anions were produced in a supersonic expansion of NO, CH_4 , and Ar through a coaxial pulsed electric discharge and a crossed 1 keV electron beam, accelerated to 7 keV, mass selected by time-of-flight, and trapped in a cryogenic electrostatic ion beam trap for up to 5 seconds.¹⁴ Throughout the trapping time, the ions were bunched and intersected by laser pulses from a 1 kHz Ti:Sapphire regenerative amplifier, with a focus of less than 1 mm. Two experiments were performed, one at the laser fundamental wavelength of 775 nm (1.60 eV) with a power density of $\sim 2 \times 10^{10}$ W/cm² in a 1.8 ps FWHM as measured by autocorrelation, and one at 388 nm (3.20 eV) with $\sim 1 \times 10^{10}$ W/cm² power density by doubling the laser output. Detached electrons were extracted from the beam and detected in a velocity mapping¹⁵ time-and-position sensitive electron detector, and resultant neutral NO_2 molecules recoiling out of the trap were collected on a time-and-position sensitive neutral particle detector coaxial with the ion beam.

8.3. Results and Discussion

The top panel of Figure 8.3 presents a comparison of photoelectron spectra obtained for two-photon detachment at 1.60 eV to one photon at 3.20 eV for $X^2A_1 \leftarrow X^1A_1$ detachment. It is clear that while the electron kinetic energy spectra (eKE) for both are quite similar, the PADs (Figure 8.2) are radically different, with the one-photon process dominated by parallel p-wave detachment and the two-photon process by interfering s- and d-waves with primarily perpendicular character. The overall Franck-Condon profiles of both spectra agree well with those observed previously in one-photon experiments.⁴ The discrepancy in intensities between the two spectra below 0.3 eV can be attributed to the larger cross-section for the s-wave component in two-photon detachment than p-wave one-photon detachment due to the Wigner threshold law.¹⁶ From the two-photon PADs, anisotropy parameters $\beta_2(E)$ and $\beta_4(E)$ can be extracted by fitting the energy-resolved angular distributions to the equation⁹

$$I(\theta, E) \propto 1 + \beta_2(E)P_2(\cos \theta) + \beta_4(E)P_4(\cos \theta) \quad (8.1)$$

and are shown in the second panel of Figure 8.3.

Since no electronic states of the anion are predicted to exist below the detachment threshold, the fact that this process is observed at this laser fluence is somewhat mysterious. The laser flux in these experiments, $\sim 10^{10}$ W/cm², is likely too low to significant strong field effects, with a ponderomotive energy on the order of a few meV. A pure rovibrational transition in the anion ground state would involve a change of at

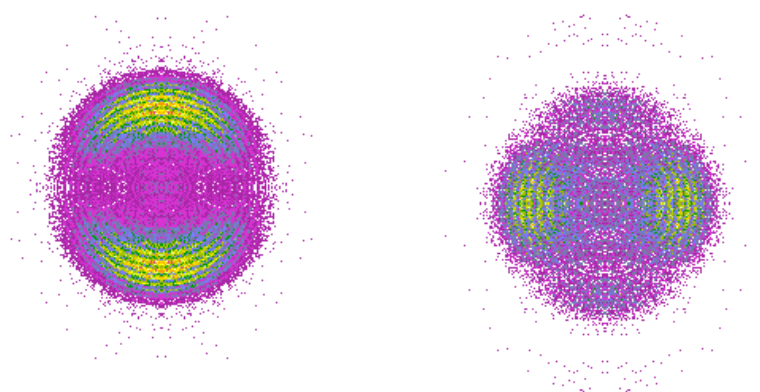


Figure 8.2: Comparison of sliced (see Chapter 2.4.5) photoelectron images for 1-photon (left) and 2-photon (right) detachment.

least 9 quanta of vibration and thus would have a negligible cross-section, so this process is unlikely to give a strongly resonant intermediate state. One possibility is that the second photon leads to resonance with an anion state above the detachment threshold, providing a large enough cross-section to give rise to measurable signal but a short enough lifetime to appear as a prompt photodetachment process. Another potential explanation is a completely coherent two-photon process, in which detachment occurs through a purely virtual state. The PAD likely holds the key to unraveling this process, though *a priori* prediction of photoelectron angular distributions remains a challenge even in the case of one photon detachment.

For a two-photon process, the PADs can be expressed as a superposition of spherical harmonic partial waves as

$$I(\theta) \propto |c_{00}e^{i\delta_0}Y_{00} + c_{20}e^{i\delta_2}Y_{20}|^2 \quad (8.2)$$

and the *s*- and *d*- partial wave contributions and phase shifts can be derived from the anisotropy parameters by

$$\frac{c_{20}(E)}{c_{00}(E)} = \left(\frac{18}{7\beta_4(E)} - 1 \right)^{-\frac{1}{2}} \quad (8.3)$$

$$\cos(\delta_0(E) - \delta_2(E)) = \frac{\frac{c_{20}(E)}{c_{00}(E)} \left(\frac{9\beta_2(E)}{\beta_4(E)} - 5 \right)}{7\sqrt{5}}, \quad (8.4)$$

where *E* is the electron kinetic energy (eKE), and are shown in the bottom two panels of Figure 8.3. The ratio of d-wave to s-wave amplitudes is seen to increase nearly linearly throughout the energy range of the 775 nm spectrum, in agreement with the Wigner threshold law, while the relative phase of the two partial waves is essentially constant.

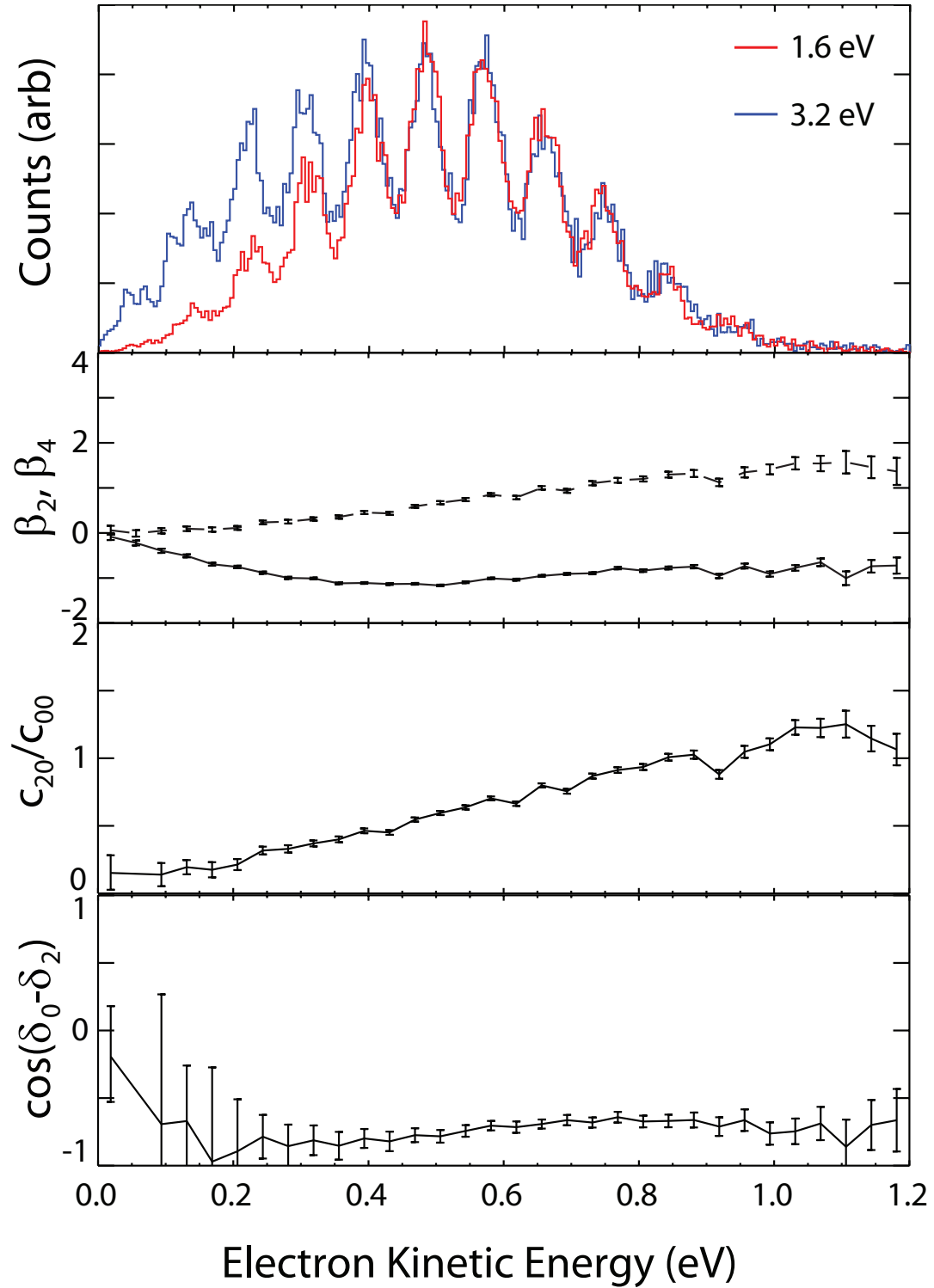


Figure 8.3: (Top) Comparison of photoelectron spectra for 1- and 2-photon detachment. (Middle top) Derived anisotropy parameters. (Middle bottom) Partial wave amplitude ratios. (Bottom) Partial wave relative phase shift.

Due to the similarities in the Franck-Condon profiles at both wavelengths, it is expected that any resonances that might be participating in this process must be short-lived. A resonance lifetime approaching a molecular vibrational period would be expected to yield qualitative changes in the Franck-Condon profile. A two-photon resonance proceeding through a virtual state, or a coherent two-photon process, could be expected to have little impact on the Franck-Condon factors. Energetically, the simplest explanation is coherent two-photon absorption; however, examination of Figure 8.1 does reveal several candidate anion states for two-photon resonances. In the 775 nm case, the 1B_1 state is predicted to have an adiabatic excitation energy of 3.19 – 3.36 eV,^{17,18} almost exactly the two-photon energy. The predicted structure of this state is $r_{NO} = 1.30 \text{ \AA}$, $\theta_{ONO} = 129^\circ$, while the anion geometry has been shown to be $r_{NO} = 1.25 \text{ \AA}$, $\theta_{ONO} = 117^\circ$, so a direct resonance is unlikely. The vertical excitation energy to this state is calculated at 3.52 eV,¹⁷ making it plausible that this state could be supporting the two-photon process somehow, but no measurements exist to verify these predictions. Additional candidate states for this wavelength include 1A_2 , which has an adiabatic excitation energy of 3.24 – 3.29 eV but a significantly higher vertical excitation energy, and the corresponding triplet states, which are lower in energy but formally spin-forbidden.

With no conclusive energetic evidence to lend credence to either explanation, the PADs are analyzed in an attempt to further clarify the picture. Several frameworks exist for extracting intuitive insights from the PADs into the electronic structure underlying photodetachment processes. The Cooper-Zare model,¹⁹ in which photoelectron partial waves are treated as emanating from a single center, has shown the ability to predict quantitative features of atomic anions and qualitative features of molecular anions. The

s&p model,²⁰ a qualitative extension of the symmetry considerations suggested for photodetachment cross-sections by Reed and Brauman,²¹ has helped to rationalize PADs of molecules with relatively high symmetry. This approach uses the symmetries of the initial and final molecular orbitals and the transition dipole operator to predict the symmetry of the PAD. However, quantitative agreement of predicted PADs with experiment generally requires complex *ab initio*-based calculations,^{22,23} and few if any of these techniques are known to have been extended to multiphoton detachment.

Another simple and intuitive model of photodetachment treats each atom as an individual electron scattering center, then sums the contributions of each atom to arrive at an interference pattern governing the PAD, as suggested by Reed and Brauman, and based on a cross-section formalism developed by Cohen and Fano.²⁴ The implementation of this model developed for this problem will now be described. By working in the minimum-basis limit of LCAO-MO theory, molecular photodetachment is approximated as a coherent superposition of atomic photodetachment events, in which angular momentum is a good quantum number and is strictly conserved. In NO_2^- , the highest occupied molecular orbital (HOMO) configuration, shown in Figure 8.4, can be represented as $S^{(N)} - P_z^{(O)} - P_z^{(O')}$, and the differences in the observed PADs at the three wavelengths can be rationalized and visualized. For one-photon detachment by a linearly polarized laser, $\Delta l = \pm 1$ and $\Delta m = 0$, and since detachment of an electron leaves NO_2 with a singly occupied HOMO and no change in orbital angular momentum, this momentum must be carried away by the electron. This leads to a wavefunction for the detached electron characterized by $P_z^{(N)} - aS^{(O)} - aS^{(O')}$ (un-normalized), where a is a scaling factor

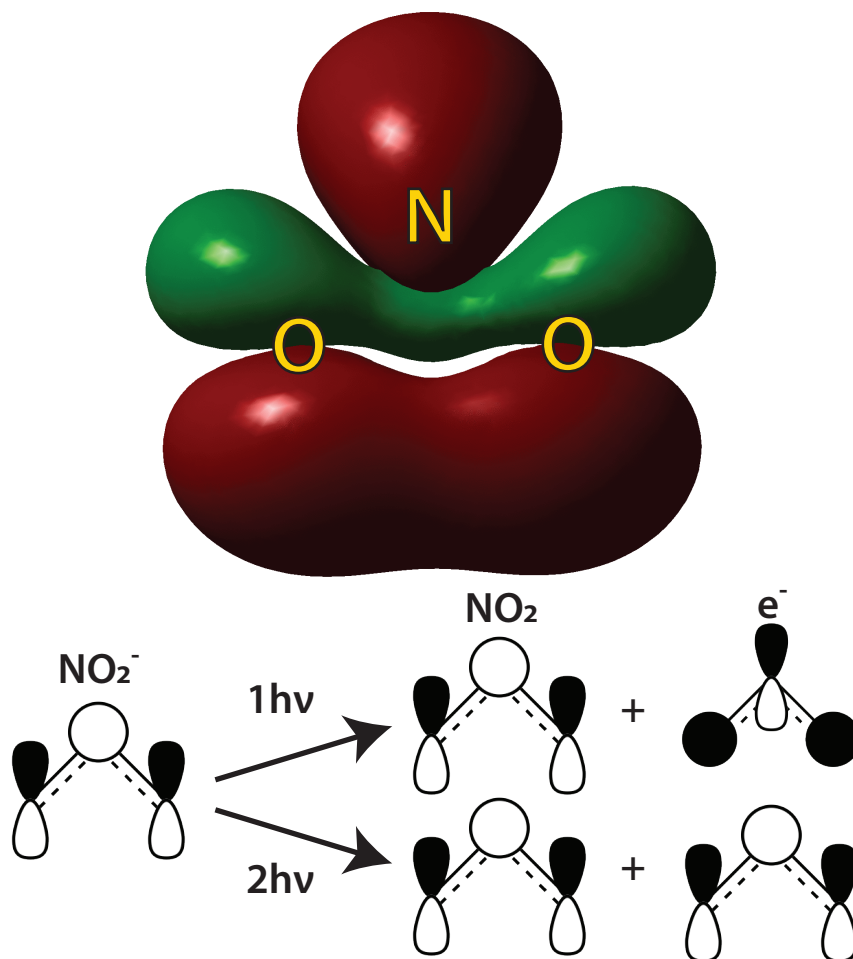


Figure 8.4: Top: NO_2^- HOMO. Bottom: LCAO picture of initial and final MOs and the required angular momenta of outgoing electrons from atomic centers.

relating s and p wave amplitudes, and only the lowest angular momentum components are considered. However, in two-photon detachment, $\Delta l = 0, \pm 2$ and the detached electron wavefunction is characterized by $bS^{(N)} - P_z^{(O)} - P_z^{(O')}$. This scheme is implemented numerically on a simple grid with each wavefunction separated into radial and angular components described by spherical Bessel functions and spherical harmonics, respectively:²⁴

$$\langle r | \psi_e \rangle \propto j_l(kr) Y_{l0}(\theta). \quad (8.5)$$

By optimizing the parameter a or b and integrating over an anisotropic angular distribution given by $\cos^{2n}\theta$ to account for the 2nd order dipole-photon interaction, interference patterns in quantitative agreement with the observed PADs can be produced at a given eKE as shown in Figure 8.5 for n=4. It is found that changes in the angular distributions can be explained primarily on the basis of changes in interference patterns brought on by the electron de Broglie wavelength, and the increases in the s- partial wave amplitudes induced by the Wigner threshold law.

The $\cos^8\theta$ anisotropy is surprising – generally for two-photon detachment one would expect at most a $\cos^4\theta$ dependence in the perturbative limit. It is possible that some strong-field effects, such as dynamical alignment of the transition dipole along the polarization vector, are beginning to become significant at this laser intensity. This would be expected to add another power of two to the $\cos\theta$ dependence.²⁵ However, the weak permanent dipole and unremarkable polarizability of NO₂, either of which would need to be large at these laser fluences, do not support this possibility.

Weaknesses in the model could account for the missing anisotropy. The neglect of a d-orbital on the nominally s-orbital could account for some loss of anisotropy – at

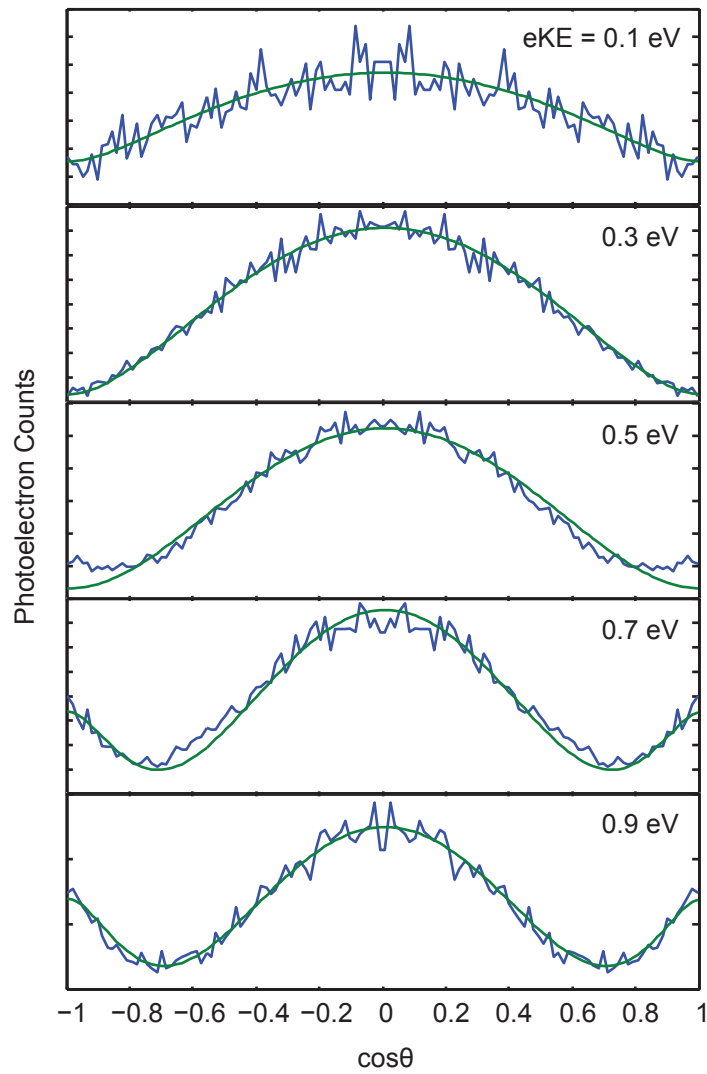


Figure 8.5: PADs and model fits for five different electron energies. Here $n=4$, and the only fitting parameter is b , the ratio of s- to p-partial waves.

low electron energies this is expected to be damped by the Wigner law, but at higher energies, >0.4 eV according to the comparison of photoelectron spectra in Figure 8.3, this could potentially lead to some error. Incorporation of d-waves into the model is straightforward, however the additional fitting parameter describing the d-wave amplitude complicates the procedure. Since the Wigner law is rigorous for atomic detachment at low eKE , the s-/d-wave amplitude ratios can in principle be fixed. Work on including this effect in the model is ongoing.

A potentially more limiting weakness in the model is the exclusion of effects caused by rotation of the polarization vector out of the plane of the molecule (in the ϕ direction of a spherical coordinate system where $\theta=0$ corresponds to the symmetry axis). Addition of a third dimension to the interference calculations is relatively straightforward but computationally demanding. However, the integral over ϕ could provide the extra dependence on $\cos\theta$ needed. Additionally, since the dimensions of the molecule are still smaller than one electron de Broglie wavelength at the energies considered here, leading to interference patterns which are approximately cylindrically symmetric about the major axis of NO_2 . If this is the case, explicit integration over ϕ would be unnecessary, and its effect can be included phenomenologically in the model as extra dependence on $\cos\theta$. This has not yet been rigorously shown but will be addressed.

8.4. Conclusions

Ultimately, these datasets alone are not sufficient to unambiguously determine the two-photon mechanisms involved in these two processes. Work is continuing on further unraveling these issues experimentally, and understanding the dynamics of photodetachment to NO_2 excited states, but a full understanding of this process may only

come about with the help of theoretical efforts to predict the quantitative effects of the possible mechanisms for detachment on the PADs as well as the possible effects of resonances in the vicinity of the second photon energy. While the model presented here has little predictive power, insights gained from it are used to work backwards towards to test hypotheses regarding the nature of this process. The strong anisotropy required to fit the experimental PADs suggests some type of alignment, potentially due to a resonance, in the photodetachment process. This is not enough to rule out coherent two-photon absorption, but it does offer guidance for further studies of this system.

References

- (1) Hsu, D. K.; Monts, D. L.; Zare, R. N. *Spectral Atlas of Nitrogen Dioxide 5530 Å to 5480 Å*; Academic Press: New York, NY, 1978.
- (2) Uehara, K.; Sasada, H. *High Resolution Spectral Atlas of Nitrogen Dioxide 559-597 nm*; Springer: Berlin, 1985.
- (3) Woo, S. B.; Helmy, E. M.; Mauk, P. H.; Paszek, A. P. *Phys. Rev. A* **1981**, *24*, 1380.
- (4) Ervin, K. M.; HO, J.; Lineberger, W. C. *J. Phys. Chem.* **1988**, *92*, 5405.
- (5) Weaver, A.; Metz, R. B.; Bradforth, S. E.; Neumark, D. M. *J. Chem. Phys.* **1989**, *90*, 2070.
- (6) Stolow, A.; Bragg, A. E.; Neumark, D. M. *Chem. Rev.* **2004**, *104*, 1719.
- (7) Ledingham, K. W. D.; Singhal, R. P. *Int. J. Mass Spectrom. Ion Proc.* **1997**, *163*, 149.
- (8) Blondel, C.; Delsart, C. *Laser Physics* **1993**, *3*, 699.
- (9) Reid, K. L. *Annu. Rev. Phys. Chem.* **2003**, *54*, 397.
- (10) Reichle, R.; Helm, H.; Kiyan, I. Y. *Phys. Rev. Lett.* **2001**, *87*, 243001.
- (11) Reichle, R.; Helm, H.; Kiyan, I. Y. *Phys. Rev. A* **2003**, *68*, 63404.
- (12) Lu, Z.; Continetti, R. E. *Phys. Rev. Lett.* **2007**, *99*, 113005.
- (13) Miyabe, S.; Haxton, D. J.; Lawler, K. V.; Orel, A. E. *Phys. Rev. A* **2011**, *83*, 043401.
- (14) Johnson, C. J.; Continetti, R. E. *J. Phys. Chem. Lett.* **2010**, *1*, 1895.
- (15) Eppink, A.; Parker, D. H. *Rev. Sci. Instrum.* **1997**, *68*, 3477.
- (16) Farley, J. W. *Phys. Rev. A* **1989**, *40*, 6286.
- (17) Czernek, J.; Živný, O. *Chem. Phys. Lett.* **2007**, *435*, 29.
- (18) Cai, Z. L. *J. Chem. Soc. Faraday T.* **1993**, *89*, 991.
- (19) Cooper, J.; Zare, R. N. *J. Chem. Phys.* **1968**, *48*, 942.

- (20) Sanov, A.; Mabbs, R. *Int. Rev. Phys. Chem.* **2008**, *27*, 53.
- (21) Reed, K. J.; Zimmerman, A. H.; Andersen, H. C.; Brauman, J. I. *J. Chem. Phys.* **1976**, *64*, 1368.
- (22) Lucchese, R. R. *J. Electron Spectrosc. Rel. Phenom.* **2004**, *141*, 201
- (23) Oana, C. M.; Krylov, A. I. *J. Chem. Phys.* **2009**, *131*, 124114.
- (24) Cohen, H.; Fano, U. *Phys. Rev.* **1966**, *150*, 30.
- (25) Stapelfeldt, H.; Seideman, T. *Rev. Mod. Phys.* **2003**, *75*, 543.

Appendix A. Design of a New Multiparticle Time- and Position-Sensitive Detector

A.1. Operating Principles

Time and position sensitive detectors are instrumental in a variety of experiments, including fast (keV-MeV lab energy) beam dissociation studies of nuclear, atomic, and molecular processes,¹⁻³ photon detection in UV/X-ray astronomy and synchrotron radiation experiments,⁴ tomographic atom probe microscopy of surfaces,⁵ certain electron microscopy techniques, and a variety of other applications. Some of these experiments require the detection of only a single particle at a time; thus most types of detectors excel at recording hits of a single particle, or perhaps a few particles coincidentally. In the last two decades, increasingly sophisticated studies of dynamics of larger systems and the desire to gather more data at higher rates have called for detectors capable of detecting the times and positions of arrival of many particles in coincidence, with higher resolution and higher efficiency.

These types of detectors are characterized by four important properties: 1) the overall resolution of the detector, 2) the multiplicity, or number of particles that can be detected in coincidence, 3) the dead time and dead area, which describe events which can not be detected due to detector geometry or acquisition characteristics, and 4) the expense and complexity of use of the detector, including difficulty of calibration. The main types

of time and position sensitive multiparticle detectors currently used in molecular dissociation experiments are delay line anodes,^{6,7} charged coupled device (CCD) cameras with segmented photomultiplier tubes (PMTs),⁸ dual CCDs with a fast optical gate,³ and a delay line and CCD combination approach.² Currently deployed methods are typically adequate in only 2-3 of these areas. Most schemes are practically limited to up to two, three, or four particles, and have limited product kinetic energy resolution.

A new approach borrowing from and expanding upon current schemes is being developed which is intended to match or exceed the capabilities of current detectors in all four of the above characteristics, providing a powerful and more accessible tool for researchers in a broad range of disciplines. The goal of the new detector is not just to address one shortfall of current methods, but rather to achieve gains in all areas. Thus, it should allow for increased resolution of both times and positions of arrival of particles, detect a larger number of particles than current methods, have practically no dead time or area in order to record events of any dissociation geometry, and be relatively inexpensive and easy to construct and use.

In order to increase multiplicity to a large number of particles and to reduce dead times and areas, it is clear that the most feasible approach is to implement a system in which the number of detector elements does not scale with the number of particles to be detected. The only elements required are timing information and position information and some way to correlate the two. Rather than attempting to increase the amount of information detected to enable this correlation, it will be easier to encode some type of position information into a set of time information which can be extracted during

analysis.

The detector consists primarily of a standard fragment imaging setup as shown in Figure A.1,⁹ with particles impinging on a set of microchannel plate (MCP) electron multipliers. The showers of electrons generated by the MCPs are accelerated onto a phosphor screen, whose emission is imaged by a CCD detector to determine positions. If the phosphor exponential decay time is similar to or less than the average temporal spacing of particles, it will be easy to distinguish times of individual hits on the screen using a photomultiplier tube (PMT) connected to a fast digitizer to record the entire signal. With this setup, all that is required is a way to connect position information to timing - this will be accomplished by segmenting the phosphor screen into four areas, each with different ratios of two colors of phosphor. By analyzing the ratios of signals on two PMTs, each filtered to accept light from only one type of phosphor, assignment of the quadrant of impact can be made. Additionally, since both the CCD and PMT are linear detectors, the integrated areas of peaks recorded on the CCD will be linearly proportional to the integrated areas of the corresponding peaks in the PMT signal, and thus peaks of different intensities can be distinguished. By using these two properties, times and positions will be able to be matched and crosschecked for a large number of particles in a single event, even if multiple particles hit the same phosphor segment.

A.2. System Design

In addition to increased multiplicity, another goal of this detector is to provide better resolution than current systems. Since there are no complex anodes, there is little cost disadvantage to making the detector large. To this extent, standard MCPs of 75 mm

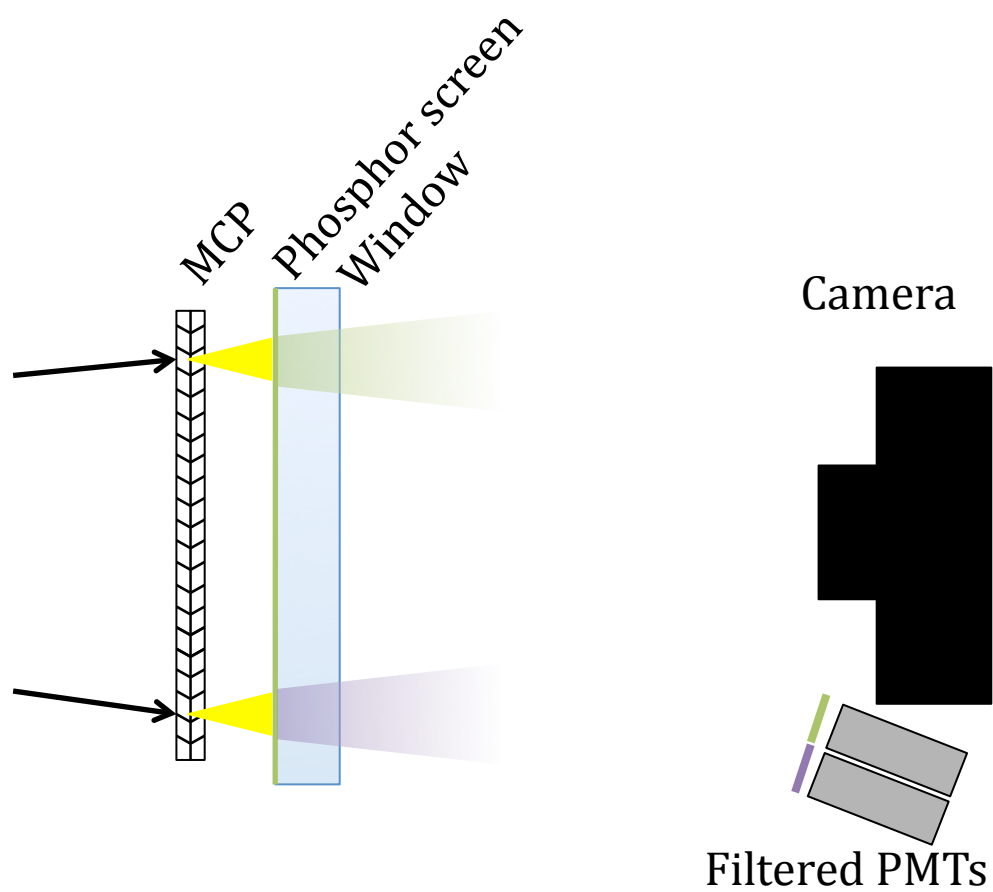


Figure A.1: A diagram of the detector setup.

in diameter with 25 micron pore spacing can be used, rather than the previous 40 mm sets, and less expensive double-stacks are used rather than high-gain triple-stacks. With the use of centroiding techniques for CCD images,¹⁰ resolutions much less than a CCD pixel are achievable. Thus, the main component of the detector position uncertainty will be the MCP pore separation, giving a position resolution slightly larger than the pore spacing. Combined with the increased recoil distance available with a larger detector, position resolution well exceeding current methods is expected. Timing resolution is determined mainly by the sophistication of the software algorithm used to analyze PMT output - simulations suggest that this resolution will be ~80 ps, an order of magnitude better than the position resolution and thus will not be a large factor in the overall resolution of the detector.

Acquisition and real time analysis of the data produced by this system is computationally intensive and, if not reduced, would result in an unfeasible amount of data to be written to disk. The incoming data must be quickly discriminated and reduced in real time. The first level of discrimination occurs with a fast veto of the CCD frame in the event of no PMT signal. For typical experiments, this should lead to an 80% reduction in data throughput. Further gains can be made by thresholding the image and keeping only the pixels with statistically relevant data in them. This method will lead to image data sizes being significantly smaller than timing data. Unfortunately, the timing data will be more difficult to reduce, and thus in the first run will be kept in full. This scheme will result in a typical event size of 4.5 kB. So with a raw data acquisition rate of 200 Hz, an hour of data would amount to 3.2 GB, a significant but not unmanageable

size. It is important to note that by retaining the signal digitally rather than losing it through analog processing, newer and more accurate algorithms can be applied to older data sets to increase the information drawn from the data or to cater analysis to specific sets of data.

A.3. Mechanical Design

The detector is mounted on a 13.25" conflat flange for mating to the existing instrument. The phosphor screen is viewed through a borosilicate glass plate in the test configuration, and fiber optic faceplate in the final version. In order to maintain high vacuum in the detector chamber while allowing for easy dismounting of the phosphor screen assembly, the window is designed with a differentially pumped, double o-ring sliding seal and the middle chamber pumped to below 1 torr with a mechanical pump, reducing the permeation gas load through the high vacuum o-ring. The phosphor screen is electrically connected to an annular anode, allowing the screen to be biased up to 20 kV while maintaining a flat electric field for the electrons from the MCP to be accelerated through. Insulation of this anode from the flange is accomplished using a PEEK annular mount.

The MCP body is relatively simple, as the back plate of the MCPs is held at ground and thus can be suspended by a superstructure directly connected to the flange. The front plate will be biased at 2000-2400 V, and is held in place by a spring-loaded circular pad connected to the front electrode of the detector. This electrode is held at the front plate bias, and electrically isolated from the detector body by PEEK standoffs.

Outside of vacuum, the camera is mounted to a light-baffled tube, directly imaging the phosphor screen. Two PMTs will be placed on either side of the camera, with optical filters to select the phosphor type they are sensitive to. The outputs of the two PMTs are fed into the two channels of a 1 GS/s, 8 bit high speed ADC, while the camera is directly read out by a full CameraLink framegrabber. In order to reach the desired 1 kHz frame rate, the resolution of the camera will be set to 454 x 454 pixels. Triggering of acquisition is performed electronically via direct TTL inputs to the framegrabber and ADC cards.

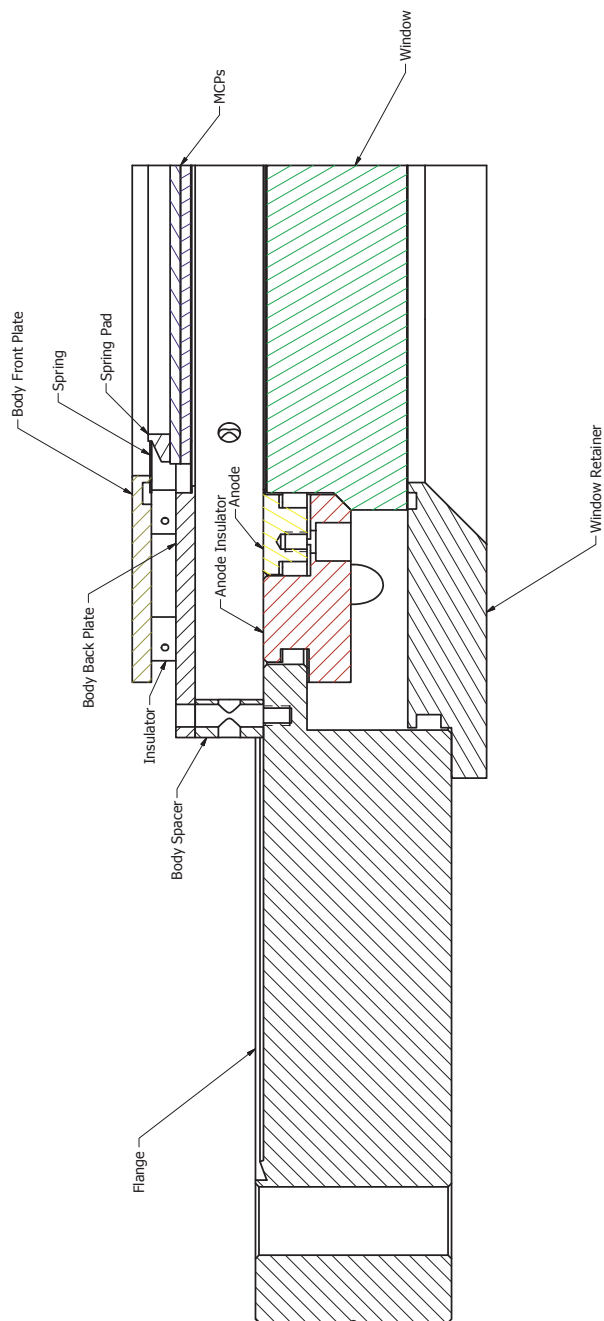


Figure A.2: A schematic of the mechanical assembly of the detector.

References

- (1) Hanold, K.; Luong, A.; Clements, T.; Continetti, R. *Rev. Sci. Instrum.* **1999**, *70*, 2268.
- (2) Ismail, I.; Barat, M.; Brenot, J.; Fayeton, J.; Lepere, V.; Picard, Y. *Rev. Sci. Instrum.* **2005**, *76*, 043304.
- (3) Strasser, D.; Urbain, X.; Pedersen, H.; Altstein, N.; Heber, O.; Wester, R.; Bhushan, K.; Zajfman, D. *Rev. Sci. Instrum.* **2000**, *71*, 3092.
- (4) Siegmund, O.; Lampton, M.; Raffanti, R.; Herrick, W. In *Nuclear Instruments & Methods in Physics Research Section A-Accelerators Spectrometers Detectors and Associated Equipment*; 1991; Vol. 310, pp. 311.
- (5) Cerezo, A.; Godfrey, T.; Hyde, J.; Sijbrandij, S.; Smith, G. *Appl. Surf. Sci.* **1994**, *76*, 374.
- (6) Lampton, M.; Siegmund, O.; Raffanti, R. *Rev. Sci. Instrum.* **1987**, *58*, 2298.
- (7) Da Costa, G.; Vurpillot, F.; Bostel, A.; Bouet, M.; Deconihout, B. *Rev. Sci. Instrum.* **2005**, *76*, 013304.
- (8) Amitay, Z.; Zajfman, D. *Rev. Sci. Instrum.* **1997**, *68*, 1387.
- (9) Heck, A.; Chandler, D. *Annu. Rev. Phys. Chem.* **1995**, *46*, 335.
- (10) Li, W.; Chambreau, S.; Lahankar, S.; Suits, A. *Rev. Sci. Instrum.* **2005**, *76*, 063106.

Appendix B. Electrical Circuits Developed in the Construction of the Instrument

B.1. Instrument Interlock Logic

The most important circuit in the instrument is the interlock system, which protects vital elements from vacuum failures and power distribution issues. The logic for the circuit is shown in Figure B.1.1, and will be briefly outlined. The instrument is roughly divided into two regions, the HV chambers and UHV chambers, since each has a separate backing pump. The interlock system is primarily controls foreline valves, gate valves, the cryo-head, and AC power, and has sensors for foreline pressures and chamber pressures, as well as turbo pump and cryopump operation. The two main goals are to protect the high vacuum pumps from accidental overpressure in the foreline, and to protect detectors from arcing due to high pressures while biased. AC power distribution also has a reset switch to prevent rapid cycling of power supplies if the interlock is momentarily activates then quickly returns to normal.

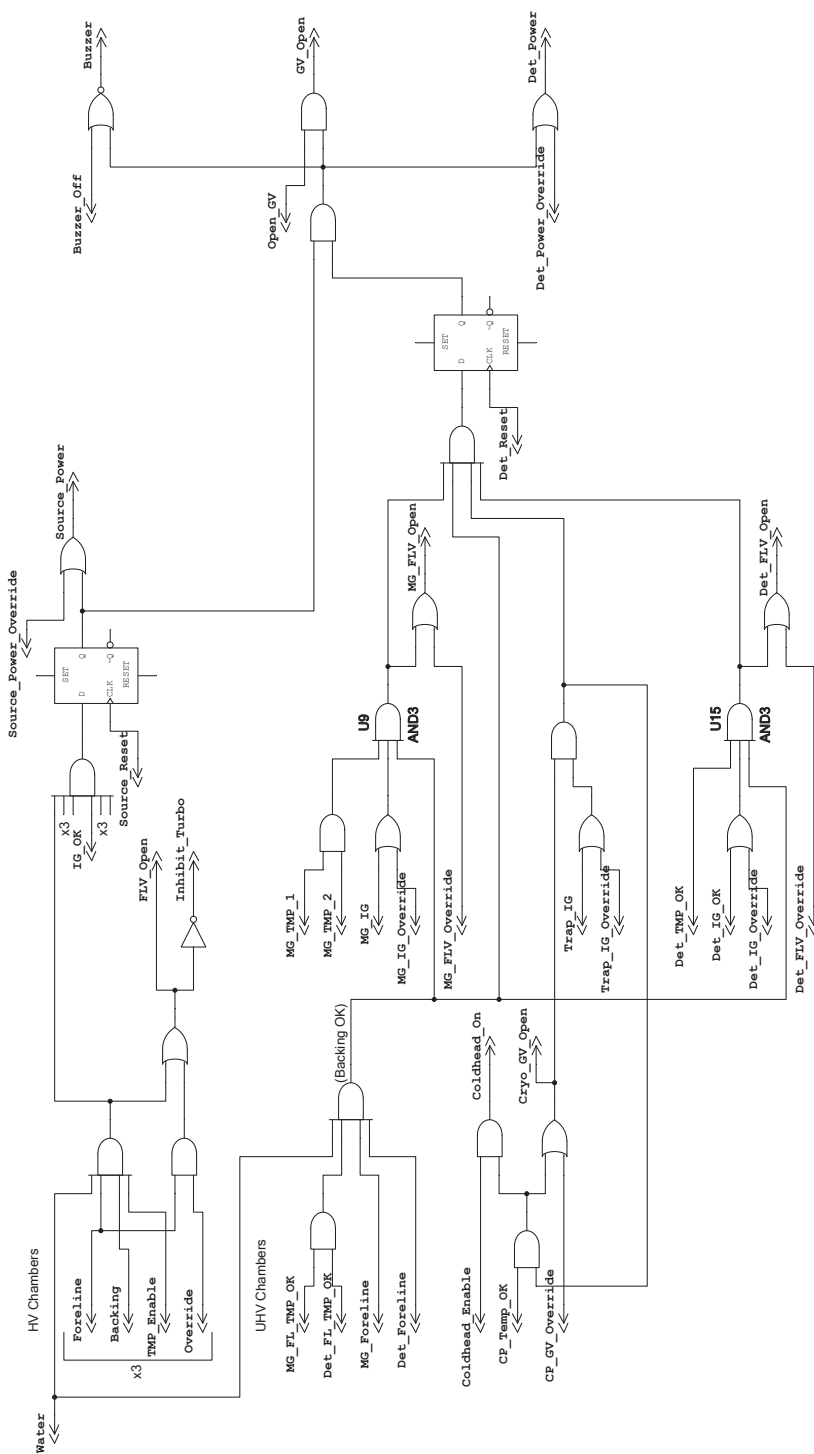


Figure B.1: Interlock system logic

B.2. Mirror Switching Circuit

For injection into the trap, the entrance mirror must be held at ground, then rapidly switched to full voltage and stabilized prior to the first return of the ions (typically 5-10 μ s). It is too costly to switch each mirror individually, so the entire voltage divider must be switched. However, this presents a problem since each plate in the mirror has a capacitance to ground, so large RC time constants must be overcome to reach operational voltages in sufficient time. Fortunately, in addition to capacitive coupling to ground, the mirror electrodes are capacitively coupled to one another, providing a high-frequency bypass and significantly shortening the rise times over the bare RC time constants. By judicious tuning of this capacitive coupling, the rise times can be optimized to produce stable voltages quickly with little over- or under-shoot.

The effective circuit is diagrammed in Figure B.2.1. Buffer capacitors and load resistors are added to the supply side of the switches to provide strong instantaneous currents and isolate switching interference from the static mirrors and the power supply regulation circuitry. The switches are Behlke HTS-GSM series push-pull galvanically isolated MOSFET stacks, capable of switching many kV in 10-20 ns.

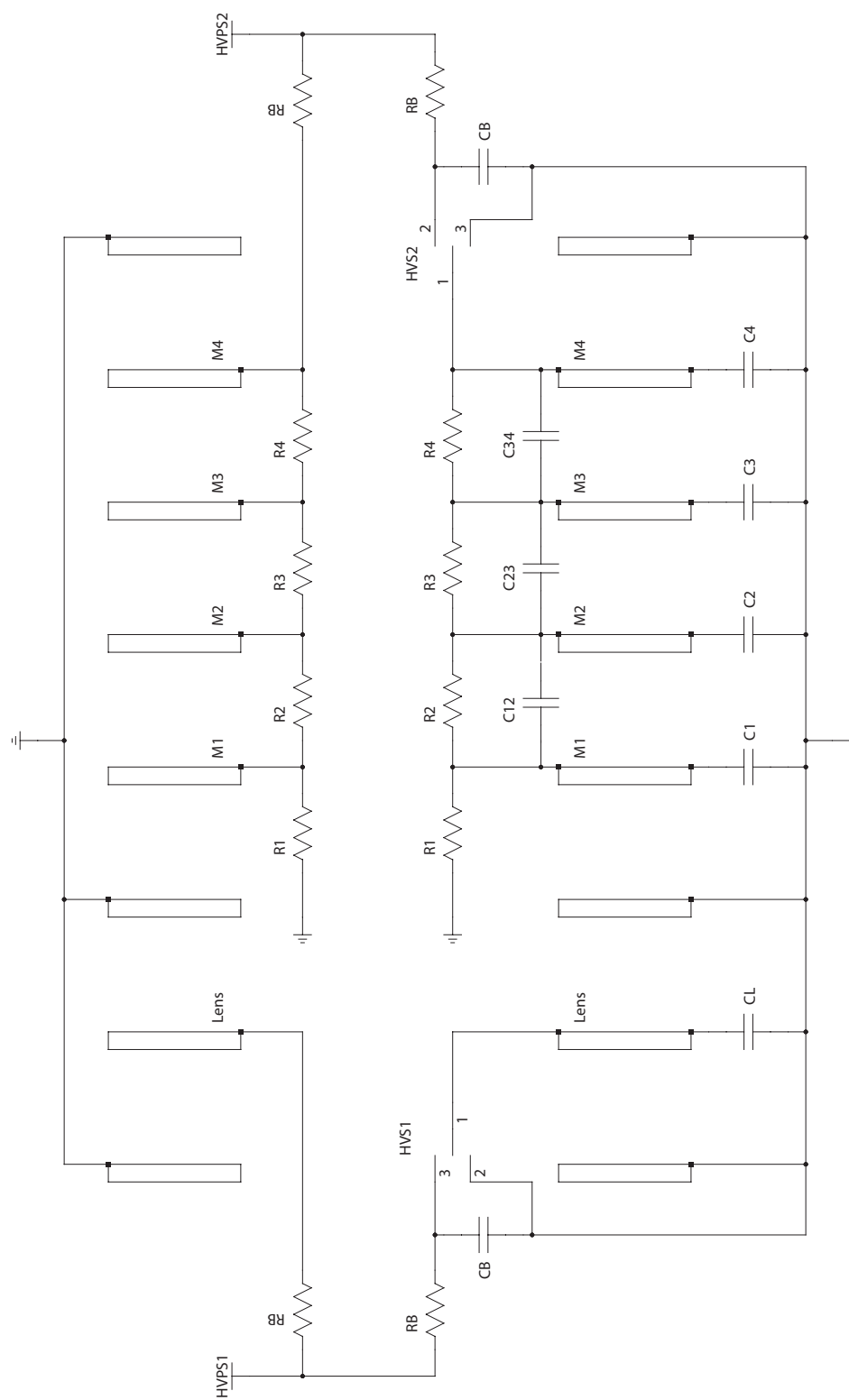


Figure B.2: Mirror switching circuit.

B.3. RF Synchronization System

The laser-ion synchronization system, which was described in Chapter 3, is primarily driven by a field-programmable gate array (FPGA) (Altera Cyclone II) that provides a set of phase-locked loops (PLLs) for frequency conversion and general logic for diagnostic and display systems. The advantage of the FPGA is complete integration of all components necessary for the operation of the system, and ease of programming and reprogramming the system. A block diagram of the FPGA code is shown in Figure B.3.1. Essentially the system has two front-ends: one tuned to operate with the Ti:Sapphire laser, and another to operate with a modelocked Nd:YAG laser. Each front end is composed of a NIM-based level discriminator and logic converter to generate a TTL pulse train that drives the input of a separate phase locked loop, in which frequency multiplication and division are performed ($5/7$ for Ti:S, $5/8$ for Nd:YAG). Each PLL outputs the synthesized clock and a lock detection signal indicating stable PLL operation. The clock signals from each PLL are selected in a multiplexer, and the chosen signal is output to the function generator. For display purposes, two 4-digit counters are implemented to monitor the input and output frequencies to confirm proper operation. This system has proven to be extremely robust, with no failures in nearly a year of operation.

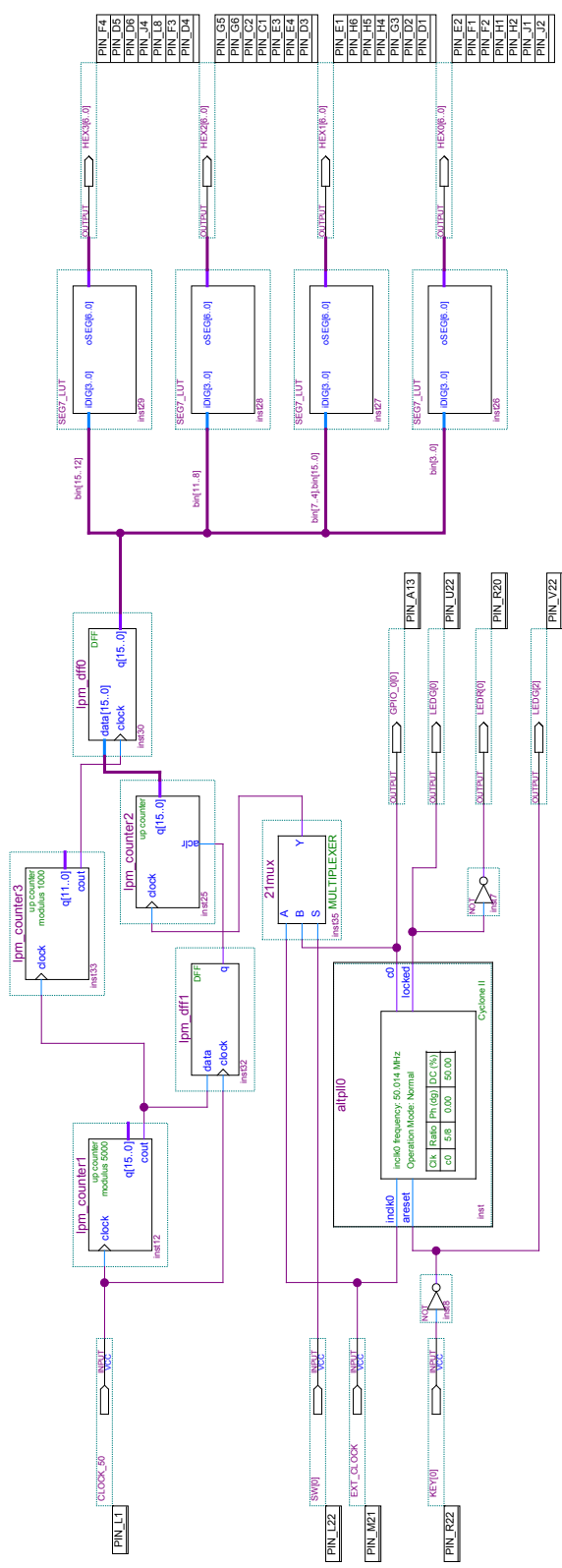


Figure B.3: Synchronization system FPGA design.

B.4. Image Charge Pickup Amplifier

In order to monitor the oscillation of ions in the trap, an image charge pickup is placed on the centerline. This allows for near-real-time diagnostics of trap operation without resorting to destructive methods such as dumping the trap or inducing collisions with high background gas pressures. The typical charge in an ion packet is on the order of 10^4 - 10^6 , requiring a high level of sensitivity and amplification. This sensitivity is also a downside, as the pickup is extremely adept at collecting signals from stray RF sources, acoustic vibrations, and voltage pulses. In order to reduce the influence of external electromagnetic interference, the electrode is connected to the vacuum feedthru by a coaxial cable and is itself shielded in a grounded housing. However, with closed-cycle cryogenerators attached to the system, the acoustic noise, caused by local fluctuations in the capacitance of the center wire as it vibrates within the shield, has been found to be extreme, often leading to signal to noise ratios of 0.1. With appropriate averaging and filtering, this can be somewhat reduced, and ion signal can usually be picked out of an appropriately long fast Fourier transform measurement.

A custom circuit and printed circuit board (PCB) have been designed and built to minimize stray RF noise and maximally filter the acoustic noise in the system. The main charge-sensitive amplifier is an Amptek A250 system with a JFET front end for charge-to-voltage conversion. This amplifier, with a gain of 160 nV/e, outputs a signal which is further filtered and amplified in a 5-pole active high-pass filter with a cutoff frequency of 40 kHz, and finally a 20 MHz low-pass filter on the front end of a digital oscilloscope. The overall circuit diagram for this system is given in Figure B.4.1. The custom-

designed PCB is intended to provide extremely clean supply voltages to the amplifier and reduce the RF cross-section for stray noise. This is accomplished through the use of an array of filter capacitors in parallel on the input voltages, and large ground planes on the top and bottom of the PCB with clearance around the input to reduce its capacitance, as shown in Figure B.4.2. The feedback resistor is chosen to be as large as possible to maximally isolate the electrode from the amplification back-end, and the feedback capacitor as low as possible to increase the overall gain of the system.

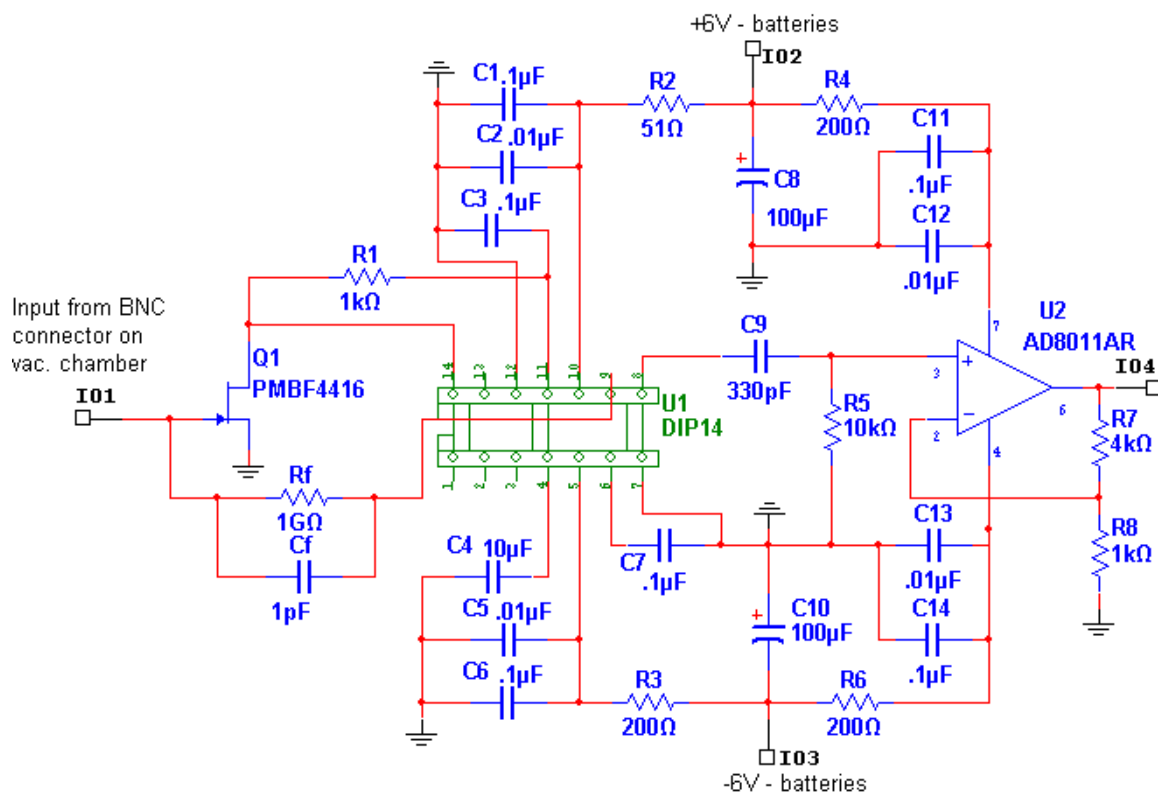


Figure B.4: Charge-sensitive amplifier schematic.

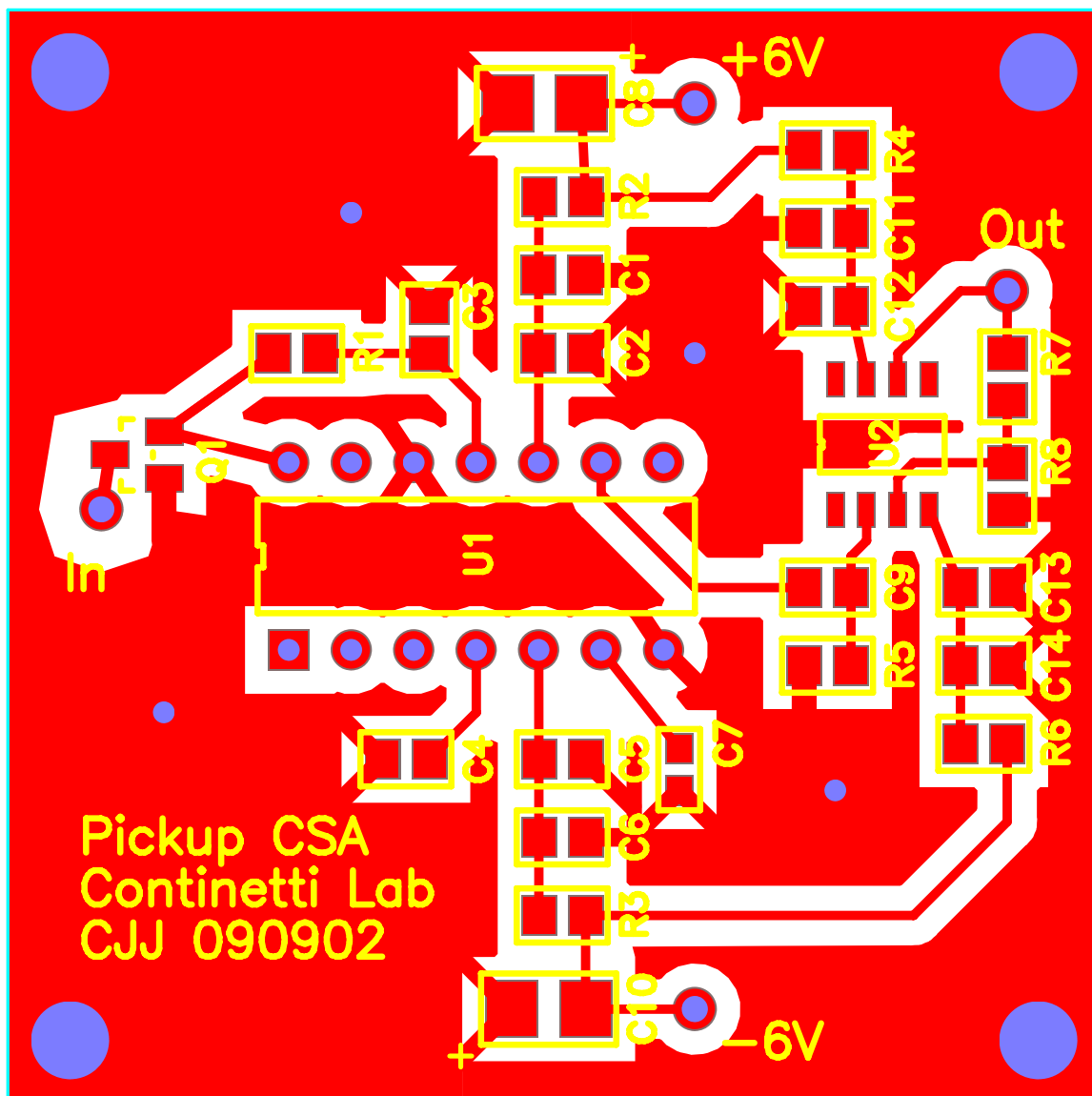


Figure B.5: Top layer of custom charge amplifier PCB.

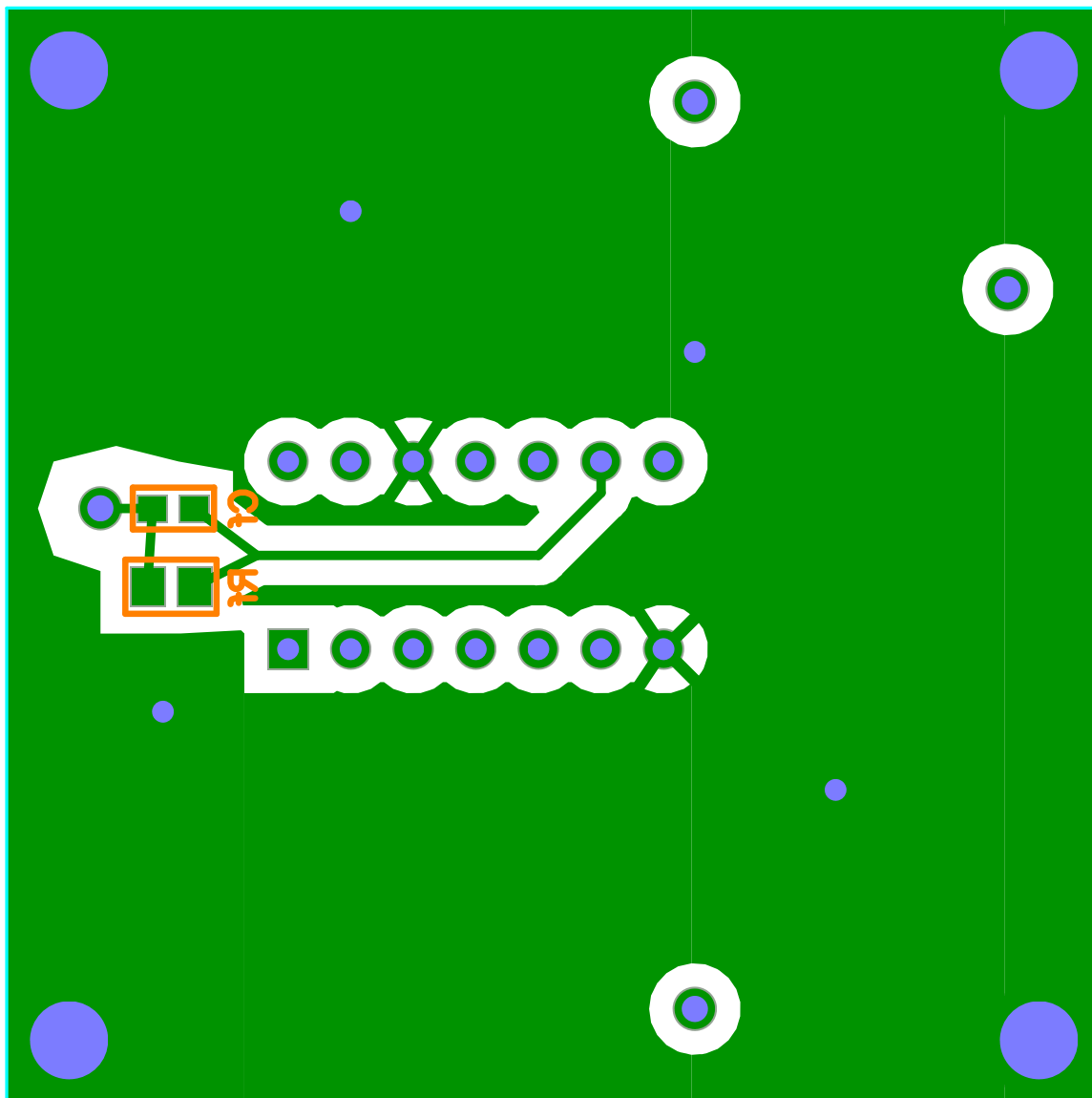


Figure B.6: Bottom layer of charge amplifier PCB.

B.5. Bunching Amplitude Modulation Circuit

Current experiments fix the RF bunching amplitude throughout the entire trapping cycle. While simple, this necessitates careful control of the ion packet-bunching phase to reduce the jarring effect of injection at a non-ideal phase. A circuit has been designed to automatically raise the amplitude of the bunching field to a specified value over a given RC time, allowing the oscillating ions to gradually adapt to the bunching field. It is expected that this will lead to lower loss of ions initially and a smaller spread in ion kinetic energies over the course of trapping. This circuit has been constructed and tested, but is not currently integrated into the experiment.

The circuit is designed to produce pulses with a given RC risetime, a fast fall time, and variable baseline and maximum. It is controlled by two knobs, one for risetime, one for baseline, and one for maximum amplitude, and the input source is the trap switching signal. The front end consists of a potentiometer(R2)-capacitor(C1) combination to produce the RC time constant, and a transistor to bypass the capacitor and generate short fall times. The amplitude is then adjusted in a non-inverting amplifier using potentiometer R8. The baseline is set by a potentiometer(R6) in a voltage divider, which is then compared to a diode-based rectifier (averaging the amplitude of the pulses output from the non-inverting amplifier) to determine the difference in total amplitude and pulse amplitude, and this difference is added to the pulse signal to produce an appropriately scaled signal. Diodes on the output protect from overvoltage.

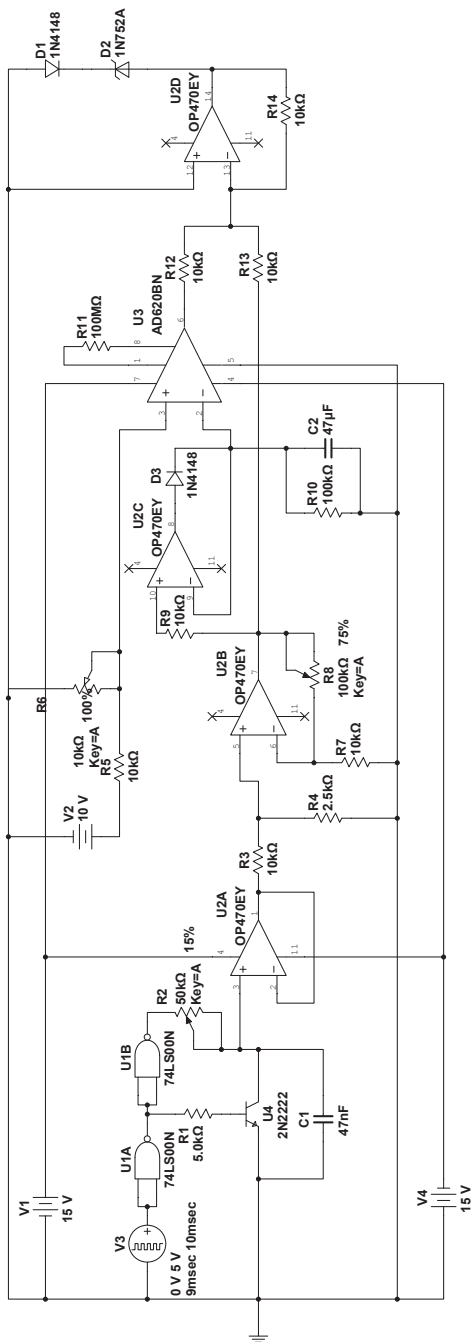


Figure B.7: RF amplitude modulation circuit.

B.6. Electron Detector Bias and Readout Circuit

In order to achieve the narrow pulse-height distributions and consistent spatial profiles of the charge emitted by the MCP electron multipliers in the electron detector, an appropriate biasing and readout circuit must be constructed. In general, the maximum voltage across a single 80:1 MCP is 1400 V. The observed onset of saturation of the triple-stack used in these experiments is 3800 V total, or 1266 V per MCP. Since MCP resistances tend to be on the order of 10-100 Mohm, the bias voltages must be set in a voltage divider with significantly lower total resistance. In the current design, an additional complication arises from the fact that the front plate of the MCP stack must be held at the same voltage as the field-free region of the VMI setup, meaning that this must be stable and adjustable. The solution is to float the front plate using a separate power supply to generate the front plate bias, and drive the MCP bias current through this point. The circuit designed to accomplish this is shown in Figure B.6.1. Each bias contact point is capacitively decoupled to reduce interference, and the front plate voltage is limited by Zener diodes to 200 V for protection. A relatively small load resistor connects the front plate to ground, ensuring no current flows backwards into the MCPs from the front plate supply, or vice-versa. An accelerating field is required to project electrons emitted from the back plate to the anode; this bias is also fixed in the voltage divider.

With the MCP biases set, the rest of the electron detector circuit must provide a means to extract charges and timing from the wedge-and-strip anode. Charges are determined by capacitively coupling high-impedance shaping amplifiers to the biasing voltage lines for each segment of the anode. These segments are each separated from the

bias supply by 10 Mohm resistors, ensuring that charge is extracted slowly enough to be detected by the amplifiers. Timing information is capacitively extracted from the wedge signal by a significantly smaller capacitor, and amplified in a low-impedance high-speed amplifier for the sharp risetimes needed to accurately determine the time-of-arrival of the electron.

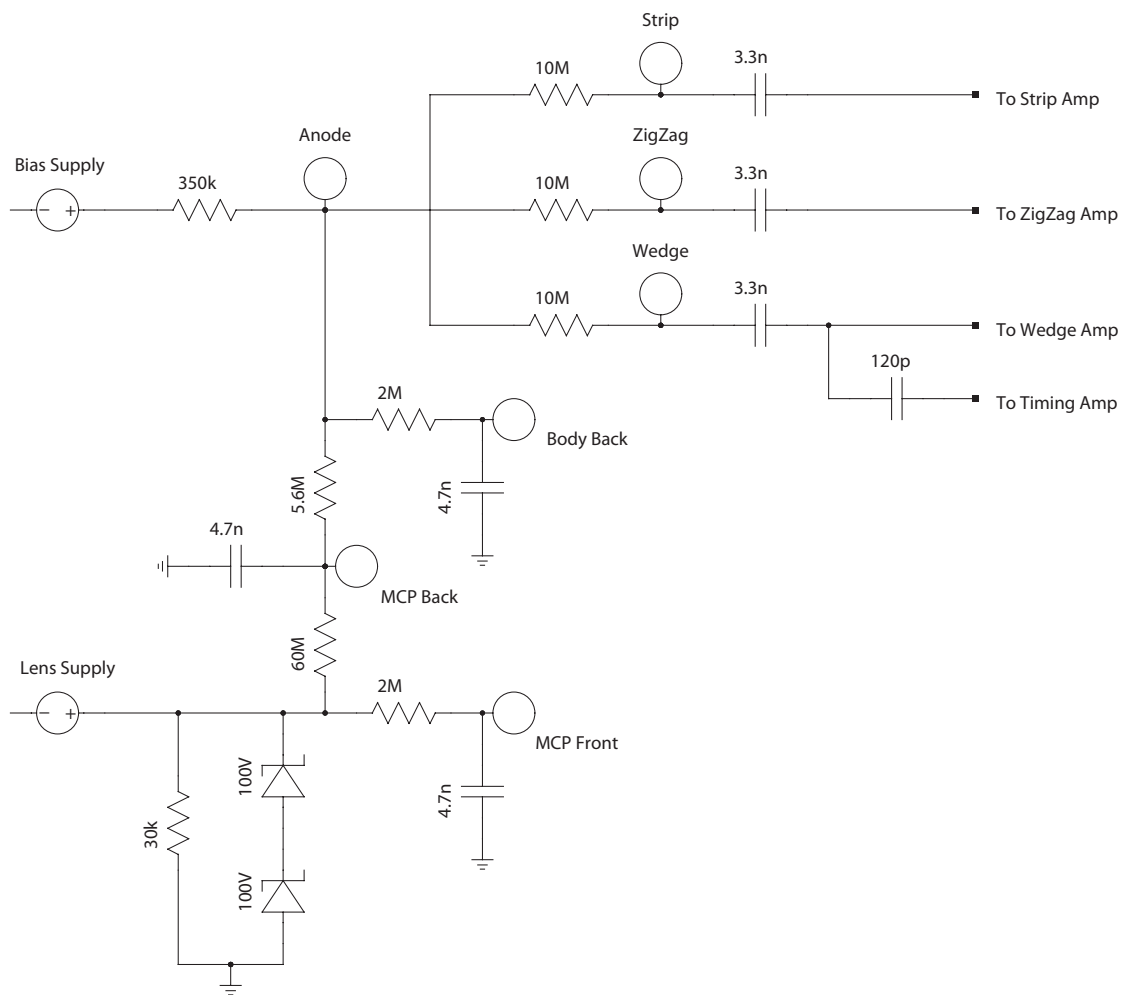


Figure B.8: Electron detector bias circuit.

B.7. Trap Cycle Divider

Since the ion source, at 10 Hz, provides the triggering for trap closing, to achieve trapping times longer than 100 ms it is necessary to trap for multiple source cycles. In order to do this, the trap must be closed on the rising edge of the first source pulse, and opened on the falling edge of the last. Additionally, the number of source cycles for which to trap must be defined. A circuit has been designed by Allen White and constructed at the Physics Electronics shop to perform these duties. Essentially a counter with triggering on rising and falling edges, this unit provides a high-current TTL driver to activate the high voltage switches, and additional TTL outputs for clearing the laser shot counter and other synchronization duties.

